

Alma mater studiorum – Università di Bologna

DOTTORATO DI RICERCA IN

CHIMICA

Ciclo XXIX

Settore Scientifico Disciplinare: CHIM/03-B1

*Development of novel
multi-substituted apatite nanophases
with advanced functionalities for bone regeneration*

A dissertation by:

Alberto Ballardini

PhD candidate

Supervisor:

Prof. Giuseppe Falini

Co-supervisors:

Dr. Simone Sprio

Dr. Andrea Ruffini

D.ssa Anna Tampieri

PhD coordinator:

Prof. Aldo Roda

Esame finale anno 2017

CONTENTS

SUMMARY	7
1. INTRODUCTION.....	10
1.1. Human skeleton	10
1.1.1. Types of bone	11
1.1.2. Bone composition and morphology	12
1.1.3. Bone cells	14
1.1.4. Bone modeling and remodeling	15
1.1.5. Mechanical properties of bones.....	16
1.2. Bone substitutes.....	18
1.2.1. Bone problems and disease	18
1.2.2. Characteristics of the ideal bone substitutes	20
1.2.3. Current solutions	23
1.3. Calcium phosphates	26
1.3.1. Tricalcium phosphate	27
1.3.2. Hydroxyapatite	30
1.4. References	39
2. CHARACTERIZATION METHODS	46
2.1. X-Ray Diffraction (XRD).....	46

2.2.	Inductively Coupled Plasma Optical Emission Spectroscopy (ICP-OES).....	52
2.3.	Fourier Transform Infrared Spectroscopy (FTIR).....	54
2.4.	Scanning Electron Microscopy (SEM) and Energy-Dispersive X-ray spectroscopy (EDX).....	56
2.5.	Specific Surface Area (SSA-BET)	59
2.6.	Porosity.....	61
2.7.	Thermo-Gravimetric analysis (TGA).....	62
2.8.	Mechanical characterization.....	63
2.9.	References	65
3.	SYNTHESIS OF MULTISUBSTITUTED APATITIC PHASES WITH ANTIBACTERIAL ACTIVITY.....	67
3.1.	Materials and methods.....	70
3.2.	Gallium-doped multisubstituted hydroxyapatite nanophases.....	76
3.2.1.	Synthesis.....	76
3.2.2.	Chemical characterization.....	78
3.2.3.	Ion release test.....	85
3.2.4.	Biological characterization.....	87
3.2.5.	Antibacterial test	89
3.2.6.	Discussion	91
3.2.7.	Conclusion.....	96
3.3.	Zinc-doped multisubstituted hydroxyapatite nanophases.....	97
3.3.1.	Synthesis.....	97
3.3.2.	Chemical characterization.....	99

3.3.3.	Ion release test.....	106
3.3.4.	Biological characterization.....	107
3.3.5.	Antibacterial test	109
3.3.6.	Discussion	112
3.3.7.	Conclusion.....	115
3.4.	References	117
4.	STRONTIUM SUBSTITUTED HYDROXYAPATITE AS COATINGS FOR POLY ETHER ETHER KETONE (PEEK)	123
4.1.	Introduction	123
4.2.	Materials and Methods	126
4.3.	Results and discussion.....	130
4.3.1.	Sr ²⁺ -substituted CaP powders.....	130
4.3.2.	Sr ²⁺ -substituted CaP targets	137
4.3.3.	Sr ²⁺ substituted CaP coatings on PEEK	138
4.4.	Conclusions	147
4.5.	References	148
5.	HIERARCHICALLY STRUCTURED BIOMIMETIC SCAFFOLD FOR REGENERATION OF LOAD BEARING BONES.....	156
5.1.	Introduction	156
5.2.	Materials and Methods	160
5.2.1.	Scaffold production.....	160
5.2.2.	Materials characterization	164

5.2.3.	Biological evaluation.....	166
5.3.	Study and optimization of the reaction kinetics related to controlled phase transformations in 3-D biomorphic templates	169
5.3.1.	Pyrolysis	169
5.3.2.	Carburization.....	174
5.3.3.	Oxidation.....	178
5.3.4.	Hydration.....	182
5.3.5.	Carbonation	184
5.3.6.	Phosphatization	188
5.4.	Characterization of the final apatitic scaffold.....	191
5.4.1.	XRD analysis.....	191
5.4.2.	Chemical composition.....	192
5.4.3.	Microstructure	193
5.4.4.	Specific surface area (SSA).....	195
5.4.5.	Porosity.....	195
5.4.6.	Mechanical properties	197
5.4.7.	Ion release	199
5.5.	In vitro characterization.....	201
5.6.	Conclusions	205
5.7.	References	206
6.	Final conclusions and future perspectives.....	210
7.	Acknowledgments	212

SUMMARY

The research activity described in the present thesis is dedicated to the development of innovative phases of substituted hydroxyapatite (HA), $\text{Ca}_{10}(\text{PO}_4)_6(\text{OH})_2$. These new materials are addressed to the regeneration of bone tissue and was mainly carried out at the Institute of Science and Technology for Ceramics, belonging to the National Research Council of Italy (ISTEC-CNR), during my PhD in Chemistry.

In the last decades the biomaterials regenerative field has become a major area of material science and biomedical research. For the research of novel materials addressed to the regeneration is necessary an interdisciplinary approach spanning from the field of chemistry, engineering, medicine and biology.

In the field of bone substitutes is highly researched an innovative material able to fill gaps with mechanical performances suitable to sustain body and permit an active life. In addition the ideal material must stimulate cell response to the regeneration of new bone matrix, acting as scaffold, and permitting the complete restoration of the bone portion.

In fact, the currently used bio-inert devices (e.g. metallic devices) can merely provide a mechanical support without regenerating the damaged bone tissue often inducing adverse side effects while forcing the patient to frequent revision surgeries, with also relevant socio-economic impact. In this respect, the synthesis of new bioactive synthetic materials able to mimic the

compositional, morphological and mechanical features of bone is considered as the elective approach for effective tissue regeneration.

Calcium phosphates, in the form of hydroxyapatite, are the main component of the inorganic part of bone. For its biomimetical properties HA was chosen as subject of investigation. Additionally ionic substitution can be performed in the apatite lattice producing different effects, depending from the selected ions. Magnesium, in substitution of calcium, and carbonate, in substitution of phosphate, extensively present in the biological bones, are able to improve properties naturally present in the apatitic phase, (i.e. biomimicry, solubility e osteoinductive properties). Other ions can be used to give new useful properties to the apatitic phase. Strontium in substitution of calcium can confer to HA antiresorptive properties, useful to treat osteoporotic patients. Zinc and Gallium can substitute calcium, providing to HA antibacterial properties, inhibiting the formation of biofilms when used as implant.

After a general introduction of bone tissue physiology and an overview on the analytical methods involved in the research (Chapter I and Chapter II, respectively), this thesis focused on the development of hydroxyapatite nanophases with multiple ionic substitutions including for the first time gallium, or zinc ions, in association with magnesium and carbonate, with the purpose to provide double functionality as osteogenic and antibacterial biomaterial (Chapter III). The novel materials showed enhanced antibacterial effects that were evaluated in collaboration with University of Ferrara.

In Chapter IV were developed of bioactive materials based on Sr-substituted hydroxyapatite in the form of sintered targets. The obtained targets were treated with Pulsed Plasma Deposition (PED) resulting in the deposition of thin film coatings able to improve the roughness and wettability of PEEK (poly-ether-ether-ketone), a promising polymeric material for prosthetic

applications, enhancing its osteointegrability. This activity has been carried on in collaboration with IOR (Istituto Ortopedico Rizzoli), Bologna.

Finally, in Chapter V, were investigated heterogeneous gas-solid reactions, addressed to the biomorphic transformations of natural 3D porous structures into bone scaffolds with biomimetic composition and hierarchical organization, for application in load-bearing sites. This research was carried out in collaboration with GreenBone Ortho s.r.l., Faenza (RA). The kinetics of the different reactions involved in the transformation process were optimized to achieve complete and controlled phase transformation, with maintenance of the original 3-D morphology at the multi-scale. Finally, massive porous scaffolds made of ion-substituted hydroxyapatite and bone-mimicking structure were developed, that were tested and assessed in 3-D cell culture models in bioreactor and in clinically relevant animal model, in collaboration with IOR (Istituto Ortopedico Rizzoli), Bologna.

1. INTRODUCTION

1.1. Human skeleton

The human skeleton is the internal framework of the body. In the adult is composed of 250 bones at birth that were reduced to 206 bones in the adulthood after some bones are fused together. The human skeleton has six different function:

1) support: the skeleton is the framework that, associated with ligaments and muscles, support the body and maintain the shape.

2) movement: the joints between bones allow movement. Movements are powered by skeletal muscles, attached to the skeleton with ligaments at various sites. Muscles, bones and joints provide the principal mechanics for movement.

3) protection: bones protect many vital internal organs from being damaged. Particularly skull protect brain, vertebrae protects the spinal cord and the rib cage and the sternum protects lungs, heart, the major blood vessels and liver.

4) production of bone cells and lymphocytes: the bone marrow is the site in which red blood cells are produced in a process called hematopoiesis. The bone marrow is contained in the head of long bones and is also responsible of the production of lymphocytes, a support of the immune system [1] [2].

5) storage of minerals: bones are composed mainly of calcium phosphate and are involved in calcium metabolism. Instead bone marrow contains ferritin, involved in iron homeostasis.

6) endocrine regulation: bone cells have the possibility of release osteocalcin, a hormone involved in the insulin regulation, in the release of sugar and in fat deposition [3].

Bones need to have a lot of different and contrasting properties to fulfill their functions. They have to be light enough to avoid overloading of the body but strong enough to protect it. It must be hard to avoid breakage but porous in order to host cells within it and can be repaired. The human skeleton is able to combine these different features, thanks to its particular structure and morphology, hierarchically organized, able to distribute the individual loads on many different points and composite, that is formed from different materials able to give them different properties.

1.1.1. Types of bone

According to the different and specific role in the body, bones could have different shape. In human body there are 5 different type of bones: long, short, flat, irregular and sesamoid.

Long bones have elongated shape, that has the function of maintain the correct distance between the different part of the body and support the weight of the body. Long bones are composed of two different parts, a central elongated part, called diaphysis, a middle tubular part composed of compact bone which surrounds a central marrow cavity which contains red or yellow marrow and fat tissue, and two rounded heads, called epiphysis, that is filled with red bone marrow, which produces erythrocytes. Example of long bones are femur, humerus and tibia.

Short bones are almost cubical bones with a function of support of the weight. Short bones are concentrated in ankles, like the tarsus, and wrist, like carpus. Short bones do not have a cavity and does not contain marrow.

Flat bones have a planar shape. The function of those bones is the protection of organs and providing a broad surface for muscular attachment. They are composed of two layers of planar compact bones enclosing between them a strait of cancellous bone, containing red marrow,

responsible for the creation of new red blood cells. Examples of flat bones are the cranium, the ilium and the rib cage.

Sesamoids are small bones located almost in the joints. They act like pulleys, providing a smooth surface for tendons to slide over and their shape depends from the strain which they are subject [4].

Irregular bones cannot be grouped as long, short, flat or sesamoid bones. Irregular bones serve various purposes in the body, such as protection of nervous tissue, affording multiple anchor points for skeletal muscle attachment. They consist of cancellous tissue enclosed within a thin layer of compact bone.

1.1.2. Bone composition and morphology

From a chemical point of view bones are composed of two distinct phases, an organic matrix ($\approx 30\%$) and an inorganic part ($\approx 70\%$), adherent on the organic matrix. The organic matrix is composed mainly of type I collagen (up to 95%) and ground substances, like glycosaminoglycans (most notably hyaluronan), proteoglycans, and glycoproteins. The type I collagen is composed of three left handed procollagen fibers join to form a right handed triple helical called tropocollagen. The organic matrix confers to bones their elasticity and resistance to fracture. On the organic matrix is deposited an inorganic part, composed of calcium phosphates, mainly hydroxyapatite nanocrystals, that guarantee hardness to bones [5]. (see **Figure 1.1.**)

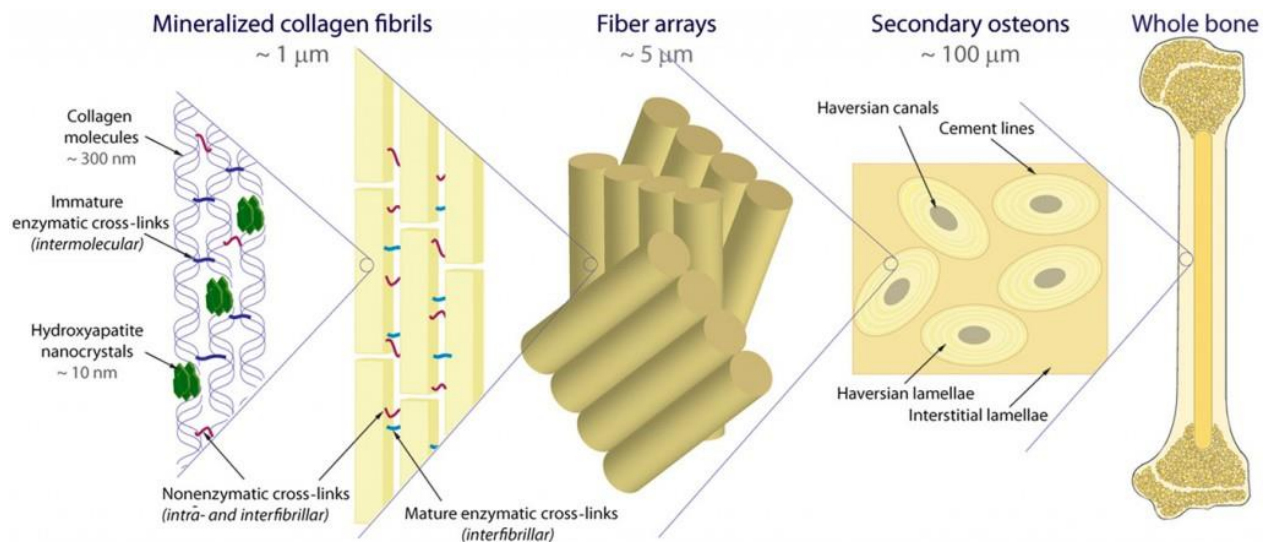


Figure 1.1. Hierarchical structure of bones (from: <http://newscenter.lbl.gov>)

From a histological point of view there are two different bone tissues, compact and cancellous. Compact bone is found in the external part of bones, is more solid and less porous than cancellous. The structure of the compact bone is composed of dense and concentrically arranged bony trabeculae or lamella and is characterized by the presence of haversian system. Compact bone, for its characteristic, has high mechanical properties and is responsible of the strength of bones. Cancellous bone instead is found in the inner part of bones and has a less organized architecture than compact bone. It has a lattice-work pattern with numerous cavities and is composed of trabeculae, with no haversian system. For its characteristics it's the place where almost of the vital processes of bones occur.

Particularly interesting are the haversian system and the trabeculae. The haversian system, or osteon, is the fundamental structure of the compact bones and is generally several mm long and about 0.2mm of diameter. Each osteon is characterized of numerous concentric layers (5-20), or lamellae, of compact bone tissue that surround a central canal, the haversian canal that contains the bone's blood supplies. Blood vessels in the different osteons are connected each other through oblique channels, called Volkmann's canals [6]. Instead in the cancellous bone lamellae are not

organized concentrically but in a disordered manner that leaves communicating cavity in bone matrix, that are occupied by nerves, bone marrow and blood vessels. The distribution of the lamellae in cancellous bone is not casual but are aligned depending from mechanical solicitation of bone [7].

1.1.3. Bone cells

There are four different types of differentiated bone cells, osteoblasts, osteoclasts, lining cells and osteocytes.

Osteoclasts are very large multinucleate cells that are responsible for the resorption of bones, a very important process in bone health allows for bone remodeling. Osteoclasts are formed by the conjoining of many different cells created from the bone marrow and it is possible found them grouped in the small pits on bone surfaces called Howship's lacunae. The pits are sites of bone resorption. In this sites osteoclasts release of proteolytic enzymes and acids which dissolve bone and result in calcium and phosphorus ions. Obviously the process of bone remodeling is activated by hormones in the bloodstream.

Osteoblasts have the role of deposit new bone matrix and regulate osteoclasts. Osteoblasts are mononuclear and smaller respect to osteoclasts. They are not terminally differentiated specialized cells. They are characterized by a large Golgi apparatus and an abundant rough endoplasmic reticulum. Osteoblasts can form tight connection with the adjacent osteoblast cells. First, the osteoblast create a framework of collagen fibers around it. Then the osteoblast release calcium and phosphate ions which naturally precipitate forming hydroxyapatite, attached to the collagen matrix. So osteoids are formed and the osteoblast could be trapped inside the osteon or could be outside the osteon. When the osteoblast becomes trapped, it becomes an osteocyte. Other

osteoblasts remaining outside the osteon are called lining cells and are used to protect the underlying bone.

Osteocytes are the most common cells in bone. They are embedded in osteons, residing in a lacuna and are connected with other osteocytes through extension of their plasma membrane inside canaliculi. The mechanical loads of bone induce low of liquid inside the canaliculi, favoring signal transmission. All the function of osteocytes are not well understand but their ability to modify through mechanical loads induce to think they could act as mechanosensor, regulating the bone remodeling [8].

Lining cells are flat, almost inactive, osteoblast. They are responsible for the protection of bones from chemical substances and are able to regulate calcium homeostasis in blood.

1.1.4. Bone modeling and remodeling

It is clear from the great number of cells living early presented that bones are complex living structures, finely regulated. There are different levels of complexity, at a chemical level the composition is important in the signaling, at a structure level the hierarchical disposition can guarantee the right level of mechanical strength and porosity, at a biological level the different types of cells can modify bone modifying it according to the different stimuli. This complexity allow them to adapt to the different situations, metabolic need and structure demands. There are two different main processes that occur in bones, modeling and remodeling. With remodeling is considered the process of turnover, always present in bones, related to bone maturation, skeletal maintenance and calcium metabolism. Continuous bone remodeling is also the cause of bone ageing. With the continuous dissolution-reprecipitation, hydroxyapatite tends to become more stoichiometric, losing calcium deficiency and ionic substitution, becoming more fragile. With

remodeling is instead considered the change of structure of bones due to mechanical strain or wounding, like healing from fracture, disuse atrophy or overload hypertrophy. Bone remodeling is divided in steps, fully regulated. (**Figure 1.2.**)

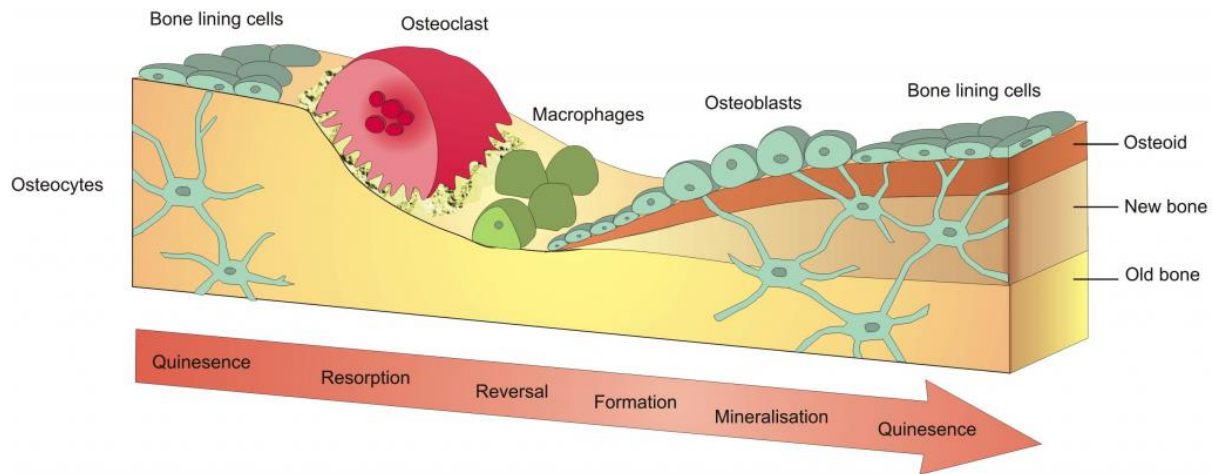


Figure 1.2. Schematic view of the different steps of bone remodeling (from: <http://precisionnutrition.com>)

The remodeling process starts with the resorption phase, with the differentiation of osteoclasts and their activity of bone resorption, forming an Howship lacuna. Then there is a reversal phase in which osteoclast are inactivated and pre-osteoblasts and a line of mononuclear cells are attached to the surface of the lacuna. In the final phases of the remodeling, osteoblast deposit layers of osteoids, filling the cavity, and the osteoblast cells could differentiate in osteoclast or lining cells, depending from the position.

1.1.5. Mechanical properties of bones

The mechanical properties of bones strongly depend on their hierarchical architecture, especially in the cortical bone. The particular structure of osteon has the ability to distribute the total mechanical strength on all the elements of the structure. Moreover their arrangement depends on

the direction of the mechanical to which they are subjected, which makes cortical bone an anisotropic material, varying its properties when loaded in different directions. For long bones stiffness is maximal for axial loads and minimal for perpendicular loads. (**Figure 1.3.**) The difference between the value is sensible because for cortical bone the axial compressive strength value is about 190MPa while for transverse loading the value decrease to 130MPa [9].

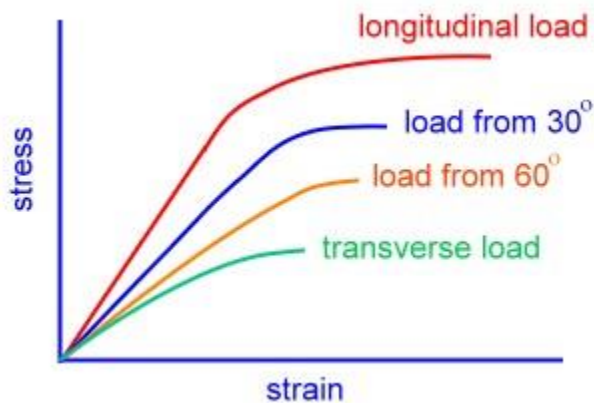


Figure 1.3. Effect of bone anisotropy: different loading curves, from longitudinal to transverse orientation [10].

Bone also have a viscoelastic behavior. A material is called viscoelastic if its mechanical properties depend on the speed whereby the load is applied and its persistence. In the case of bone, it is more resistant to fracture for high speed and low persistent loads.

Depending from the load, bone can have two different behavior. (**Figure 1.4.**) For small load it has an elastic response, in which also for high load there is small deformation and, if the load is removed, bone goes back to its original shape and measure. Increasing the load, passing the yield point, the behavior becomes plastic, there are big deformation also for small increase of loads and the deformation is permanent (hysteresis). The load can be increased continuously until is reached the failure point, after which the bone does not retain the original shape. Materials exhibiting only elastic behavior are called brittle while materials whose behavior is mainly plastic

are called ductile. Bones have both of those behaviors because it is a composite material, in which collagen is weak and ductile and hydroxyapatite is strong and brittle [11].

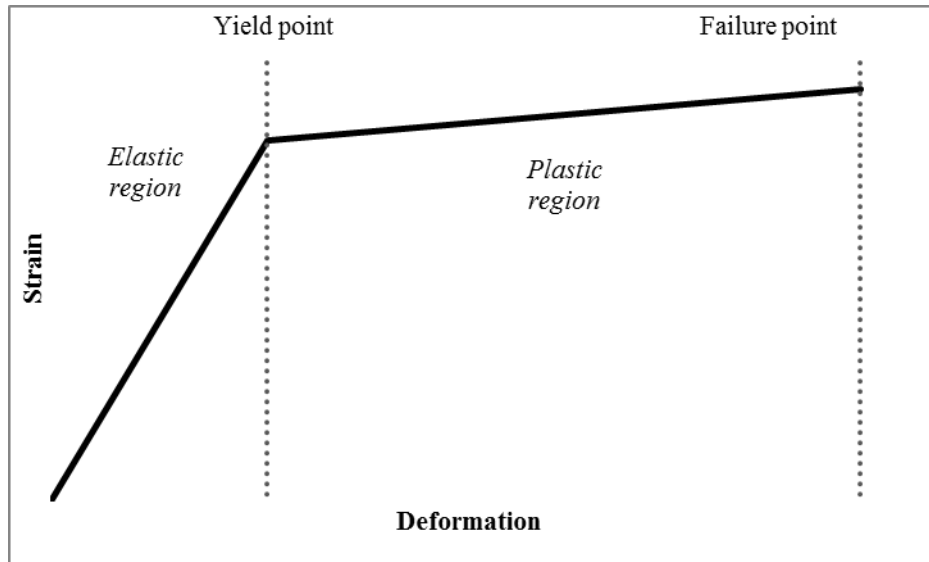


Figure 1.4. A typical stress/deformation curve where it is possible to see the two behavior of bone.

1.2. Bone substitutes

1.2.1. Bone problems and disease

As it has seen in the previous paragraphs, because of their typical structure and the ability of cells of repair bone damage, the healing of bone is often spontaneous and autonomous. It is usually only necessary the reduction of the fracture to realign the two stumps of the bone. For normal, small fracture it is necessary only immobilizing the fractured bone and the healing will come spontaneously.

However there are also cases in which the body alone is not able to repair the damage it has suffered. In case of displaced fractures, in which the pieces of fractured bone are not in place, an

operation is required immediately after the trauma to put the pieces of bone in axis and ensure healing. If the bone is broken into several parts, often due to a particularly traumatic event, it is necessary to hold together the different pieces using screws. If the bone is ground into very small pieces, it is no longer possible to keep them together and it becomes necessary to surgically remove fragments and insert in their place a bone substitute.

Also several serious diseases may affect bone tissue, making in many cases necessary to intervene in surgical manner. One of the most common diseases that affects the bones is osteoporosis. The probability of incurring osteoporosis increases with age and, by increasing the average life expectancy, it will be a more and more frequent pathology. Osteoporosis is a disease characterized by decreased bone mass and microarchitectural deterioration of bone tissue. The cause is to be found in an imbalance between the activity of osteoclasts, which resorb bone, and the osteoblasts, which deposit it in favor of the first. This results in an increase in bone fragility and thus the risk of fractures. Also, the healing of fractures, because of the poor activity of osteoblasts, is slower and more difficult. In extremely severe cases the healing of fractures becomes impossible and it is necessary the introduction of a bone substitute. To restore the balance between the activity of osteoclasts and osteoblasts, several drugs have been developed, such as hormones, bisphosphonates, vitamin D. Particularly relevant in antiosteoporotic therapy is the use of strontium ranelate which acts in two different directions and therefore it is called DABA (Dual Action Bone Agent). Strontium ranelate leads to the differentiation of pre-osteoblast to osteoblast which increases the bone formation. It also inhibits osteoclasts formation from pre-osteoclasts, which leads to the decrease of bone resorption [12].

Another serious disorder in bone metabolism is Paget's disease of bone. It was found in approximately 3% of the population over age 40, with a preference of 50% to men than women

[13]. The disease is caused by a virus, paramyxoviridae, but its activity is favored by genetic and environmental factors. The disease causes an excessive turnover of bone, followed by disorganized bone remodeling. This results in pain, misshapen bones, fractures and arthritis in the joints near the affected bones. Often Paget's disease is localized to only a few bones in the body, commonly the pelvis, femur, and lower lumbar vertebrae. Rarely, it can develop into a bone tumor known as Paget's sarcoma [14]. The more commonly used drugs to treat Paget's disease are bisphosphonates and calcitonin. In the more serious cases it has necessary a surgical intervention for bone deformity remodeling or the reduction of the fracture caused by this disease.

Another subject is related to bone tumors. There are 4 types of cancers that can affect the skeletal system, osteosarcoma that develops inside the bones [14], chondrosarcoma that originates from cartilage [15], Ewing's sarcoma, which develops from immature nerve terminations of the bone marrow [16] and metastatic tumors, due to metastases in the bones resulting from tumors in other parts of the body. The 3 tumors arising directly from the bones are not particularly frequent while bones are one of the most commonly organs affected from engraftion and the proliferation of cancer metastases. For all 4 cases, the treatments are the same, chemotherapy, radiotherapy, generally not very effective, and surgical intervention, for physically removing the bone portion containing the cancerous cells. Treatments are often performed simultaneously to treat the same tumor.

1.2.2. Characteristics of the ideal bone substitutes

When a part of bone is so damaged that has to be removed, an object has to be inserted to maintain the correct space between the various part of the body and give mechanical support to the body, restoring the mobility.

Actually a solution commonly adopted in the clinical procedure is the use of natural bones. Three different type of natural bones can be used. Autograft transplant consists in the removal of part of one bone of the patient, usually iliac crest, and its insertion in the damaged site [17]. It is usually considered the gold standard for its safety and regenerative properties. However can cause morbidity in the site from which the bone is take and the quantity of bone that can be withdrawn is limited. Allograft implant consist in the use of bones from human cadaver [17]. However before the implant bones have to be sterilized and conserved in special bone banks, with very expensive procedure. Respect to autograft, allograft implants is less safe and less regenerative but guarantee a larger quantity of material without damages for the patient. Xenograft implant consist in the use of bone materials from another species, commonly bovine or porcine, freeze dried and deproteinized [18]. Xenograft allows a greater availability of the material at the expense of a lesser biocompatibility. Another possibilities is the use of synthetic bone grafting.

This is the field of prosthetic. The goal for prostheses is the complete rehabilitation of the patient and the restoration of use of the damaged bone, bringing him back to of an active life.

A perfect prostheses has to match up a lot of characteristics.

- **Mechanical properties.** The mechanical strength to compression and the Young modulus of the implant have to be similar to the one of natural bone. Those characteristic permit a rapid restarting of the movement, inhibiting bone resorption and favoring bone turnover [19].
- **Porosity.** An high porous structure permit to cells and liquids to infiltrate into all the length of the scaffold, allowing the colonization of all the scaffold. The porosity not only need to be elevate but two other fundamental characteristics, *interconnection*, every pore

need to be colligated with another, and the *dimension*. If the objective is cells infiltration and their growth inside the scaffold it will be necessary a macroporosity in the order of magnitude of hundreds micron (100-300) allowing cells inflow and a microporosity, in order of magnitude of some micron, allowing the interchange of liquids and signals between cells and blood flow [20].

- **Properties of the surface.** From literature it has been proved that for favoring the attachment of cells and their proliferation has been favored by the roughness of the material [21] [22]. Depending from the material of which the implant is composed there are different methods to improve the roughness of the surface. For plastic and metallic prostheses the roughness of the material is improved by chemical reaction or by coating with a rough material. For ceramic materials the roughness of the surface is connected with the crystallinity of the material. A low crystallinity is connected with high surface area and roughness of the material.
- **Osteoinductive.** Means the capacity of recruitment of immature cells and the stimulation of these cells to develop into preosteoblasts [23]. Is the same process involved naturally in bone healing from fracture
- **Osteoconductive.** Means that bone can grows and proliferate on the surface of the material [24].
- **Osteointegrative.** Is the stable anchorage of an implant achieved by direct bone-to-implant contact [25].
- **Angiogenetic.** Means the capacity of the prostheses of promoting the formation of new blood vessels and their penetration into the prostheses [26]. Blood vessels are

fundamental for making all the prostheses habitable to the cells, not only the surface, providing the correct provision of nutrients.

- **Resorbable.** The prostheses has to be dissolved sometimes after the implantation. The dissolution rate has to be similar with the deposition of new bone. If the dissolution was made by the cells and the materials of which it is composed have to be used in the healing process the properties is called **bioresorbability** [27].

When all those characteristic are present in one scaffold its fate is the complete regeneration of an active bone once inserted in the body.

1.2.3. Current solutions

The first bone implants are traceable to early Egyptians, China and South Central American cultures, using stone or ivory to replace teeth [28]. From this era there were a development in material and biological science. At the moment the materials used for bone grafting are divided into three main different groups, metallic, polymeric and ceramics.

1.2.3.1. Metallic implants

Metals have biomechanical properties which made them suitable as an implant material. Besides these properties metals are also easy to process and it is possible to product them in every shape. Metallic implants can be sterilized by the common sterilization procedure which makes them easy to use. The first metals used were gold, stainless steel and cobalt-chromium but, due to advancements with time and low success rates with these metals, they materials have now become obsolete and are now replaced by newer ones. Titanium (Ti) and its alloys (mainly Ti6Al4V and Ti6Al7Nb) have become the most common metals for implants.

Titanium has a good record of being used successfully as an implant material and this success with titanium implants is credited to its excellent mechanical properties and its biocompatibility due to the formation of stable oxide layer on its surface [29].

Titanium reacts with several other elements for eg: silver, Al, Ar, Cu, Fe, Ur, Va and Zn to form alloys. Titanium alloys exists in three forms alpha, beta and α - β . The alloys most commonly used for implants are of the alpha-beta variety. The most common contains 6% Al and 4% Va (Ti6Al4V) or 6% Al and 7% Nb (Ti6Al7Nb) [30].

Despite their great biocompatibility, their excellent mechanical properties and their workability, metallic implants were not resorbable and after a period of time requires surgical intervention for substitution of the implant because of the corrosion.

1.2.3.2. Polymeric implants

A lot of different synthetic or natural polymer are widely used for bone grafting. The properties of the implant differs depending from the polymer selected. Generally polymers have different advantages. The physical characteristics of the polymers can be altered based on their use as their composition may be changed easily. Polymers can be changed in to more porous or softer form. Polymers can be manipulated easily and allow better reproduction. They show fibrous connective tissue attachment. Depending from the polymer used, they are usually resorbable. They are plastic and easily moldable, also in 3D printing. However there are some disadvantages in the use of polymer. Their mechanical properties are not adequate. They lack of adhesion to living tissues and can generate adverse immunologic reactions.

The more common polymers used are polylysine (PLL), Poly (L-lactic acid) (PLLA), poly(lactic-co-glycolic) acid (PLGA), silk, chitosan and collagen [31]. Recently an innovative polymeric

material has aroused great interest because is capable of combining great resistance to corrosion with light weight and elevate mechanical properties, Polyether ether ketone (PEEK).

1.2.3.3. Bioceramics

Another possibilities for bone grafting is the use of bioceramics. They are resistant, anticorrosive, biocompatible, ostointegrative and generally well accepted by the body. However they are usually brittle, rigid and not resorbable. The bioceramics commonly utilized comprendono metal oxides, like aluminum oxide (Al_2O_3), zirconium oxide (ZrO_2) and titanium oxide (TiO_2), bioglasses, that contains various amount of SiO_2 (30-60%), P_2O_5 (2-15%), CaO and/or CaF_2 (20-40%) and Na_2O (5-25%), alumino-silicates and calcium phosphates. Depending from the uses one material can be considered more suitable than another.

As well as unique materials that make up the implant, the bioceramic can also be used in addition to previously described materials.

It is possible combining the ceramic materials with metals, covering the surface of the metallic implant with a ceramic coating, thus ensuring to the final device the mechanical properties of the metal with osteointegrative properties and corrosion resistance properties of the ceramic. Also altering the surface properties of metallic implant, increasing its roughness, it is possible ensuring a greater adhesion of cells to the surface and to decrease the probability of dislocation of the prosthesis [32].

It is also possible combining the ceramic materials with polymeric materials, thus going to strengthen the poor mechanical properties of polymeric materials. Of particular interest are biodegradable polymers that, with the synergic interaction of osteoinductive ceramics, could be slowly replaced by new bone, restoring the lost part of bone or cartilage..

1.3. Calcium phosphates

Among bioceramic materials of particular importance are the calcium phosphates. These are composed of calcium, phosphorus and oxygen as fundamental elements. Calcium is an essential ion in the human body that, in an adult, contains approximately 1100g of calcium. Normally 99% of calcium present in the body is contained in bones but could also be complexed with proteins, like albumin or globulin, with anions, like bicarbonate, lactate or sulphate, or in the free ionized form. In combination with phosphate calcium is the main component of bones and teeth. Phosphorus is an essential element in the body, that mass about 1% of the total weight of the body. It is used in a large number of molecules like DNA and ATP and, in combination with calcium is the main component of human bone and teeth.

Despite their composing elements are the same calcium phosphates differ for composition, the more important parameter for the composition is the Ca/P molar ratio, crystal geometry, and biological effects. The different composition involve diversification of the chemico-physical properties between the different compounds. Among these one of the most important is the solubility, which will influence the degree of resorption of the material once implanted.

The most common calcium phosphates are:

Monocalcium phosphate (MCP), $(\text{Ca}(\text{H}_2\text{PO}_4)_2)$, Ca/P=0.5. Is the more acid and more soluble ($K_s=1.14$) among all calcium phosphates It can be monohydrated or anhydrous. It is not biocompatible and it is widely used as fertilizer.

Dicalcium phosphate dehydrate (DCPD), $(\text{CaHPO}_4 \cdot 2\text{H}_2\text{O})$, Ca/P=1. It is soluble ($K_s=6.59$) and for this reason is used as bone cement. It has the mineralogic name of brushite. It can be also as anhydrous form and is called dicalcium phosphate dehydrate or with the mineralogic name of monetite (DCPA, CaHPO_4)

Octacalcium phosphate (OCP), $(Ca_8(HPO_4)_2(PO_4)_4 \cdot 5H_2O)$, Ca/P=1,33. It is an insoluble form of calcium phosphate ($K_s=96,6$) that is considered the promotor of calcium phosphates precipitation.

Tricalcium phosphate (TCP), $(Ca_3(PO_4)_2)$, Ca/P=1.5. It is one of the most important calcium phosphates. It exist in two different polymorphs, α and β , where the α is stable only at high temperatures. The solubility differs significantly from α to β and the α polymorph result much more soluble.

Hydroxyapatite (HA), $(Ca_{10}(PO_4)_6(OH)_2)$, Ca/P=1.67. It is the ost studied calcium phosphates because is the main component of the mineral part of human bone and is one of the most insoluble form of calcium phosphates.

Amorphous calcium phosphate (ACP), Ca/P=1.2-2.2. It has not a crystalline structure or a defined formula. It is more soluble than α -TCP.

Tetracalcium phosphate (TTCP), $(Ca_4(PO_4)_2O)$, Ca/P=2. It is the most basic of all the calcium phosphates and the one with the highest Ca/P ratio. It is stable at high temperature ($\geq 1300^\circ C$) and is partially soluble ($K_s=42$) [32].

In the next paragraphs we will speak deeply about two of the most important calcium phosphates, tricalciumposphates and hydroxylapatite.

1.3.1. Tricalcium phosphate

Tricalcium phosphate (TCP) is a compound with formula $Ca_3(PO_4)_2$ and Ca/P molar ratio of 1,5. It is partially soluble ($K_s=20-30$). It exist in three polymorphs, α , α' and β but only α and β are commonly used. α' -TCP is not widely studied because it can be obtained only at temperature superior to $1430^\circ C$ and immediately reverts to α -TCP when the temperature decreases.

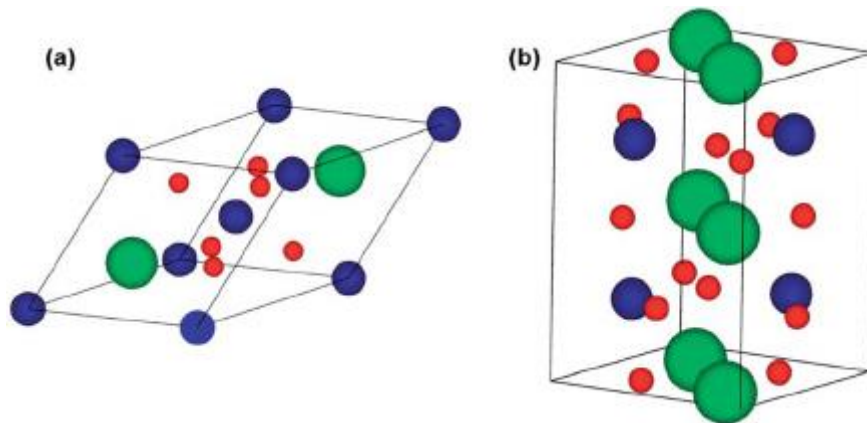
α -TCP has a monoclinic crystal structure and is stable only at high temperature ($\geq 1125^{\circ}\text{C}$) and for this reason is synthesized for heating at high temperature of β -TCP or of a mixture calcium pyrophosphate or monetite with calcium carbonate to obtain a Ca/P molar ratio of 1,5. The heating is followed by a quenching, avoiding the transformation of the α phase to β . It is more soluble than β and its higher solubility bring to a dissolution reprecipitation process able to deposit hydroxyapatite in situ. The deposited hydroxyapatite have the shape of needles, entangled together and for this reasons is studied as bone cement [33] [34].

β -TCP is more stable and less soluble than α . It has rhombohedral structure. It can be synthesized with a wet reaction by precipitation from a solution of two soluble salts, a phosphate, like $(\text{NH}_4)_2\text{HPO}_4$ and a calcium salt, like $\text{Ca}(\text{NO}_3)_2$, in controlled chemical conditions. Using this technique it is possible to obtain a mixture of ACP, TCP and hydroxyapatite. Another technique for the synthesis of β -TCP is the high temperature synthesis, similar to the one to obtain α -TCP but followed by a slow cooling. The structure of TCP can easily accept a substitution of Mg or other cations in the site of Ca. When Ca is substituted with Mg the obtained mineral take the name of whitlockite ($(\text{Ca},\text{Mg})_3(\text{PO}_4)_2$), a mineral present in some rocks [35]. Whitlockite is less soluble than unsubstituted β -TCP.

β -TCP is widely studied because of its use as material for bone substitution. β -TCP can be used as unique material to create the bone substitute or mixed with hydroxyapatite, in the so-called biphasic bone substitutes. The mix between HA and β -TCP is used to combine the different properties of the two materials.

Table 1.I. Crystallographic properties of TCP polymorphs

<i>Property</i>	<i>β-TCP</i>	<i>α-TCP</i>	<i>α'-TCP</i>
Symmetry	Rhombohedral	Monoclinic	Hexagonal
Space Group	R3C	P21/a	P63/mmc
a (nm)	1.04352	1.2859	0.53507
b (nm)	1.04352	2.7354	0.53507
c (nm)	3.74029	1.5222	0.7684
α (°)	90	90	90
β (°)	90	126.35	90
γ (°)	120	90	120
Z	21	24	1
V (nm³)	3.5272	4.31	0.19052
V0 (nm³)	0.168	0.18	0.19052
D_{th} (g*cm³)	3.066	2.866	2.702

**Figure 1.5.** Crystal structure of β - (a) and α - (b) TCP.

1.3.2. Hydroxyapatite

1.3.2.1. Structure and chemistry

Hydroxylapatite (HA) is a composite with chemical formula $\text{Ca}_5(\text{PO}_4)_3(\text{OH})_1$ but usually written as $\text{Ca}_{10}(\text{PO}_4)_6(\text{OH})_2$ to indicate that the crystalline cell comprises two units and Ca/P molar ratio of 1,67. A stoichiometric hydroxyapatite has the following weight percentage composition: Ca 39,9%, P 18,5%, O 41,4% and H 0.2%. It is fundamental insoluble in water at pH=7 ($K_s=117$) but it can be easily solubilized in acidic condition, below 5 of pH. HA has a theoretical density of 3.16 g/cm^3 . It has an hexagonal cell with space group P63/m. It has two different length for its axis ($a=b=9.421\text{\AA}$, $c=6.881\text{\AA}$ and $\gamma=120^\circ$) [Posner AS, Perloff A, Diorio AF. Refinement of the hydroxyapatite structure. *Acta Crystallographica*. 1958;11:308-9.] and two different sites for Ca ions, 4f and 6h (in orange and green in **Figure 1.6.**). The common name for the two different position are Ca1 or Column Ca for the 4f position and Ca2 or triangular Ca for the 6h position.

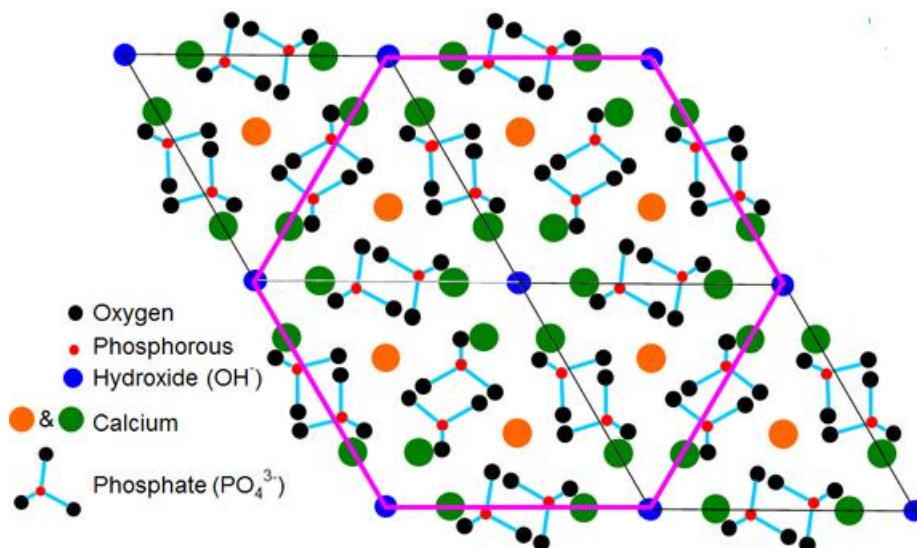


Figure 1.6. Crystallographic structure of HA. (from: <http://www.iupui.edu/~bbml/boneintro.shtml>)

1.3.2.2. Biological relevance

Nanocrystalline hydroxyapatite, as mentioned in the previous paragraphs, is the main component of the mineral part of human bones and teeth. Biological HA is non-stoichiometric because it contains foreign ions that can substitute Ca^{2+} , PO_4^{3-} and OH^- . The more important substituents are Mg^{2+} and Na^+ in the site of calcium, carbonate ion (CO_3^{2-}) silicate ion (SiO_3^{2-}) and HPO_4^{2-} in the site of phosphate and chloride (Cl^-) and fluoride (F^-) in the site of hydroxyl. In addition, biological hydroxyapatite can have some vacancies. The more important are calcium and hydroxyl vacancies, used to balance the charge difference in case of substitution with ions of different charge, like CO_3^{2-} or HPO_4^{2-} in the position of PO_4^{3-} . Substitutions and vacancies changes also the Ca/P molar ratio of bones. Furthermore the chemical composition differs between bone, enamel and dentine to perform better their specific function. The ionic presence of each ion is tabulated in **Table 1.2.**

Table 1.2. Atomic composition of bone, enamel dentine and stoichiometric HA [36].

<i>Atoms</i>	<i>Ions</i>	<i>Bone</i>	<i>Enamel</i>	<i>Dentine</i>	<i>Stoichiometric HA</i>
Calcium	Ca ²⁺	37.69	37.11	37.36	39.60
Phosphorus	P ⁵⁺	17.69	18.25	18.33	18.50
Carbonate	CO ₃ ²⁻	8.92	3.30	0.83	---
Sodium	Na ⁺	1.08	0.52	1.11	---
Magnesium	Mg ²⁺	0.85	0.45	0.08	---
Chloride	Cl ⁻	0.15	0.31	0.03	---
Potassium	K ⁺	0.05	0.08	0.14	---
Fluoride	F ⁻	0.03	0.01	---	---
Strontium	Sr ²⁺	0.03	0.14	0.03	---
Barium	Ba ²⁺	0.15	0.02	0.01	---
Lead	Pb ²⁺	0.12	0.10	0.01	---
Iron	Fe ³⁺	0.15	0.08	0.01	---
Zinc	Zn ²⁺	0.06	0.12	0.10	---
Copper	Cu ²⁺	0.15	0.01	0.01	---
Aluminum	Al ³⁺	trace	0.04	0.02	---
Silicon	Si ⁴⁺	0.08	0.14	0.01	---
Manganese	Mn ²⁺	trace	0.06	trace	---
Selenium	Se ²⁺	trace	0.00	trace	---
Tin	Sn ²⁺	trace	0.01	trace	---
Lithium	Li ⁺	trace	0.00	trace	---
Nichel	Ni ²⁺	trace	0.00	trace	---
Silver	Ag ⁺	trace	0.00	0.10	---
Sulfur	S ⁶⁺	trace	0.01	0.00	---
Cadmium	Cd ²⁺	trace	0.01	0.00	---
Ca/P		1.65	1.57	1.58	1.67
Inorganic fraction (%)		65	97	72	100

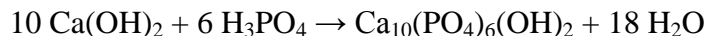
In addition, due to the remodeling action of cells, bone composition changes from a young person to an old person [37]. During ageing the biological hydroxyapatite tends to become less substituted, more stoichiometric and more crystalline. The reduced substitution and the increased crystallinity of older bones are reflected in a lesser solubility of apatite. The macroscopic effect of this change is the increased fragility of bones and the longer time of healing from fracture in the older age.

1.3.2.3.Synthetic routes

For its biological relevance, a great numbers of study are performed on hydroxyapatite and a great number of synthetic routes are developed. The more used are: precipitation technique, sol-gel approach, hydrothermal technique, multiple emulsion technique, biomimetic deposition technique, electrodeposition technique [38].

The **precipitation technique** is the most popular and widely researched technique for synthesis of HA. This technique is also called as wet precipitation or chemical precipitation or aqueous precipitation [39]. This technique is commonly chosen to synthesize HA because relatively large amounts of HA can be produced in absence of any organic solvents at a reasonable cost. Furthermore crystallinity, size, shape and surface area of the obtained crystals can be modulated modifying the parameters of the synthesis, such as temperature (0-100°C). The precipitation technique involved the reaction in aqueous solution or suspension of two different salt, one containing Ca and the other containing PO_4^{3-} by ensuring that the final Ca/P ratio is 1.67. The pH during the reaction must be controlled and maintained in basic condition, to avoid the formation of other phases, like brushite. The more used reagents containing calcium are $\text{Ca}(\text{OH})_2$ and $\text{Ca}(\text{NO}_3)_2$. The more common reagents containing phosphate are H_3PO_4 and ammonium phosphates ($(\text{NH}_4)_2\text{HPO}_4$ or $(\text{NH}_4)\text{H}_2\text{PO}_4$). In case of reaction of calcium hydroxide and

phosphoric acid the involved reaction is a neutralization and no other reagent for ensure that the pH is basic is required [40].



In the other cases it is necessary to adjust pH to maintain basic, using other reagents such as NH_4OH or urea. This synthetic route is frequently used also for its possibility to insert doping ions in the lattice during the precipitation.

The **sol-gel approach** guarantee, respect to the precipitation technique, a better control of the parameter of process and a major homogeneity of the mixing. Also in this case are used two different precursor, one containing calcium and the other the phosphate, setting the Ca/P molar ratio equal to 1.67. As calcium precursor are widely used calcium nitrate and calcium acetate and as phosphate reagents are commonly used organic compounds containing phosphorous, such as $\text{C}_6\text{H}_5\text{PCl}_2$, $\text{HOOCCH}_2\text{PO(OH)}_2$ or $(\text{C}_2\text{H}_5)_2\text{PO}_4$. The reagents were mixed and heated at high temperature (500-900°C) [41].

Hydrothermal synthesis is a process that utilizes single or heterogeneous phase reactions in aqueous solvent at elevated temperature ($T > 50^\circ\text{C}$) and pressure ($P > 100 \text{ kPa}$) to crystallize ceramic materials directly from solutions. It is particularly useful to convert scaffolds made of calcium carbonate, derived from corals [42] or wood [43], into HA. In this case as source of phosphate are used different phosphate salts, such as ammonium phosphates or potassium phosphates. Phosphoric acid could not be used in this case because is not possible to adjust the pH during the synthesis.



The **multiple emulsion technique** is an innovative route for the synthesis of HA that uses a water/oil/water (w/o/w) emulsion made of dipotassium hydrogen phosphate as inner aqueous

phase, benzene as oil phase and calcium nitrate as outer aqueous phase. This technique have the advantages of using a simple apparatus and can be carried out at room temperature [44].

The **biomimetic deposition technique**, differently from the precipitation technique, uses metastable synthetic body fluid to facilitate the spontaneous nucleation and growth of biomimetic hydroxyapatite. The obtained HA is more similar to biological one respect to the one obtained with a typical precipitation technique but could produce smaller amount of powder for each synthesis. This synthesis was developed for the creation of coating directly on the surface of the implant [45].

The **electrodeposition technique** is used to synthesise coatings of ultrafine-grained nanocrystalline HA using dilute solutions of calcium and phosphate and an electric field [46].

1.3.2.4. Ionic substitution

Hydroxyapatite has a crystalline structure that can easily accept ionic substitution, particularly when ions were introduced during the synthesis at low temperature. It is also possible to introduce ions in a HA already synthesized for ion exchange with an ion-rich solution. When an ion substituted HA is sintered, ions can be retained in the HA lattice, giving distortion of the crystal parameter, or remain as intercalating ions or be segregated in a side phase, usually whitlockite or the corresponding oxide.

There are two different purpose for ionic substitution. A first reason is improving the natural properties of the apatitic phase, like biomimicry and solubility. Another reason for the introduction of foreign ions is giving to HA new properties, such as antibacterial or anti-osteoporotic properties. Three of the more studied ions for substitution, are magnesium, strontium and carbonate, for their biological relevance [47] [48] [49].

Magnesium and strontium are cations of the same group of calcium in the periodic table of the elements, the second, alkaline earth metals. They have the same charge (2+) and a similar ionic radius (Mg^{2+} 86pm, Ca^{2+} 114 pm, Sr^{2+} 132pm) of calcium. For this reasons it is simple to understand that this cations can substitute calcium in HA. However their effects are different when inserted in the HA lattice. Magnesium can be inserted in HA during a low-temperature synthesis of the phase but create a β -TCP phase when is sintered. The effect of Mg on HA is a decrease of the crystallinity, a decrease in crystallite dimension and an improvement in its solubility [50]. Strontium doped HA can be easily synthesized and sintered without the formation of any side phase. The doping with Sr is useful because could provoke an in situ release of Sr ions that inhibits bone resorption, acting as anti-osteoporotic agent, without the side effect related to a systemic administration. A lot of other cations have been inserted, with different ionic radius and charge, like Zn [51], Ga [52], Mn [53], Fe [54], Na [55], Ag [56] or Cu [57]. When an ion with a different charge is introduced in the crystal, the restoring of the neutrality could involve other ions. It is possible to create a lacuna in the lattice with the removal of an ion or performing a concomitant substitution. The more involved ions are calcium and/or hydroxyls and/or carbonate.

Another important ion that is commonly found also in synthetic HA is carbonate. A spontaneous carbonation always occur when the synthesis is conducted in water without controlled N_2/Ar atmosphere. The carbon dioxide present in the air spontaneously dissolves into water, generating carbonate ions, that precipitate inside the apatite lattice. The carbonate ions can enter in the apatite lattice in two different position, A and B. In the A position the carbonate ion substitute the hydroxyl group while in the B position substitute the phosphate group. In biological hydroxyapatite is prevalent the B substitution and also biological in vitro tests reveals that the

substitution in the B position favors HA solubility and cells vitality and differentiation. The insertion of a carbonate ion in the place of a phosphate ion generate an unbalance of a negative charge. A proposed mechanism to balance the charge is the simultaneous loss of a calcium ion and of an hydroxyl group, recovering neutrality. In this case the obtained HA is carbonate substituted and calcium deficient, further increasing the solubility. Another proposed mechanism for charge balance is the simultaneous substitution of one calcium ion with a monovalent cation, like Na^+ , K^+ or NH_4^+ [58] [59]. Others anions can be substituted to phosphate like silicate, sulfate or selenium.

Also the hydroxyl group can be substituted in the HA lattice. The more common substitution is with the fluoride ion (F^-), forming fluorapatite [60]. The F^- substitution is commonly found in enamel and bone and has the effect of decreasing the solubility and increasing the resistance of teeth to dental caries. Also chloride can substitute the hydroxyl group, forming chlorapatite [61].

1.3.2.5.Porous scaffold

In addition to the chemical characteristic of the HA phase, a great importance is assumed by the 3D structure of the bone substitute. There are different methods to obtain a 3D porous scaffold. The more commonly used techniques are partial sintering, sacrificial fugitives, replica templates and direct foaming.

The **partial sintering** of powder is the most used method to generate porosity in a scaffold [62]. It consist in the sintering of a material at low temperature. The porosity is generated by surface diffusion or evaporation-condensation phenomena and lead to an homogeneous and controlled porosity.

The **sacrificial template technique** uses two different materials mixed to prepare a biphasic composite, composed of a continuous matrix of ceramic powders and a dispersed secondary phase. During sintering the secondary phase evaporate and leaves an high open porosity [63].

The **replica method** consist in the impregnation of an existing structure, normally polymeric, with a ceramic suspension. When the scaffold in sintered the polymeric structure evaporates and the ceramic matrix is consolidated, maintaining the same structure of the original template [64].

The **direct foaming method** consist in the incorporation of a gas (e.g. air) into a ceramic suspension, that is subsequently dried and sintered [65].

1.4. References

- [1] Birbrair A, Frenette PS. Niche heterogeneity in the bone marrow. *Annals of the New York Academy of Sciences* 2016;1370:82-96.
- [2] Adeyeye EI. Bone marrow: a source of nutritionally valuable fats as typified in the femur of ram and bull. *Open Journal of Analytical Chemistry Research* 2014;2:1-15.
- [3] Lee NK, Sowa H, Hinoi E, Ferron M, Ahn JD, Confavreux C, et al. Endocrine regulation of energy metabolism by the skeleton. *Cell* 2007;130:456-69.
- [4] Saladin KS, Miller L. *Anatomy & physiology*: WCB/McGraw-Hill; 1998.
- [5] Hall JE. *Guyton and Hall textbook of medical physiology*: Elsevier Health Sciences; 2015.
- [6] Cooper RR, Milgram JW, Robinson RA. Morphology of the osteon. *J Bone Joint Surg Am* 1966;48:1239-71.
- [7] Gdyczynski CM, Manbachi A, Hashemi S, Lashkari B, Cobbold RSC. On estimating the directionality distribution in pedicle trabecular bone from micro-CT images. *Physiological measurement* 2014;35:2415.
- [8] Chen J-H, Liu C, You L, Simmons CA. Boning up on Wolff's Law: mechanical regulation of the cells that make and maintain bone. *Journal of biomechanics* 2010;43:108-18.
- [9] Reilly DT, Burstein AH. The elastic and ultimate properties of compact bone tissue. *Journal of biomechanics* 1975;8:393IN9397-396IN11405.
- [10] Nordin M, Frankel VH. *Basic biomechanics of the musculoskeletal system*: Lippincott Williams & Wilkins; 2001.

- [11] Bankoff ADP. Biomechanical characteristics of the bone: INTECH Open Access Publisher; 2012.
- [12] Hamdy NA. Strontium ranelate improves bone microarchitecture in osteoporosis. *Rheumatology* 2009;48:iv9-iv13.
- [13] Fauci AS. *Harrison's principles of internal medicine*: Mcgraw-hill New York; 1998.
- [14] Tamparo CD. *Diseases of the human body*: FA Davis; 2016.
- [15] Gelderblom H, Hogendoorn PC, Dijkstra SD, Van Rijswijk CS, Krol AD, Taminiau AH, et al. The clinical approach towards chondrosarcoma. *The oncologist* 2008;13:320-9.
- [16] Iwamoto Y. Diagnosis and treatment of Ewing's sarcoma. *Japanese Journal of Clinical Oncology* 2007;37:79-89.
- [17] Goldberg VM, Stevenson S. Natural history of autografts and allografts. *Clinical Orthopaedics and Related Research* 1987;225:7-16.
- [18] Sachs DH, Bach FH. Immunology of xenograft rejection. *Human immunology* 1990;28:245-51.
- [19] Lin AS, Barrows TH, Cartmell SH, Guldberg RE. Microarchitectural and mechanical characterization of oriented porous polymer scaffolds. *Biomaterials* 2003;24:481-9.
- [20] Murphy CM, Haugh MG, O'Brien FJ. The effect of mean pore size on cell attachment, proliferation and migration in collagen–glycosaminoglycan scaffolds for bone tissue engineering. *Biomaterials* 2010;31:461-6.
- [21] Shalabi M, Gortemaker A, Hof MVt, Jansen J, Creugers N. Implant surface roughness and bone healing: a systematic review. *Journal of dental research* 2006;85:496-500.
- [22] Alla RK, Ginjupalli K, Upadhya N, Shamma M, Ravi RK, Sekhar R. Surface roughness of implants: a review. *Trends in Biomaterials and Artificial Organs* 2011;25:112-8.

- [23] Polini A, Pisignano D, Parodi M, Quarto R, Scaglione S. Osteoinduction of human mesenchymal stem cells by bioactive composite scaffolds without supplemental osteogenic growth factors. *PloS one* 2011;6:e26211.
- [24] Vaccaro AR. The role of the osteoconductive scaffold in synthetic bone graft. *Orthopedics* 2002;25:S571-S8.
- [25] Albrektsson T, Johansson C. Osteoinduction, osteoconduction and osseointegration. *European Spine Journal* 2001;10:S96-S101.
- [26] Kanczler J, Oreffo R. Osteogenesis and angiogenesis: the potential for engineering bone. *Eur Cell Mater* 2008;15:100-14.
- [27] Kellomäki M, Niiranen H, Puumanen K, Ashammakhi N, Waris T, Törmälä P. Bioabsorbable scaffolds for guided bone regeneration and generation. *Biomaterials* 2000;21:2495-505.
- [28] Hulbert SF, Bennett JT. State of the art in dental implants. *Journal of dental research* 1975;54:153-7.
- [29] Tschernitschek H, Borchers L, Geurtsen W. Nonalloyed titanium as a bioinert metal--A review. *Quintessence international* 2005;36.
- [30] Saini M, Singh Y, Arora P, Arora V, Jain K. Implant biomaterials: A comprehensive review. *World Journal of Clinical Cases: WJCC* 2015;3:52.
- [31] Stratton S, Shelke NB, Hoshino K, Rudraiah S, Kumbar SG. Bioactive polymeric scaffolds for tissue engineering. *Bioactive Materials* 2016;1:93-108.
- [32] Cook SD, Thomas KA, Kay JF, Jarcho M. Hydroxyapatite-coated titanium for orthopedic implant applications. *Clinical orthopaedics and related research* 1988;232:225-43.

- [33] Gbureck U, Barralet JE, Radu L, Klinger HG, Thull R. Amorphous α -Tricalcium Phosphate: Preparation and Aqueous Setting Reaction. *Journal of the American Ceramic Society* 2004;87:1126-32.
- [34] Sprio S, Dapporto M, Montesi M, Panseri S, Lattanzi W, Pola E, et al. Novel Osteointegrative Sr-Substituted Apatitic Cements Enriched with Alginate. *Materials* 2016;9:763.
- [35] Klein CP, De Groot K, Drissen A, Van Der Lubbe H. Interaction of biodegradable β -whitlockite ceramics with bone tissue: An in vivo study. *Biomaterials* 1985;6:189-92.
- [36] Gross KA, Berndt CC. 17 Biomedical Application of Apatites. 2002.
- [37] Grynpas M. Age and disease-related changes in the mineral of bone. *Calcified Tissue International* 1993;53:S57-S64.
- [38] Nayak AK. Hydroxyapatite synthesis methodologies: an overview. *International Journal of ChemTech Research* 2010;2:903-7.
- [39] Mobasherpour I, Heshajin MS, Kazemzadeh A, Zakeri M. Synthesis of nanocrystalline hydroxyapatite by using precipitation method. *Journal of Alloys and Compounds* 2007;430:330-3.
- [40] Smičiklas I, Onjia A, Raičević S. Experimental design approach in the synthesis of hydroxyapatite by neutralization method. *Separation and purification technology* 2005;44:97-102.
- [41] Chai C, Ben-Nissan B. Bioactive nanocrystalline sol-gel hydroxyapatite coatings. *Journal of Materials Science: Materials in Medicine* 1999;10:465-9.
- [42] Damien E, Revell P. Coralline hydroxyapatite bone graft substitute: A review of experimental studies and biomedical applications. *Journal of applied biomaterials & biomechanics: JABB* 2003;2:65-73.

- [43] Ruffini A, Sprio S, Tampieri A. Study of the hydrothermal transformation of wood-derived calcium carbonate into 3D hierarchically organized hydroxyapatite. *Chemical engineering journal* 2013;217:150-8.
- [44] Kimura I. Synthesis of hydroxyapatite by interfacial reaction in a multiple emulsion. *Advances in Materials Science and Engineering* 2007;2007.
- [45] Zhang Q, Leng Y, Xin R. A comparative study of electrochemical deposition and biomimetic deposition of calcium phosphate on porous titanium. *Biomaterials* 2005;26:2857-65.
- [46] Jamesh M, Kumar S, Narayanan TS. Electrodeposition of hydroxyapatite coating on magnesium for biomedical applications. *Journal of Coatings Technology and Research* 2012;9:495-502.
- [47] Tampieri A, Celotti GC, Landi E, Sandri M. Magnesium doped hydroxyapatite: synthesis and characterization. *Key Engineering Materials: Trans Tech Publ*; 2004. p. 2051-4.
- [48] Landi E, Tampieri A, Mattioli-Belmonte M, Celotti G, Sandri M, Gigante A, et al. Biomimetic Mg-and Mg, CO 3-substituted hydroxyapatites: synthesis characterization and in vitro behaviour. *Journal of the European Ceramic Society* 2006;26:2593-601.
- [49] Landi E, Tampieri A, Celotti G, Sprio S, Sandri M, Logroscino G. Sr-substituted hydroxyapatites for osteoporotic bone replacement. *Acta Biomaterialia* 2007;3:961-9.
- [50] Cacciotti I, Bianco A, Lombardi M, Montanaro L. Mg-substituted hydroxyapatite nanopowders: synthesis, thermal stability and sintering behaviour. *Journal of the European Ceramic Society* 2009;29:2969-78.
- [51] Miyaji F, Kono Y, Suyama Y. Formation and structure of zinc-substituted calcium hydroxyapatite. *Materials Research Bulletin* 2005;40:209-20.

- [52] Melnikov P, Teixeira A, Malzac A, Coelho MdB. Gallium-containing hydroxyapatite for potential use in orthopedics. *Materials Chemistry and Physics* 2009;117:86-90.
- [53] Li Y, Widodo J, Lim S, Ooi CP. Synthesis and cytocompatibility of manganese (II) and iron (III) substituted hydroxyapatite nanoparticles. *Journal of Materials Science* 2012;47:754-63.
- [54] Tampieri A, D'Alessandro T, Sandri M, Sprio S, Landi E, Bertinetti L, et al. Intrinsic magnetism and hyperthermia in bioactive Fe-doped hydroxyapatite. *Acta biomaterialia* 2012;8:843-51.
- [55] El Feki H, Savariault J, Salah AB. Structure refinements by the Rietveld method of partially substituted hydroxyapatite: $\text{Ca}_{9.5}\text{Na}_{0.5}(\text{PO}_4)_6(\text{CO}_3)_{1.5}(\text{OH})_2$. *Journal of Alloys and Compounds* 1999;287:114-20.
- [56] Rameshbabu N, Sampath Kumar T, Prabhakar T, Sastry V, Murty K, Prasad Rao K. Antibacterial nanosized silver substituted hydroxyapatite: synthesis and characterization. *Journal of Biomedical Materials Research Part A* 2007;80:581-91.
- [57] Shanmugam S, Gopal B. Copper substituted hydroxyapatite and fluorapatite: synthesis, characterization and antimicrobial properties. *Ceramics International* 2014;40:15655-62.
- [58] Gibson IR, Bonfield W. Novel synthesis and characterization of an AB-type carbonate-substituted hydroxyapatite. *Journal of biomedical materials research* 2002;59:697-708.
- [59] Landi E, Celotti G, Logroscino G, Tampieri A. Carbonated hydroxyapatite as bone substitute. *Journal of the European Ceramic Society* 2003;23:2931-7.
- [60] Heling I, Heindel R, Merin B. Calcium-fluorapatite. A new material for bone implants. *The Journal of oral implantology* 1981;9:548.

- [61] Kannan S, Rebelo A, Lemos A, Barba A, Ferreira J. Synthesis and mechanical behaviour of chlorapatite and chlorapatite/ β -TCP composites. *Journal of the European Ceramic Society* 2007;27:2287-94.
- [62] Simon JL, Michna S, Lewis JA, Rekow ED, Thompson VP, Smay JE, et al. In vivo bone response to 3D periodic hydroxyapatite scaffolds assembled by direct ink writing. *Journal of Biomedical Materials Research Part A* 2007;83:747-58.
- [63] Yunos DM, Bretcanu O, Boccaccini AR. Polymer-bioceramic composites for tissue engineering scaffolds. *Journal of Materials Science* 2008;43:4433.
- [64] Bose S, Roy M, Bandyopadhyay A. Recent advances in bone tissue engineering scaffolds. *Trends in biotechnology* 2012;30:546-54.
- [65] Ebaretonbofa E, Evans J. High porosity hydroxyapatite foam scaffolds for bone substitute. *Journal of Porous Materials* 2002;9:257-63.

2. CHARACTERIZATION METHODS

2.1. X-Ray Diffraction (XRD)

X-ray diffraction (XRD) is a non-destructive analytical technique primarily used for phase identification of a crystalline material [1].

Crystals are solids in which the atoms are regularly arranged, that can be described in terms of symmetry elements, reflecting the symmetry of the physical properties of a crystal. The crystal structure of a material is identified by its unit cell and its lattice parameters, the length of the cell edges and the angles between them. Inside the unit cell the atomic position are described by the position on the three spatial axis, x_i , y_i , z_i , measured from a given lattice point. There are different structures with different geometrical entities (points, axes or planes) with a different lattice symmetry that occurs and are defined symmetry elements. The geometrical entities (points, axes or planes) with respect to which a lattice symmetry occurs are defined symmetry elements.

By using the symmetry elements it is possible to define the symmetry operations. Complex symmetry operations lead to space groups, the most detailed level to describe the symmetry properties of the crystal, such as cleavage, electronic band structure and optical properties. Although there are an infinite number of ways to specify a unit cell, for each crystal structure there is a conventional unit cell, which is chosen to display the full symmetry of the crystal.

However, the conventional unit cell is not always the smallest possible choice. The smallest structure completely filled by stacked atoms is called primitive unit cell and each atom has an identical arrangement of the neighboring atoms [2].

The crystal structure consists of the same group of atoms, the basis, positioned around each and every lattice point. This group of atoms therefore repeats indefinitely in three dimensions according to the arrangement of one of the 14 Bravais lattices. **(Figure 2.1.)**

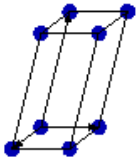
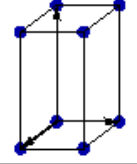
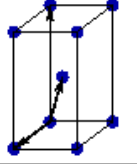
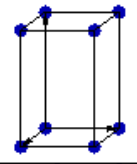
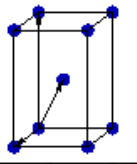
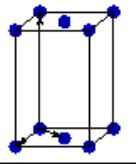
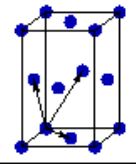
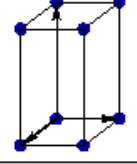
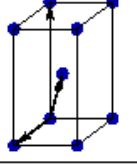
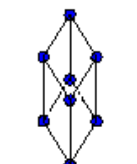
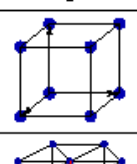
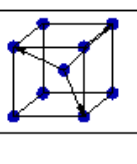
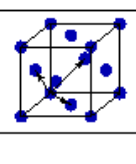
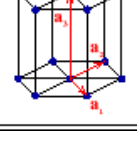
Bravais lattice	Parameters	Simple (P)	Volume centered (I)	Base centered (C)	Face centered (F)
Triclinic	$a_1 \neq a_2 \neq a_3$ $\alpha_{12} \neq \alpha_{23} \neq \alpha_{31}$				
Monoclinic	$a_1 \neq a_2 \neq a_3$ $\alpha_{23} = \alpha_{31} = 90^\circ$ $\alpha_{12} \neq 90^\circ$				
Orthorhombic	$a_1 \neq a_2 \neq a_3$ $\alpha_{12} = \alpha_{23} = \alpha_{31} = 90^\circ$				
Tetragonal	$a_1 = a_2 \neq a_3$ $\alpha_{12} = \alpha_{23} = \alpha_{31} = 90^\circ$				
Trigonal	$a_1 = a_2 = a_3$ $\alpha_{12} = \alpha_{23} = \alpha_{31} < 120^\circ$				
Cubic	$a_1 = a_2 = a_3$ $\alpha_{12} = \alpha_{23} = \alpha_{31} = 90^\circ$				
Hexagonal	$a_1 = a_2 \neq a_3$ $\alpha_{12} = 120^\circ$ $\alpha_{23} = \alpha_{31} = 90^\circ$				

Figure 2.1. the 14 Bravais lattices

The possible lattice centring are:

- P: Simple or Primitive centring, lattice points on the cell corners only;
- I: Body centred, one additional lattice point at the center of the cell;
- F: Face centred, one additional lattice point at centre of each of the faces of the cell;
- C: Centred on a single face, one additional lattice point at the centre of one of the cell faces

An useful notation tools to identify the different planes and directions of a Bravais lattice are the Miller indices. With the Miller indices is possible to identify a reticular plane with three integers h,k,l, reported as (hkl). These indices are vectors reciprocals of the intercepts of the plane on the axes x,y and z.

XRD is based on the constructive interference of monochromatic X-rays, generated by a cathode ray tube, filtered to produce monochromatic radiation with the crystalline material, finely ground to guarantee homogenization of the phase composition. Incident X-ray interacts with the sample, producing constructive interference if the Bragg's law is satisfied. (**Figure 2.2**).

$$n \lambda = 2d \sin \theta$$

where λ is the wavelength of the radiation, d is the distance between the layers of atoms and θ is the angle of incidence. If n is a whole number the radiation will be constructive, otherwise it will be destructive.

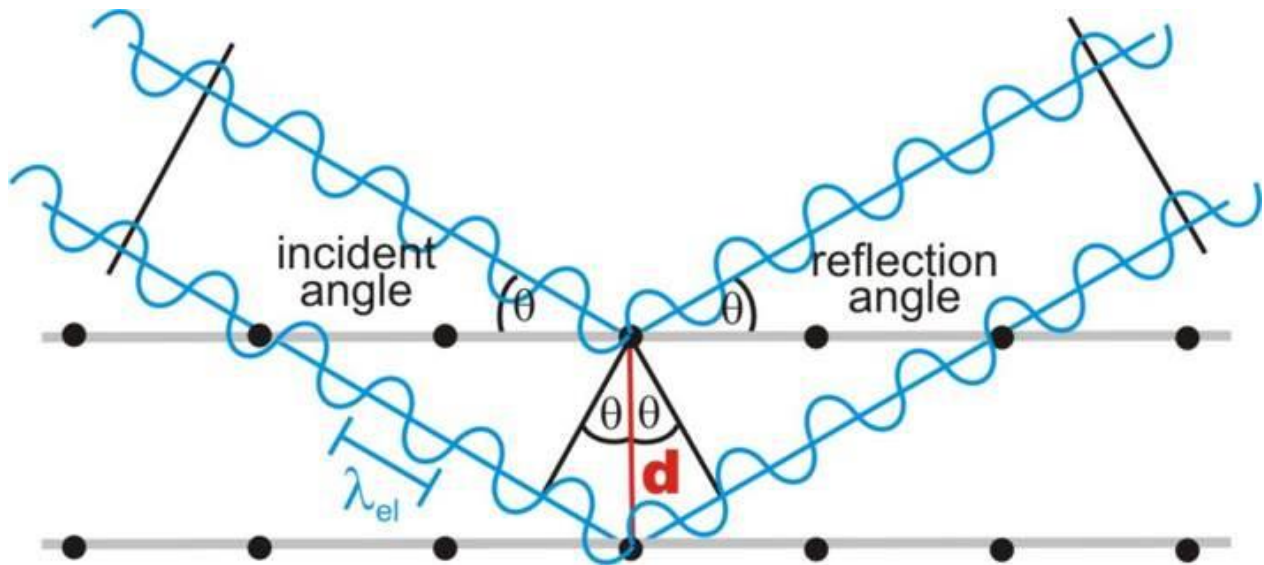


Figure 2.2. – Bragg's law and constructive interference

The interaction of X-rays with atoms leads to the movement of the electronic cloud, with subsequent re-radiation waves with the same frequency, a phenomenon known as elastic scattering or Rayleigh scattering (**Figure 2.3.**).

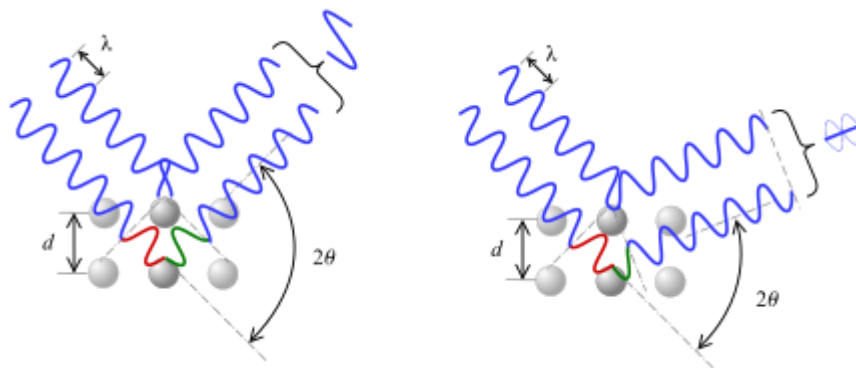


Figure 2.3. – Constructive (left figure) or destructive (right figure) interference in Rayleigh scattering of X-rays.

The results are usually presented in diffractograms, plots that reports peaks as function of the scattering angle 2θ . Peaks appears when a constructive interference occurs between X-rays and the crystalline matrix.

In diffractograms where analyzed position and relative intensity of the peaks, used as fingerprints for the material composition, compared with the the Powder Diffraction Files of the International Centre for Diffraction Data (ICDD). Diffractograms could be refined with Rietveld techniques, providing structural information, such as crystallite dimension, unit cell and axis dimension.

Another useful information in diffractograms is the width of diffraction peak. It is related to several factors, including:

1. instrumental factors
2. the presence of lattice defects
3. strain dishomogeneity among the grains
4. the size of the crystallites

Usually for in a peak is analyzed the full-width at half-maximum (FWHM) that is related with the variation in microstructure and the presence of stress-strain accumulation in the material, that causes an increase of FWHM.

Diffractometer

X-ray diffractometers consist of three basic elements: an X-ray tube, a sample holder, and an X-ray detector. X-rays are generated in a cathode ray tube by heating a filament to produce electrons, accelerating the electrons toward a target by applying a voltage, and bombarding the target material with electrons (**Figure 2.4.**).

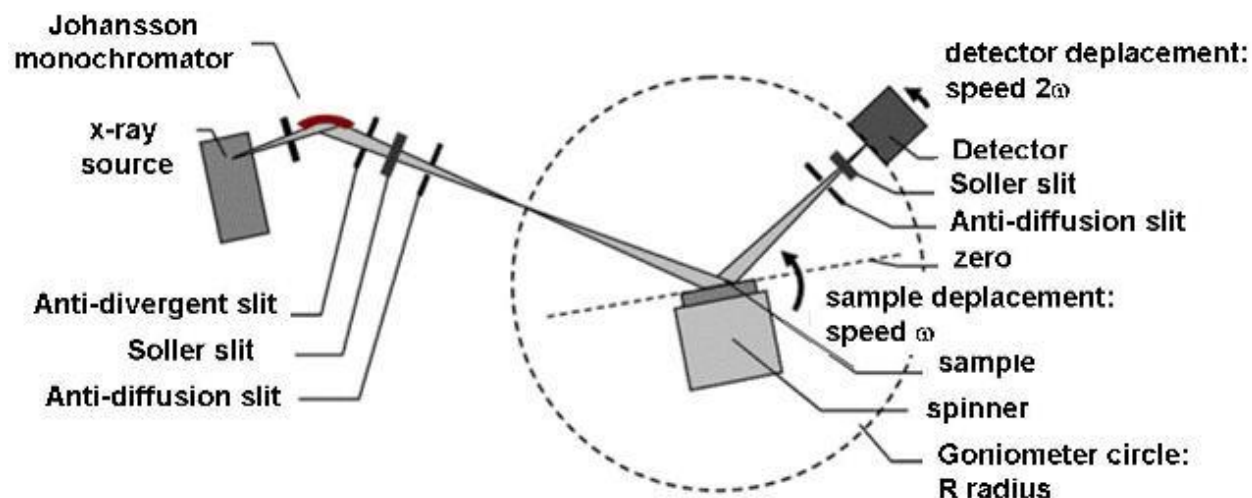


Figure 2.4. – Typical scheme of a Bragg-Brentano type diffractometer

The model of diffractometer employed in this activity is a D8 Advance diffractometer (CuK α radiation) ($\lambda = 1.54178 \text{ \AA}$) generated at 40kV and 40mA equipped with LINXEYE detector (Bruker, Karlsruhe, Germany) working with Bragg-Brentano configuration. XRD spectra were recorded in the 2θ range from 20 to $60^\circ 2\theta$ with a counting time of 0.5s and a step size of 0.02° . The lattice parameters refinement was performed according to the Rietveld method (TOPAS 4.2 software).

Full profile analysis

The full profile analysis or Rietveld refinement is a technique devised by Hugo Rietveld for use in the characterization of crystalline materials. The height, width and position of the reflection peaks is used to determine many aspects of the material's structure.

The Rietveld method, first implemented in 1967 and reported in 1969 [3], uses a least squares approach to refine a theoretical line profile until it matches the measured profile. The introduction of this technique was a significant step forward in the diffraction analysis of powder samples as, unlike other techniques at that time, it was able to deal reliably with strongly overlapping reflections. The principle of the Rietveld Method is to minimize a function M which analyzes the

difference between a calculated profile $y(\text{calc})$ and the observed data $y(\text{obs})$. Rietveld defined such an equation as:

$$M = \sum_i W_i \left\{ y_i^{\text{obs}} - \frac{1}{c} y_i^{\text{calc}} \right\}^2$$

where W_i is the statistical weight and c is a scale factor such that $y^{\text{calc}} = y^{\text{obs}}$.

With this technique is possible to obtain further information about different parameter of the analyzed phase (i.e. the lattice parameter, domain dimensions, atomic substitution, anisotropy).

In this work the full profile refinement was carried out by aid of TOPAS 5.

2.2. Inductively Coupled Plasma Optical Emission Spectroscopy (ICP-OES)

The inductively coupled plasma optical emission spectroscopy (ICP-OES) is the most popular and precise analytical technique for the determination of the elemental composition and for the determination of trace elements [4] (Figure 2.5).

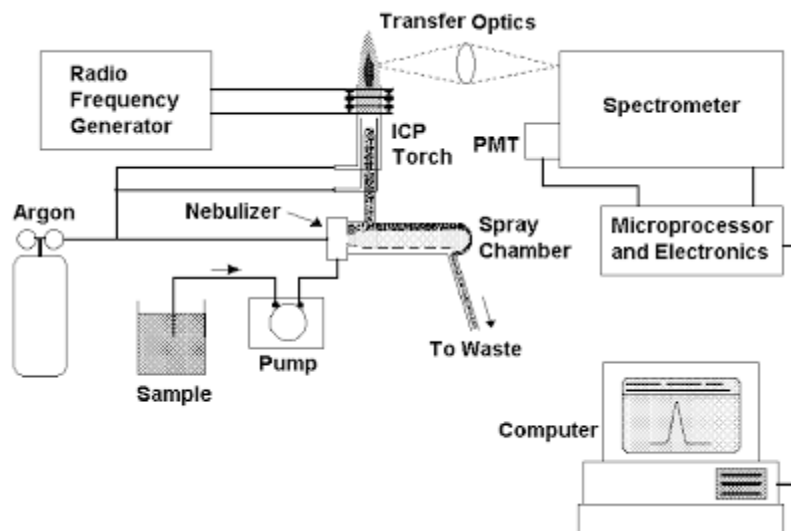


Figure 2.5. Schematic representation of an ICP-OES instrument

The technique is based upon the spontaneous emission of photons from atoms and ions that have been excited by a radiofrequency (RF) discharge. Atoms and ions were analyzed in plasma. Plasma can simply be considered as a gaseous mixture of negatively charged electrons and highly charged positive ions, being created by heating a gas or by subjecting gas to a strong electromagnetic field. In this case an inductively coupled plasma is created in a torch, that consists of three concentric tubes, usually made of quartz. The end of this torch is placed inside an induction coil supplied with a radio-frequency electric current. A flow of argon gas is introduced between the two outermost tubes of the torch and an electrical spark is applied for a short time to introduce free electrons into the gas stream. The sample, that has to be in liquid phase, is converted to an aerosol and conveyed into the central channel of the plasma. The maximum temperature that can be reached by the inductively coupled plasma (ICP) is 10000K, so that the aerosol is quickly vaporized. Analyte elements are liberated as free atoms in the gaseous state. Further collisional excitation within the plasma imparts additional energy to the atoms, promoting them to excited states. Sufficient energy is often available to convert the atoms to ions and subsequently promote the ions to excited states. Both the atomic and ionic excited species may then relax to the ground state via the emission of photons. The wavelength of the emitted photons is characteristic of the quantized energy level structure of the atoms and can be used to identify the elements from which they were originated [5]. In addition the total number of photons is directly proportional to the concentration of the originating element in the sample and could be correlated using a previous calibration obtained with opportune standard solutions.

2.3. Fourier Transform Infrared Spectroscopy (FTIR)

Infrared spectroscopy (IR spectroscopy) is the subset of spectroscopy that deals with the infrared region of the electromagnetic spectrum. The term is originated because a Fourier transform (a mathematical process) is required to convert the raw data into the actual spectrum. As with all spectroscopic techniques, it can be used to identify and study chemicals. The infrared portion of the electromagnetic spectrum is usually divided into three regions; the near-, mid- and far-infrared, named for their relation to the visible spectrum. The higher-energy near-IR, approximately $14000\text{--}4000\text{ cm}^{-1}$ ($0.8\text{--}2.5\text{ }\mu\text{m}$ wavelength) can excite overtone or harmonic vibrations. The mid-infrared, approximately $4000\text{--}400\text{ cm}^{-1}$ ($2.5\text{--}25\text{ }\mu\text{m}$) may be used to study the fundamental vibrations and associated rotational-vibrational structure. The far-infrared, approximately $400\text{--}10\text{ cm}^{-1}$ ($25\text{--}1000\text{ }\mu\text{m}$), lying adjacent to the microwave region, has low energy and may be used for rotational spectroscopy. The names and classifications of these subregions are conventions, and are only loosely based on the relative molecular or electromagnetic properties [6].

Infrared spectroscopy exploits the fact that molecules absorb frequencies that are characteristic of their structure. These absorptions are resonant frequencies, i.e. the frequency of the absorbed radiation matches the vibrational frequency. The energies are affected by the shape of the molecular potential energy surfaces, the masses of the atoms, and the associated vibronic coupling. **(Figure 2.6.)**

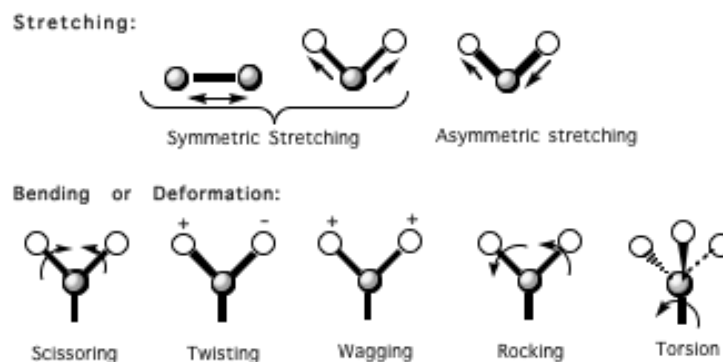


Figure 2.6. Overview of the movements correlated to infrared spectroscopy

The infrared spectrum of a sample is recorded by passing a beam of infrared light through the sample. When the frequency of the IR is the same as the vibrational frequency of a bond or collection of bonds, absorption occurs. Examination of the transmitted light reveals how much energy was absorbed at each frequency (or wavelength). This measurement can be achieved by scanning the wavelength range using a monochromator. Alternatively, the entire wavelength range is measured using a Fourier transform instrument and then a transmittance or absorbance spectrum is generated using a dedicated procedure.

This technique is commonly used for analyzing samples with covalent bonds. Simple spectra are obtained from samples with few IR active bonds and high levels of purity. More complex molecular structures lead to more absorption bands and more complex spectra.

For solid materials, like the ones analyzed in this work, a quantity of sample is grinded finely with potassium bromide (to remove scattering effects from large crystals). The mixed powder is then crushed in a mechanical die press to form a translucent pellet through which the beam of the spectrometer can pass. A reference is necessary to avoid fluctuation in the output of the source, affecting data, and to cancel the effects of the presence of KBr. A pure KBr pellet is used as reference.

2.4. Scanning Electron Microscopy (SEM) and Energy-Dispersive X-ray spectroscopy (EDX)

A scanning electron microscope (SEM) is a type of electron microscope that produces high magnification images of a sample (up to 200000x), with both resolution and field depth higher than the conventional optical microscope, by scanning it with a focused beam of electrons. The electrons interact with atoms in the sample and, after focusing the high-energy beam of electrons onto the surface of a sample, produces various signals that contain information about the sample's surface topography and composition [7] (**Figure 2.7**).

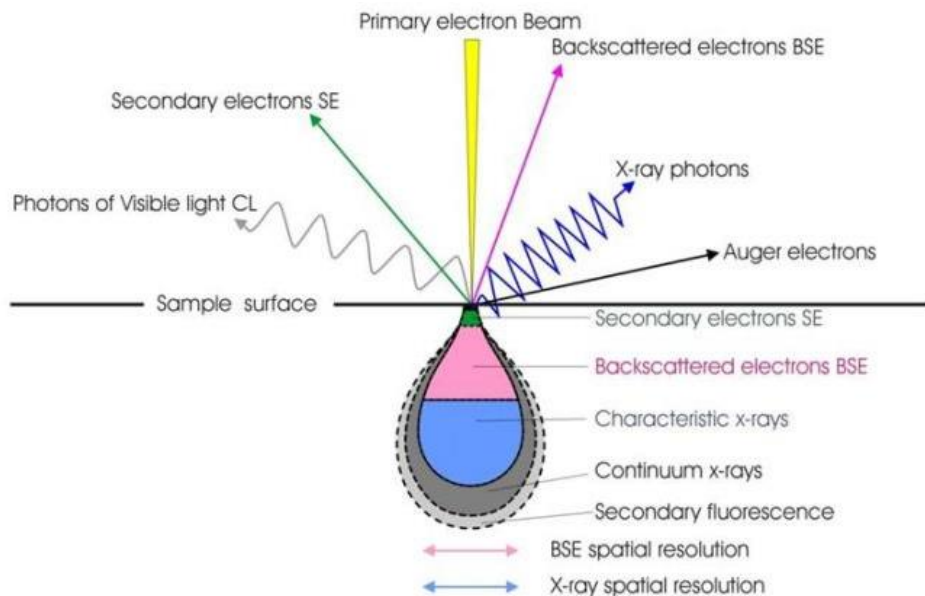


Figure 2.7. Interaction of electrons with the surface

The primary electrons which are not reflected transfer their energy to some of the electrons of the samples, making them able to diffuse towards the surface and escape outside of the sample with a low energy (energy < 50 eV), the so-called secondary electrons. Furthermore, characteristic x-ray photons are emitted when the primary beam causes the ejection of inner shell electrons from the sample and are used to investigate the elemental composition of the sample. The back-

scattered electrons emitted from the sample may be used alone to form an image or in conjunction with the characteristic x-rays as atomic number contrast clues to the elemental composition of the sample.

In a typical SEM, an electron beam is thermionically emitted from an electron gun fitted with a tungsten filament cathode. Tungsten is normally used in thermionic electron guns because it has the highest melting point and lowest vapor pressure of all metals, thereby allowing it to be electrically heated for electron emission, and because of its low cost. The electron beam, which typically has an energy ranging from 0.2 keV to 40 keV, is focused by one or two condenser lenses to a spot about 0.4 nm to 5 nm in diameter. The beam passes through pairs of scanning coils or pairs of deflector plates in the electron column, typically in the final lens, which deflect the beam in the x and y axes so that it scans in a raster fashion over a rectangular area of the sample surface. The interaction volume depends on the electron beam energy, the atomic number of the specimen and the specimen's density. The secondary electrons, due to their low energy, are detected by a scintillator-photomultiplier device and the resulting signal is rendered into a two-dimensional intensity distribution that can be viewed and saved as a digital image. The brightness of the signal depends on the number of secondary electrons reaching the detector. The spatial resolution of the SEM depends on the size of the electron spot, which in turn depends on both the wavelength of the electrons and the magnetic electrooptical system which produces the scanning beam.

The equipment employed in the present work is a FEI, Quanta 200, USA.

Energy Dispersive X-ray spectroscopy

The Energy-Dispersive X-ray spectroscopy (EDX) is an analytical technique used for the elemental analysis or chemical characterization of a sample during SEM analysis. It utilizes x-ray fluorescence to characterize the elements present in a material [8]. If a sample is excited under high energy of electron beam or other electromagnetic radiation, the inner shell of electrons is ejected to vacuum creating a vacancy in that shell (**Figure 2.8.**).

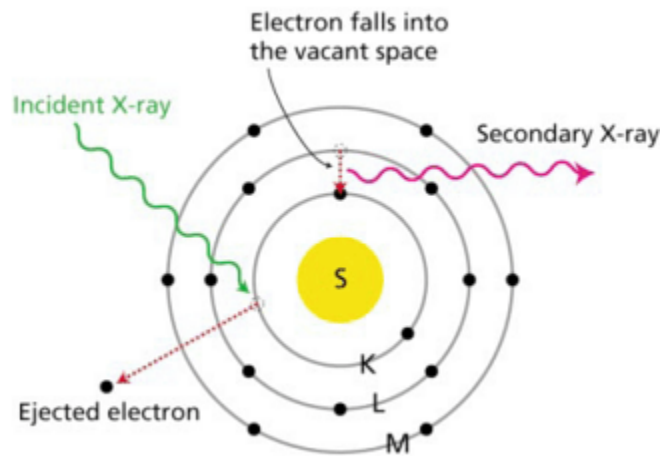


Figure 2.8. Representation of the creation of secondary x-ray

Electrons from the outer shell fall into the vacant site for filling the inner shell. During this process (radiant energy), the sample fluoresces X-ray of energy equal to the energy difference between the starting and final state. Because each atom has its unique and discretized energy levels, the X-ray fluorescence is also characteristic of every atom.

SiLi detectors operating at liquid nitrogen temperature are commonly used in EDX experiments: striking the detector, the X-rays produce photoelectrons which in turn produces electron-hole pairs within the Si. These migrate to opposite ends of the detectors (via an applied electric field of 1.5 kV) producing a current pulse whose size is proportional to the energy of the incident X-Ray.

2.5. Specific Surface Area (SSA-BET)

Of enormous importance in the materials chemistry, particularly in ceramic processing, is reserved to size, shape and specific surface area (SSA) of the powders. For the calculation of specific surface area is assumed that a powder is composed by small spherical particles with the same diameter. The specific surface area (m^2/g) of the powder, S , can be calculated by multiplying the surface area of each particle and n , the number of the particles per weight unit ($S = 4\pi r^2 n$).

Indeed, the size and shape of the powder particles are usually irregular and unexpected, so that it is not possible to define a simple model of the surface area. In this case, the SSA is indirectly measured by the adsorption of a gas on the outer surface of the particles.

When a gas is adsorbed on the surface of a material, two different adsorption processes can occur: a physical and a chemical adsorption. The main difference relates to the interactions forces involved in the adsorption of the gas: the first one is characterized by weak Van der Waals and electrostatic forces, while the latter includes also stronger chemical bonds. For that reason, a physical adsorption is considered the easier way to determine SSA, with the quantification of the reversible process (desorption) can be adopted to quantify the adsorbed gas.

B.E.T. Equation

The scientists Stephen Brunauer, Paul Hugh Emmett and Edward Teller published in 1938 [9] a theory to describe the multilayer adsorption phenomena as an extension of the Langmuir theory [10].

Three main postulates were proposed:

- 1) gas molecules physically adsorb on a solid in layers infinitely
- 2) there is no interaction between each adsorption layer

3) the Langmuir theory can be applied to each layer

The resulting BET equation, simplified by the use of the parameters of a single gas, is:

$$\frac{p}{V_{ads}(p^0 - p)} = \alpha \frac{p}{p^0} + \beta$$
$$\alpha = \frac{C - 1}{V_m C} \quad \beta = \frac{1}{V_m C}$$

where V_{ads} is the adsorbed gas quantity, V_m is the monolayer adsorbed gas quantity, p is the equilibrium pressure of the adsorbates at the temperature of adsorption, p^0 is the saturation pressure of the adsorbates at the temperature of adsorption and C is the BET constant, related to the net adsorption energy.

This equation can be parameterized, resulting in the equation of a line, $y=\alpha x+\beta$, especially in a low pressure range 0.05-0.30. Once derived the α and β coefficients, V_m is determined as $1/(\alpha+\beta)$.

The total surface area of the adsorbed gas, S , is determined by multiplying V_m and S_0 , the area correspondent to 1 cm^3 of an adsorbed gas monolayer ($S = V_m S_0$).

Finally, SSA is determined by dividing S and W , the sample weight.

Returning to the assumption that all the particles were spherical and equal, the specific surface area measurement can also be used to evaluate the size of the particles according to the formula:

$$S = \frac{6}{d * l}$$

where S is the specific surface area, d is the density of the material and l is the dimension of the particle.

To perform an SSA-BET analysis the sample holder is immersed in liquid nitrogen to enable the adsorption process. After few minutes, the gas stabilization occurs and the adsorption process is quantified. Then, the desorption process is forced by substituting the liquid nitrogen with a room

temperature water bath; in this condition, the previously adsorbed nitrogen is released. Ideally, the gas adsorption is completely reversible and the desorption is equivalent to the adsorption.

In this activity, the Micrometrics FlowSorb II 2300 instrument was used.

2.6. Porosity

Mercury intrusion porosimetry

In the creation of 3D object, a property of great interest to control is the porosity, that affect physical properties of the materials. The term porosimetry refers to an analytical technique used to measure the distribution of pore in function of their dimension.

Mercury intrusion porosimetry is based on the premise that a nonwetting liquid (contact angle $> 90^\circ$), in this case Hg, will intrude capillaries only under pressure (**Figure 2.9**).

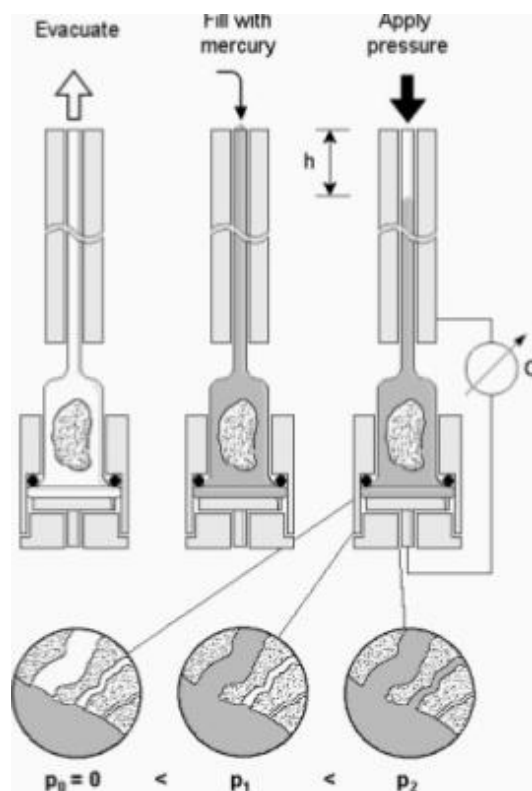


Figure 2.9. – Schematic view of a mercury porosimeter

The relationship between the pressure and capillary diameter was described by Washburn [11] as:

$$P = \frac{-4\gamma\cos\theta}{d}$$

where P is the pressure, γ is the surface tension of the liquid, θ is the contact angle of the liquid and d is the diameter of the capillary.

The pressure required for the infiltration of Hg is inversely proportional to the size of the pores, so that a low pressure is required to intrude mercury into large macropores, whereas a greater pressure is required to force mercury into small pores.

The pore size distribution is determined from the volume intruded at each pressure increment, while the total porosity is determined from the total volume intruded.

In this work, the pore volume and pore size distributions were evaluated by mercury intrusion porosimetry (surface tension = 0.48 N/m and contact angle = 140°, Hg pressure in the range 0-200 Pa, Thermo Scientific Surfer). The measurement error is related to the accuracy of Hg intrusion porosimetry (<4%).

Total porosity

The total porosity of a 3D object can also be calculated by comparing its density with the theoretical density of the material following the equation:

$$P = 1 - (d_p/d_t) \%$$

where P is the total porosity as percentage, d_p is the density of the piece and d_t is the theoretical density of the material.

2.7. Thermo-Gravimetric analysis (TGA)

The Thermogravimetric analysis is a useful test to determine changes in weight in relation to change in temperature. Such analysis relies on a high degree of precision in three measurements:

weight, temperature, and temperature change [12]. As many weight loss curves look similar, the weight loss curve may require transformation before results may be interpreted. A derivative weight loss curve can be used to tell the point at which weight loss is most apparent.

The analyzer usually consists of a high-precision balance with a pan loaded with the sample. The sample is placed in a small electrically heated oven with a thermocouple to accurately measure the temperature. The atmosphere may be purged with an inert gas to prevent oxidation or other undesired reactions. A computer is used to control the instrument. Analysis is carried out by raising the temperature gradually and plotting weight against temperature. After the data is obtained, curve smoothing and other operations may be done such as to find the exact points of inflection.

In this activity, the Simultaneous Thermal Analyser (STA 449 Jupiter Netzsch Geratebau, Selb, Germany) was used.

2.8. Mechanical characterization

The strength of ceramics materials is mainly characterized by compressive tests, because of the intrinsic micron-size defects that can be easily extended during a tensile stress, affecting the measurement. For that reason, the compressive strength of ceramics is generally higher than their tensile strength. A compressive test of a specimen involves a system of converging forces which tends to reduce its size

The uniaxial compression tests provide a simple and effective way to characterize a material's response to loading. By subjecting a sample to a controlled compressive displacement along a single axis, the change in dimensions and resulting load can be recorded to calculate a

stress/strain profile. From the obtained curve, elastic and plastic material properties can then be determined.

The compressive strength of scaffolds is an important bio-engineering consideration. When using porous structures for tissue engineering scaffolds, the structure must retain sufficient mechanical properties to fulfil the requirements of structural integrity once implanted in host tissue.

In uniaxial compression the forces are directed along one direction only, so that they act towards decreasing the object's length along that direction.

The tests were performed in displacement control at 0.5 mm/min, by collecting data at 20 Hz with a universal testing machine (MTS Insight 5, Minnesota, USA).

2.9. References

- [1] B.D. Cullity Elements of X-ray Diffraction Addison Wesley Mass. 1978 ISBN 0-201-01174-3
- [2] Hahn, Theo, ed. (2002). International Tables for Crystallography, Volume A: Space Group Symmetry. A (5th ed.). Berlin, New York: Springer-Verlag. ISBN 978-0-7923-6590-7.
- [3] H M Rietveld, J. Appl. Cryst. 2, 65–71 (1969)
- [4] Hou X, Jones BT. Inductively Coupled Plasma/Optical Emission Spectrometry. Encyclopedia of Analytical Chemistry: John Wiley & Sons, Ltd; 2006.
- [5] Baggioni L., Beltrani N., Graziani D. and M., Masironi M., Montanari M., Piazza L., Rondini G, Tondini D., Visani A.; About friendship; Scientific high school; September 2003.
- [6] Griffiths, P.; de Haseth, J.A. (18 May 2007). Fourier Transform Infrared Spectrometry (2nd ed.). Wiley-Blackwell. ISBN 0-471-19404-2
- [7] McMullan, D. (2006). "Scanning electron microscopy 1928–1965". Scanning. 17 (3): 175–185.
- [8] Joseph Goldstein (2003). Scanning Electron Microscopy and X-Ray Microanalysis. Springer. ISBN 978-0-306-47292-3. Retrieved 26 May 2012
- [9] Brunauer S, Emmett PH, Teller E. Adsorption of Gases in Multimolecular Layers. Journal of the American Chemical Society. 1938;60:309-19.
- [10] Langmuir I. The adsorption of gases on plane surfaces of glass, mica and platinum. Journal of the American Chemical Society. 1918;40:1361-403

[11] Washburn EW. Note on a Method of Determining the Distribution of Pore Sizes in a Porous Material. Proc Natl Acad Sci U S A. 1921;7:115-6.

[12] Coats, A. W.; Redfern, J. P. (1963). "Thermogravimetric Analysis: A Review". Analyst. 88 (1053): 906–924.

3. SYNTHESIS OF MULTISUBSTITUTED APATITIC PHASES WITH ANTIBACTERIAL ACTIVITY

The establishment of more effective and durable therapies for restoring extensive bone parts is an urging need. Bone regeneration requires the use of biomaterials with chemico-physical features enabling cell instruction to assist the regenerative cascade. The importance of using biomaterials with bone-mimicking chemical features is a major need to prevent adverse reactions and to adequately trigger the regenerative cascade. [1] [2] Besides, the occurrence of post-surgical complications such as infections is a serious concern: bacterial contamination provokes the formation of biofilm at the bone-implant interface that hampers new bone formation and osteointegration, thus leading to the implant failure and additional surgery that provoke significant morbidity for the patient and a raise of the healthcare costs. This drawback is particularly frequent in the case of metallic prostheses used for hip and knee replacement, with more than 300,000 implants performed each year only in the US and an incidence of infections around 0.5% to 4% in total hip and knee arthroplasties, respectively [3]. To prevent implant infection, systemic administration of antibiotics like cephalosporins is a common pre-surgery practice. However, systemic approaches require large dosage that may provoke adverse secondary effects and are often accompanied by limited therapeutic effectiveness. [4] Advanced

approaches have been pursued to incorporate drugs into the bone cement used for prosthesis fixation, or into the implant coating. However, these approaches also suffer of limited effectiveness, due to the existence of antibiotic-resistant bacteria and also to the decrease of the antibiotic activity during the storage and/or sterilization process [5].

Therefore new solutions integrating a significant boosting and assistance to bone regeneration with prolonged and effective protection against bacteria are today highly desired. In this respect, hydroxyapatite (HA: $\text{Ca}_{10}(\text{PO}_4)_6(\text{OH})_2$) is an elective material for bone regeneration, as it closely resembles the bone mineral and demonstrated excellent biocompatibility and ability to establish tight interface with newly formed bone [6] [7]. The synthesis of multi-substituted HA nanophases has been successfully carried out in previous studies, to improve biomimicry of HA and increase its bioactivity [8] [9]. Bio-competent ion substitutions in the HA lattice can be obtained during synthesis by neutralization method, where the conditions of temperature, pH and ionic strength are adjusted to enable the entering of ions addressed to occupy the same crystal site (e.g. the two independent sites of calcium or the phosphate site) [10]. The nature and amount of such ions have specific effects on the bone regenerative cascade [11].

The HA lattice is able to host several foreign ions that can be exposed in high density or released, particularly when the HA phase is obtained by wet methods that provide nanosize and high specific surface [12]; therefore HA nanophases have the potential of multi-purpose materials with functionality that can be in principle tailored on the basis of the type and amount of ion substitutions. such as antibacterial effects [13]. Recent studies suggest that the doping with ions [14] like Ag^+ [15], Ga^{3+} [16] and Zn^{2+} [13], already known for their antibacterial activity, in the hydroxyapatite lattice could provide a long term antibacterial effect through the progressive release of secondary ions in the biological fluids or through exposure on the HA surface. Indeed,

it was shown that HA nanophases can progressively release calcium and foreign ions by ion exchange phenomena mediated by the hydrated surface layer typical of HA nanophases. Ions with reputed antibacterial effects have different inhibition mechanisms. Ag^+ ions can penetrate the bacterial cell wall, subsequently turning DNA into a condensed form as a reaction of DNA against the denaturation effect of Ag ions. At the same time, Ag ions react with proteins by combining -SH groups, leading to the inactivation of bacterial proteins. As a result, DNA of bacteria loses their replication ability, and bacterial proteins become inactivated, which leads to the damage and even the death of microorganisms [17]. The introduction of Ag ions in the HA lattice was attempted in previous studies but resulted tricky. In fact its high affinity with phosphate groups favors a rapid precipitation of silver phosphates thus preventing its incorporation into the HA lattice. Zn^{2+} ions are commonly found in natural bones in a ratio Zn/Ca about 0,1%. Zinc has ability to stimulate bone regeneration, since it inhibits osteoclasts activity, which cause bone resorption, whereas stimulating the proliferation of osteoblasts [18] [19]. A secondary effect of zinc regards its antibacterial activity, especially against *Staphylococcus aureus*, a bacteria commonly found in post-surgical infections and a possible initiator of osteomyelitis. Due to this additional functionality, the incorporation of Zn^{2+} ions in the HA lattice raised considerable interest and it was subject of several studies in the past years [18] In contrast, few studies have been performed so far on the antibacterial effect of gallium. Systemic administration of gallium results effective against many bacterial strains as it replaces iron in many enzymes fundamental to the growth and proliferation of bacteria thus interfering with their metabolism. However, gallium does not exhibit toxic effects in respect to possible interaction with hemoglobin because this protein uses Fe in its oxidation state of 2+ while Ga exists only in the 3+ oxidation state [16] [20].

In the present work, new hydroxyapatite nanophases presenting multiple ion substitutions were synthesized with the purpose to confer both enhanced osteogenic ability and antibacterial effect. More specifically, the wet synthesis of low-crystallinity hydroxyapatite was carried out in the presence of magnesium and carbonate ions, as well as of zinc or gallium to obtain a (Mg, CO₃, Zn/Ga)-substituted hydroxyapatite. The effective doping of the HA lattice by antibacterial ions, in the presence of Mg and CO₃²⁻, was thoroughly investigated and selected materials were tested in relevant environment to assess the cytotoxicity and osteogenic potential in the presence of human mesenchymal stem cells, as well the specific antibacterial ability of zinc and gallium. The new materials were tested with several bacterial strains, *Staphylococcus Aureus*, *Candida Albicans*, *Escherichia Coli*, *Pseudomonas Aeruginosa*, belonging to different strains of contaminant agents (gram positive, gram negative, yeast). Those strains were selected among the most common ones involved in infective processes, especially post-operative infections, [21] and evaluated in respect to the kinetics of ion release to associate the antibacterial activity to the presence or exposure of doping ions.

3.1. Materials and methods

Raw materials

Common high-purity chemical reagents were purchased from Sigma Aldrich. Ultrapure water (0.22 mS, 25 °C) was used in all the experiments.

Material characterization

The phase composition of the product was obtained by X-ray diffraction (XRD), by using a D8 Advance Diffractometer (Bruker, Karlsruhe, Germany) equipped with a Lynx-eye position sensitive device using Cu K α radiation ($\lambda = 1.54178 \text{ \AA}$) generated at 40kV and 40mA. XRD

spectra were recorded in the 2θ range from 20 to $60^\circ 2\theta$ with a counting time of 0.5 s and a step size of 0.02° . Full profile analysis of the XRD spectra to assess cell parameters and crystallite size was carried out by aid of TOPAS 5 (Bruker, Karlsruhe, Germany).

Infrared spectroscopy was performed on the as-obtained powders, by using a Nicolet 380 FTIR spectrometer (Thermo Fisher Scientific Inc., Waltham, MA, US). The FTIR spectra were recorded in the wavelength range from 4000 to 400 cm^{-1} on small pellets obtained by mixing 1 mg of the sample powder with 150 mg of anhydrous potassium bromide (KBr). The mixture was pressed at 10 t pressure into 7 mm diameter disks. Before the acquisition of the FTIR spectra, the disks were heated at 100°C for a period of 24 h to expel the physically adsorbed water. A pure KBr disk was used as blank.

The evaluation of the carbonate content was made by thermo-gravimetric analysis (TGA) of dried samples, using a Stanton STA 1500 (Stanton, London, UK). About 10 mg of the sample was weighed in an alumina crucible and heated from room temperature to 1100°C under nitrogen flow. The heating rate was $10^\circ\text{C}/\text{min}$. An empty alumina crucible was used as reference standard. The carbonate content was evaluated on the basis of the weight loss detected between 600°C and 1100°C . [22].

The chemical analysis was performed on dried samples using ICP-OES spectrometer (Agilent 5100). About 20 mg of hydroxyapatite was weighed and dissolved into 2 ml of nitric acid (Sigma Aldrich 65 vol%) then diluted in 100 ml of milliQ water. The solution was then analyzed using standard prepared from primary standards (1000 ppm, Fluka). The elements were analyzed with the following spectral line: Ca 422.673 , Ga 294.363 , Mg 279.553 , Zn 213.857 and P 213.618 .

Ion release

The evaluation of the ion release with time was made by immersing tablets (1 g of powder each) into 5 ml of pH=7.4 buffer solution (Ca and Mg free Hank's Balanced Salt solution) and maintained at 37°C under gentle shaking. At scheduled times (i.e. after 1, 2, 3, 7, 11 and 15 days) the solution was removed and 5ml of fresh solution was added to the tablets. The liquids containing the ions released after the prefixed times were analyzed by ICP-OES for the quantitative determination of Ca, Mg, Zn and Ga. The results were presented as cumulative data. All the experiments were made in triplicate.

Cell culture

Human Adipose-Derived Mesenchymal Stem Cells (ASCs) were purchased from ATCC and cultured in Modified Eagle's Medium (α MEM GlutaMAX, Gibco, Thermo Fisher Scientific) supplemented with 15% Fetal Bovine Serum (FBS, Gibco), 10 ng/ml Fibroblast Growth Factor (FGF, Invitrogen) and 1% penicillin/streptomycin (100 U ml⁻¹/100 μ g ml⁻¹) and incubated at 37 °C with 5% CO₂. The cells were cultured until 70-80% of confluence, then detached by trypsinization, centrifuged and suspended again. Cell number and viability were assessed with the trypan-blue dye exclusion test.

For the experiments, ASCs were plated in 6, 24 and 96 well-plates at 5.0 x 10³ cells/cm² and cultured in osteogenic medium (α MEM supplemented with 10% FBS, 1% penicillin/streptomycin 100 U/ml/100 μ g/ml, 10 mM β -glycerophosphate, 50 μ g/ml ascorbic acid and 100 nM dexamethasone).

24 h after the cell seeding two different concentrations (50 μ g/ml and 500 μ g/ml) of nanoparticles (GaHA; GaMgCO₃HA and HA) were added to the cells and left in culture for the entire duration of the study.

Cell Viability Assay

The MTT reagent (3-(4,5-dimethylthiazol-2-yl)-2,5-diphenyltetrazolium bromide) was prepared at 5 mg/ml in 1x PBS. Cells seeded in 96-well plates, were incubated with the MTT reagent 1:10 for 2 h at 37 °C. Medium was collected and cells were incubated with 200 µl of dimethyl sulfoxide for 15 min. In this assay, the metabolically active cells react with the tetrazolium salt in the MTT reagent to produce a formazan dye that can be observed at λ_{max} of 570 nm, using a Multiskan FC Microplate Photometer (Thermo Fisher Scientific). This absorbance is directly proportional to the number of metabolically active cells. Mean values of absorbance were determined. Three samples per group were analysed at day 1, 3, 7 and 14.

Cell morphology evaluation

After 3 days of culture, cell cultures were washed in 1x PBS for 5 min and fixed in 4% (w/v) paraformaldehyde for 15 min. Permeabilization was performed with 1x PBS with 0.1% (v/v) Triton X-100 for 5 min. FITC conjugated phalloidin (Invitrogen) 38 nM in 1x PBS was added for 20 min at room temperature in the dark. For nuclear staining the cells were incubated with DAPI 300 nM (Invitrogen) for 5 min. Images were acquired by an Inverted Ti-E fluorescence microscope (Nikon). The analysis was performed for all the groups at both concentrations, but only one representative image for each group has been reported.

Quantitative Real-Time Polymerase Chain Reaction (qPCR)

After 7 and 14 days, cells grown in 6 well-plates in presence of the two concentrations of GaHA, GaMgHA and HA were lysed and total RNA extraction was performed by use of the Tri Reagent, followed by the Direct-zol™ RNA MiniPrep kit (Zymo Research) according to manufacturer's instructions. RNA integrity was analysed by native agarose gel electrophoresis and quantification performed by the Qubit® 2.0 Fluorometer together with the Qubit® RNA BR assay kit,

following manufacturer's instructions (Invitrogen). Total RNA (500 ng) was reverse transcribed to cDNA using the High-Capacity cDNA Reverse Transcription Kit, according to manufacturer's instructions (Life Technologies). Quantification of the expression of gene alkaline phosphatase (ALPL, HS01029144) was performed by use of the StepOne™ Real-Time PCR System (Applied Biosystems). The housekeeping gene used was glyceraldehyde 3-phosphate dehydrogenase (GAPDH, HS99999905) (Life Technologies). Experiment was done in triplicate, using three technical replicates for each experiment. Data were collected using the StepOne Software (v.2.2.2) and relative quantification was performed using the comparative threshold (Ct) method ($\Delta\Delta Ct$), where relative gene expression level equals $2^{-\Delta\Delta Ct}$ [29]. HA samples were used as calibrator.

Immunofluorescence analysis

Osteogenic cell differentiation was also analyzed by immunofluorescence through the staining of runt-related transcription factor 2 (RUNX2) and Collagen I (COL-I). After 7 days of cell culture, cells seeded on 24 well-plate were fixed in 4% (w/v) paraformaldehyde. Blocking was performed with 20% normal goat serum and cell permeabilization with 0.1% (v/v) Triton x-100. Cells were incubated overnight at 4°C, with antibodies anti-RUNX2 and anti-COL-1 (Abcam). Primary antibodies were probed with the secondary antibodies Alexa Fluor 488 goat anti-rabbit (Molecular Probes) and Cy3 sheep anti-mouse (Molecular Probes), for 45 minutes at room temperature. Cell nuclei were stained with DAPI 300 nM. Images of one sample per group were acquired by an Inverted Ti-E fluorescence microscope (Nikon).

Statistical analysis

Results were expressed as mean \pm standard error of the mean (SEM) plotted on graph. Analysis of the effect of the nanopowders on cell viability and gene expression was made by two-way

analysis of variance (ANOVA), followed by Bonferroni's post hoc test. Statistical analyses were performed by the GraphPad Prism software (version 6.0) with statistical significance set at $p \leq 0.05$.

Antibacterial tests

In order to prepare the working culture of microbial strains, subculture from the stock culture by streaking onto Tryptone Soy Agar (TSA) (for bacteria) and onto Sabouraud Destrose Agar (SDA) (for Candida) was prepared and incubate overnight. A second subculture was made and incubated as earlier. The second subculture was the working culture.

From the working culture a loop full of bacterial cells was transferred into the diluent and suspended. Each microbial test suspension was prepared by taking 1 ml of diluent (Tryptone Sodium Chloride solution) in a 9 ml of the diluent using a mechanical shaker. The number of cells in the microbial suspension was adjusted in a range from 5.3×10^6 to 6.7×10^6 cfu/ml for bacteria and 6.0×10^5 cfu/ml for Candida yeasts, using diluent by turbidimetry.

For the determination of the bactericidal effect, 400 μ l of microbial suspension (5.3×10^6 a 6.7×10^6 cfu/ml for bacteria and 6.0×10^5 cfu/ml for yeast) were added to tablets prepared as for ion release tests. The antibacterial tests were carried out on two different sets of materials: the first set (coded as NON-COND) was used as synthesized; a second set (coded as COND) was used after conditioning by soaking into pH=7.4 buffer solution (Ca and Mg free Hank's Balanced Salt solution) for 15 days, i.e. in the same experimental conditions used for the analysis of ion release.

The test was executed in triplicate for every strain. After every contact time, through dilution, the total viable count (TVC) were calculated. The result was expressed in cfu/ml

For each test the number of cfu/ml in the test suspension was calculated (N) and the test method calculate Na. For each test organism was recorded the number of cfu/ml in the bactericidal test suspension (N) and after the test procedure for bactericidal activity of the product (Na). The reduction in viability was calculated as $N \times 10^{-1}/Na$.

3.2. Gallium-doped multisubstituted hydroxyapatite nanophases

Gallium is an ion present in trace in natural hydroxyapatite. It can substitute Ca in the apatite lattice because despite having a higher charge it has a lower ionic radius (Ca 114pm, Ga 76pm). The effect of Ga on bone cells has been studied and it has been found that Ga has antiresorptive properties, thus inhibiting osteoclast. Gallium has been tested against different disease of bones, such as bone tumor, infection and Paget's disease. Gallium is also found in human body in many proteins that bind Fe^{3+} , like transferrin or lactoferrin, because they have the same ionic charge and a similar ionic radius (Fe^{3+} 69pm), but not to hemoglobin, that can bind only Fe^{2+} . In fact antibacterial properties of Ga are given by its possibility to interfere with Fe homeostasis. The insertion of Ga in the HA lattice could confer new properties to the materials and could be an innovative method to exploit Ga properties through an in situ release. The simultaneous insertion of Mg and carbonate ions could improve the biomimicry and solubility of the new phase and give synergistic effects.

3.2.1. Synthesis

For the preparation of the new hydroxyapatite phases was chosen a precipitation method, particularly a neutralization reaction, between an aqueous suspension of calcium hydroxide

(Ca(OH)₂, Sigma Aldrich, 95% purity), 10g in 150ml, and a solution of phosphoric acid (H₃PO₄, Fluka, 85% purity), 9.72g in 100ml. The synthesis technique was chosen for the easiness of the reaction procedure and for the possibility of the insertion of foreign ions. To introduce foreign ions in the final product, gallium and magnesium ions were added by dissolving suitable reactants in the aqueous calcium suspension, i.e. gallium nitrate (Ga(NO₃)₃, Sigma Aldrich), for Gallium, and magnesium chloride (MgCl₂, Sigma Aldrich) for Magnesium. To introduce carbonate ions in the reaction vessel, a solution of calcium bicarbonate (NaHCO₃, Sigma Aldrich) was dropped in the basic suspension simultaneously with the phosphoric acid solution. The Ca/P ratio was set to 1.67, i.e. equal to that of stoichiometric hydroxyapatite. Additional ions were added, to induce substitutions in the apatite structure in defined extents. In the present work, undoped HA phase was synthesized as a reference material. Then gallium-doped materials were prepared, with different nominal X_{Ga} (where X_{Ga} is the molar ratio Ga/Ca). Also different multi-substituted materials were prepared with simultaneous substitution of Ga, with different X_{Ga} and Mg with X_{Mg} (where X_{Mg} is the molar ratio Mg/Ca) and carbonate with X_{CO₃} (where X_{CO₃} is the molar ratio CO₃/PO₄).

After the end of the dropping, the suspension was maintained under stirring for 2h to complete the reaction and homogenize the product. The whole synthesis process was carried out at 40 °C to limit the extent of crystallization of the final apatite phase. After 2h the suspension was closed and left overnight for maturation and deposition of the product. Then, the supernatant liquid was removed and the solid product was separated by the residual fluid by centrifugation, repeatedly washed in bi-distilled water, and finally dried at 40 °C. The dried powders were manually milled, sieved at 106 µm and stored in dry environment for further analysis.

Table 3.I initial molar composition

<i>Samples</i>	<i>Molar Ca/P</i>	X_{Mg}	X_{Ga}	X_{CO3}	<i>Tot cat/ PO₄</i>	<i>Tot cat/ Tot an</i>
HA	1.67	---	---	---	1.67	1.67
Ga-HA-1	1.67	---	0.025	---	1.70	1.71
Ga-HA-2	1.67	---	0.05	---	1.75	1.75
Ga-HA-3	1.67	---	0.1	---	1.69	1.84
Ga-MCHA-1	1.67	0.10	0.01	0.10	1.85	1.69
Ga-MCHA-2	1.67	0.15	0.01	0.10	1.94	1.76
Ga-MCHA-3	1.67	0.10	0.025	0.10	1.87	1.70
Ga-MCHA-4	1.67	0.15	0.025	0.10	1.95	1.78
Ga-MCHA-5	1.67	0.10	0.05	0.10	1.92	1.75
Ga-MCHA-6	1.67	0.15	0.05	0.10	2.00	1.82

3.2.2. Chemical characterization

XRD analysis reported that all the as-obtained materials were composed of hydroxyapatite (HA) only, (according to the reference pattern PDF card #09-0432), as showed in **Fig. 3.2**. No additional peaks belonging to other crystalline phases were detected.

The XRD spectra of the various doped materials are characterized by broader patterns, if compared with the reference HA, that could be ascribed to a reduction in the crystal ordering due to introduction of foreign ions into the HA structure [23] [24] [25] [26] [27]. The crystallinity index (C.I.) or splitting factor (S.F.) [28] reveals that HA is the most ordered of the examined phases (C.I.=3.68). Considering only the Ga mono-substituted phases was seen a decrease in the C.I. with the increase of Ga substitution (Ga-HA-1=3.40 Ga-HA-2=3.26 Ga-HA-3=3.01).

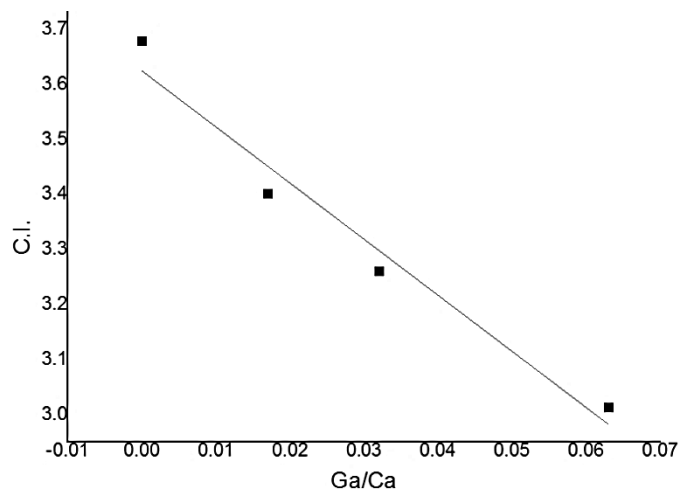


Figure 3.1. Decrease of the splitting factor or crystallinity index (C.I) depending from Ga/Ca ratio.

In this respect, considering only monosubstituted Ga-HA, full profile analysis by Rietveld method evidenced a slight deformation of the HA lattice (**Tab. 3.II**), particularly an increase of the a cell parameter and a decrease of the c parameter that could be ascribed to the entering of Ga^{3+} ions in substitutional position into the calcium sites of the HA lattice, thus yielding a general increase of the cell volume.

Table 3.II Crystallographic analysis of the as-obtained new monosubstituted phases.

<i>Sample</i>	<i>a</i> (Å)	<i>c</i> (Å)	<i>c/a</i>	<i>Cell Vol.</i> (Å ³)	<i>D_{av}</i> (nm)	<i>D₃₀₀</i> (nm)	<i>D₀₀₂</i> (nm)	<i>D₀₀₂/D₃₀₀</i>	<i>C.I.</i>
HA	9.432 (1)	6.895 (1)	0.731 (1)	531.2 ±0.1	21.3 ±2.1	22.8 ±0.4	56.0 ±1.5	2.46	3.68
Ga-HA-1	9.433 (2)	6.895 (2)	0.731 (1)	531.4 ±0.2	11.2 ±1.3	16.3 ±1.2	30.9 ±0.8	1.90	3.40
Ga-HA-2	9.434 (2)	6.890 (2)	0.730 (1)	531.4 ±0.3	12.4 ±1.4	18.0 ±0.8	32.9 ±0.6	1.83	3.26
Ga-HA-3	9.444 (1)	6.889 (1)	0.729 (1)	532.1±0. 2	11.0 ±1.4	15.4 ±2.1	30.9 ±0.8	2.01	3.01

The HA lattice distortion was more pronounced when also Mg^{2+} ions were introduced in the HA structure, with a more marked reduction of the a axis and of the overall cell volume. This effect is ascribable to the presence of Mg that, as previously reported [29], could reduce significantly the a axis when introduced in substitutional position into the HA lattice and, due to its smaller volume, could yield reduction of the lattice volume.

Table 3.III Crystallographic analysis of the as-obtained new multisubstituted phases.

<i>Samples</i>	<i>a</i> (Å)	<i>c</i> (Å)	<i>c/a</i>	<i>Cell Vol.</i> (Å ³)	<i>D_{av}</i> (nm)	<i>D₃₀₀</i> (nm)	<i>D₀₀₂</i> (nm)	<i>D₀₀₂/</i> <i>D₃₀₀</i>	<i>Splitting</i> <i>factor</i>
Ga- MCHA-1	9,402 (6)	6,905 (0)	0.734 (4)	528,7 ±0,2	11.8 ±1.5	18,8 ±1,2	25,1 ±0,8	1.34	2.94
Ga- MCHA-2	9,416 (5)	6,886 (2)	0.731 (2)	528,8 ±0,1	17.5 ±1.2	21,6 ±1,0	40,4 ±1,1	1.84	2.89
Ga- MCHA-3	9,405 (7)	6,884 (1)	0.731 (9)	527,4 ±0,1	13.7 ±1.1	16,2 ±0,7	29,8 ±0,6	1.87	2.99
Ga- MCHA-4	9,402 (7)	6,905 (0)	0.7343 (6)	528,7 ±0,2	11.7 ±1.4	19,6 ±1,2	24,9 ±0,8	1.27	2.74
Ga- MCHA-5	9,406 (1)	6,891 (0)	0.732 (6)	528,0 ±0,1	15.3 ±1.1	20,3 ±0,9	35,2 ±1,4	1.73	2.70
Ga- MCHA-6	9,402 (4)	6,898 (9)	0.733 (7)	528,2 ±0,2	12.1 ±1.3	20,6 ±1,1	31,2 ±1,0	1.51	2.68

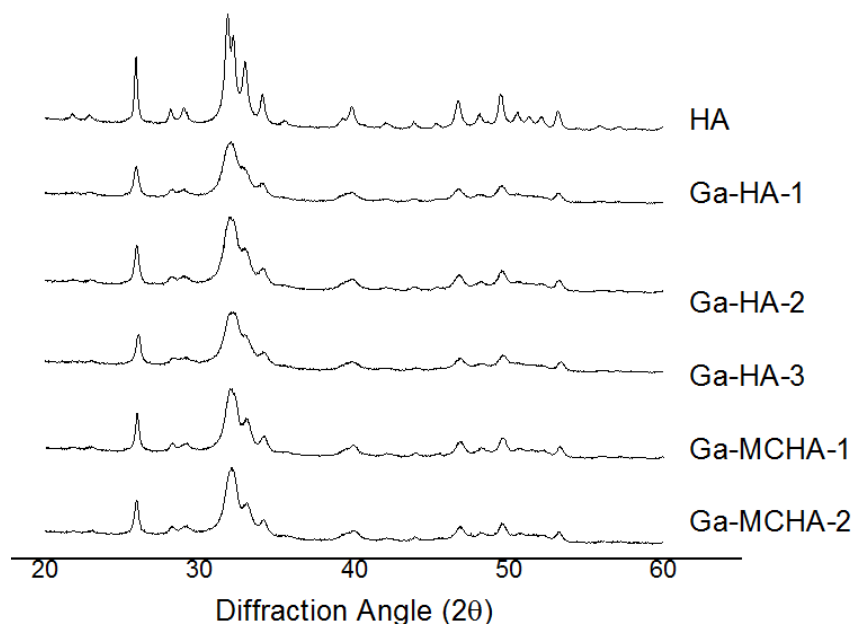


Figure 3.2. XRD patterns of undoped and some doped materials.

The analysis of the crystal size reported an average crystallite size of 21.3 ± 2.1 nm in undoped HA. In comparison, the Ga-doped HA phases showed a marked reduction of the crystallite size, (11.5 ± 0.7 nm) whereas in multi-doped materials it tends to increase again (13.7 ± 2.3 nm). By separate evaluation of the domain size along the two orthogonal axes of the hexagonal HA lattice, it was found that all the HA phases showed anisotropic crystal development along the *c* axis. However, crystal anisotropy tended to decrease in substituted HAs and even more markedly in the multi-substituted materials (**Table 3.II-3.III**).

FTIR spectra collected on the new doped apatites (**Figure 3.3**) showed the characteristic absorption bands of phosphate group at $980\text{--}1100$ and $560\text{--}600$ cm^{-1} . As the water adsorbed on the powdered samples was eliminated by heating prior to FTIR spectra acquisition, the broad bands at ~ 3500 cm^{-1} and at 1640 cm^{-1} only addressed the presence of structural water into the HA structure [30]. The FTIR adsorption bands appear weakly resolved, and the crystallinity index reported in **Table 3.II**. and **Table 3.III**. confirm the reduced crystallinity degree related to

the ionic substitutions in doped materials. In particular, the splitting factor decreased at higher amounts of gallium, and further decreased when also magnesium and carbonate were added. FTIR analysis reported also the presence of carbonate in the doped apatitic phases, particularly with the absorption bands at ~ 1450 , 1430 and 870 cm^{-1} , confirming that the carbonate group substituted the phosphate group (B-type substitution) in all the new phases (see **Figure 3.3**) [31].

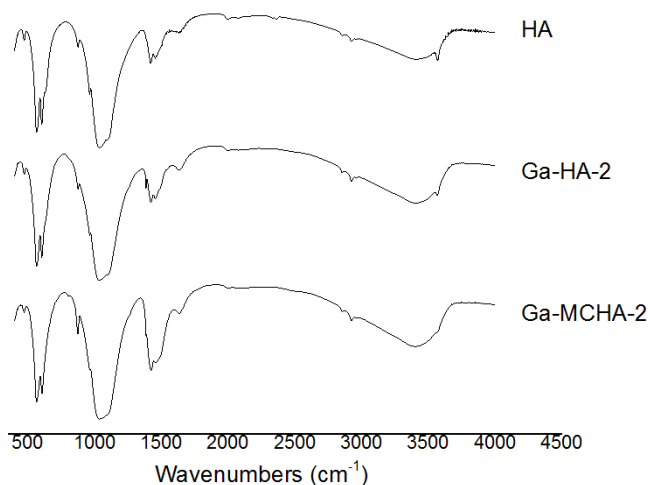


Figure 3.3. FTIR spectra of some different substituted hydroxyapatites.

FTIR spectra also highlighted the reduction of the OH^- absorption peak at 3570 cm^{-1} in Ga-HA-2 and, in higher extent, in Ga-MCHA-2 (similar amount of Gallium but also containing Mg and CO_3), if compared to undoped HA. Also, an increase of the carbonation extent in multi-doped phases with the increase of Gallium content was detected (**Table 3.IV**). These findings suggested that the expulsion of OH^- groups could be an effect of the substitution of Ga^{3+} for Ca^{2+} in the HA lattice; in fact, ionic substitutions could yield calcium vacancies and thus a general decrease of the calcium content, as reported in **Table 3.II** and also previously observed by and, in association with an excess of the negative charge. Therefore, the elimination of OH^- groups would restore the overall charge balance in the HA lattice.

Another possible mechanism for the compensation of the excess negative charge could be the enhanced carbonation detected in the multisubstituted Ga-Mg-CO₃ apatites, that could be explained by the claimed ability of magnesium to favor the CO₃ uptake in HA.

The chemical analysis of the as-obtained powders, reported in **Table 3.IV**, shown that Ga is really found in the final apatite but only a fraction of gallium nominally introduced in the reaction vessel remained incorporated in the apatite structure.

Table 3.IV Chemical analysis of the as-obtained new phases.

<i>Samples</i>	<i>Actual Ca/P</i>	<i>Actual Ga/Ca</i>	<i>Ga yield (%)</i>	<i>Actual Mg/Ca</i>	<i>Mg yield (%)</i>	<i>Actual C/(P+C)</i>	<i>Tot cat./ Tot an.</i>
HA	1.69	0.000	---	---	---	0.022	1.65
Ga-HA-1	1.72	0.017	68	---	---	0.048	1.67
Ga-HA-2	1.64	0.032	64	---	---	0.054	1.61
Ga-HA-3	1.55	0.063	63	---	---	0.048	1.57
Ga-MCHA-1	1.75	0.0062	62	0.068	68	0.11	1.69
Ga-MCHA-2	1.69	0.0061	62	0.079	53	0.098	1.70
Ga-MCHA-3	1.72	0.016	64	0.046	46	0.088	1.68
Ga-MCHA-4	1.67	0.017	68	0.062	41	0.11	1.62
Ga-MCHA-5	1.66	0.031	62	0.033	33	0.075	1.64
Ga-MCHA-6	1.73	0.032	64	0.30	20	0.12	1.64

Considering only mono-substituted Ga-HA an average yield of Ga incorporation of $65.0 \pm 2.6\%$ is reached. Considering instead multi-substituted Ga-MCHA, the materials co-doped with Ga, Mg and CO₃ ions, the average yield of Ga incorporation was maintained at similar levels: $63.5 \pm 2.5\%$. From this data is possible to conclude that the presence of Mg does not affect the substitution of Ca with Ga. The total average yield of Ga substitution is $64.0 \pm 2.5\%$.

Also Mg does only a fraction of the Mg inserted enter in the final product of the reaction. The yield of Mg entering in the final product decrease for two different reason. A first reason is the

X_{Mg} . It is possible to observe that the yield of Mg inserted in the final phase decrease at the increasing of the X_{Mg} maintaining constant the X_{Ga} . A second effect is the decrease of the yield of Mg yield in function of Ga inserted, as showed in **Fig. 3.4**.

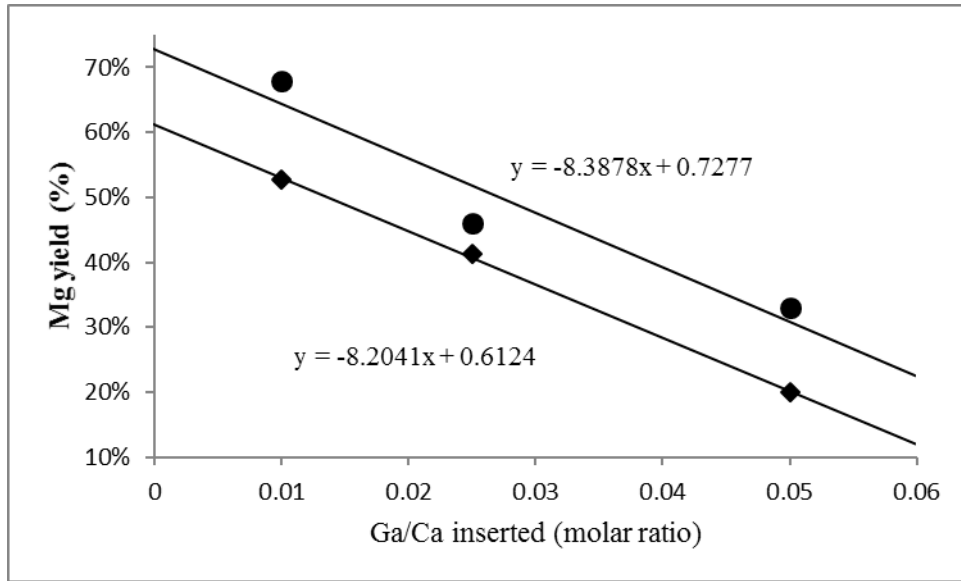


Fig. 3.4. Correlation between Mg yield and Ga/Ca inserted molar ratio (● initial $X_{Mg} = 0.10$, ◆ initial $X_{Mg} = 0.15$)

The two different lines of **Fig.3.4.** corresponds to the two different initial Mg/Ca molar ratio used. There is difference between the two lines but the slope remain the same and could be considered typical of the co-substitution Mg-Ga. The explanation of the decrease of Mg insertion at the increase of Ga content could be hypothesized. The introduction of gallium and the consequent modification of the lattice structure, could result in a detrimental effect in respect to Mg entering. Between the two ions Mg is the only influenced by this aspect because it is not strongly bonded to HA. The incorporation of carbonate groups occurred spontaneously in the reference and Ga-substituted HA samples, as an effect of the dissolution of CO_3^{2-} ions from the air atmosphere into the aqueous alkaline suspension containing $Ca(OH)_2$ [32]. In this respect the presence of gallium significantly enhanced the apatite carbonation in B site. In fact, in the multi-

doped materials the highest carbonation extent occurred in the samples with the highest amount of gallium (Ga-MCHA-6), (see **Table 3.IV**).

3.2.3. Ion release test

To investigate the potential bioactivity and effect on bacteria of the doped and multi-doped powders, the release of ions in simulated physiological fluid was recorded for Ga-HA-2, Ga-HA-3 and Ga-MCHA-5 materials, in comparison with the reference, the undoped HA. Those phases were selected to possibly put in evidence dose dependent effects of Ga (between Ga-HA-2 and Ga-HA-3) as well as of magnesium/carbonate co-substitutions (between Ga-HA-2 and Ga-MCHA-5, that have the same X_{Ga}).

A marked effect on the apatite solubility was detected, in relationship with the amount and type of foreign ions. The release profiles of Ca, Mg and Ga in all the investigated materials can be described as the effect of two distinct release mechanisms, characterized by an initial stage of burst ion release, particularly in the first 3 days, followed by a slower release profile (**Figures 3.5 and 3.6**). The calcium release rate increased steadily with calcium content in Ga-doped apatites but, unexpectedly, decreased in multi-doped materials. During the whole period of investigation, low relative amounts of calcium and gallium ions were released (**Figure 3.6**). Marked effects were recorded for the release of magnesium from multi-doped apatite, Ga-MCHA-5, which released more than 10 wt% of magnesium in the first 24 hours, and more than 20 wt% after 15 days. The same material also released the highest amount of gallium (**Figs. 3.5 and 3.6**), in spite it was only a bit more than 1 wt% of the initial amount.

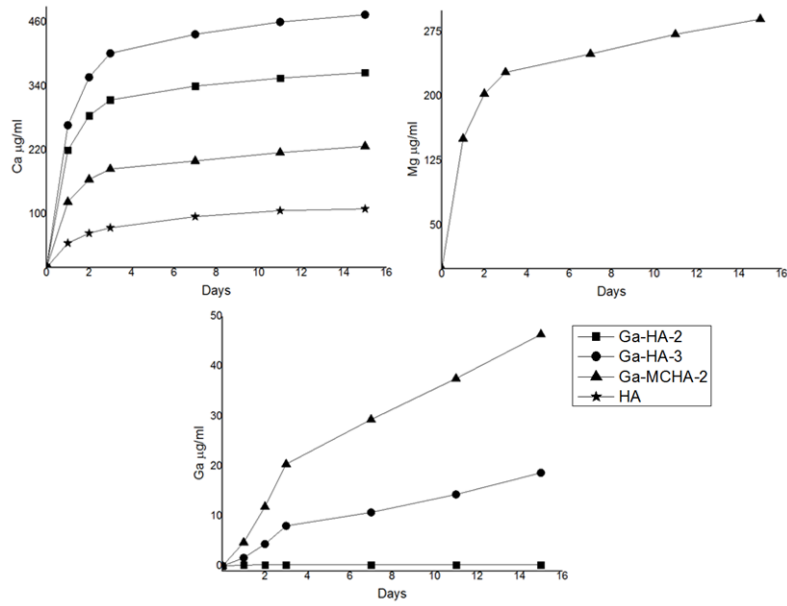


Figure 3.5. Ion release tests for all the selected composition. The results are expressed as absolute concentrations.

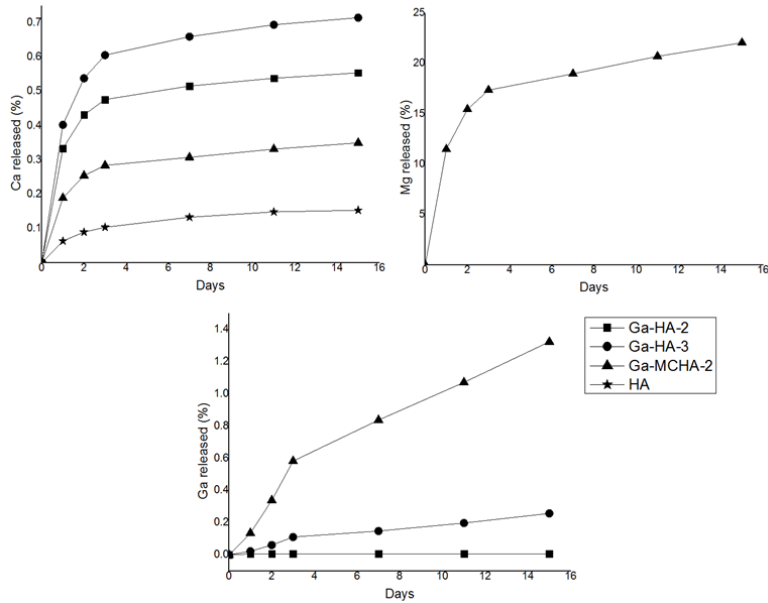


Figure 3.6. Ion release tests for all the selected composition. The results are showed as percentage ion loss in respect to the starting material.

3.2.4. Biological characterization

In vitro cell analysis was carried out on three selected materials: Ga-HA-2, Ga-MCHA-5 and the undoped HA, as a reference. The ACSs behavior in contact with two different concentrations of powders was investigated *in vitro* looking at the cell viability, cell morphology and cell differentiation up to 14 days of culture. The quantification of metabolically active cells showed a significant enhancement in cell proliferation induced by the presence of Ga, in detail Ga-MCHA-2 at the higher concentration starting from day 3 with respect to HA group (Fig. 6). At the lower concentration, increased cell viability was seen at day 7 for Ga-MCHA-5 respect to HA group (Fig. 3.7).

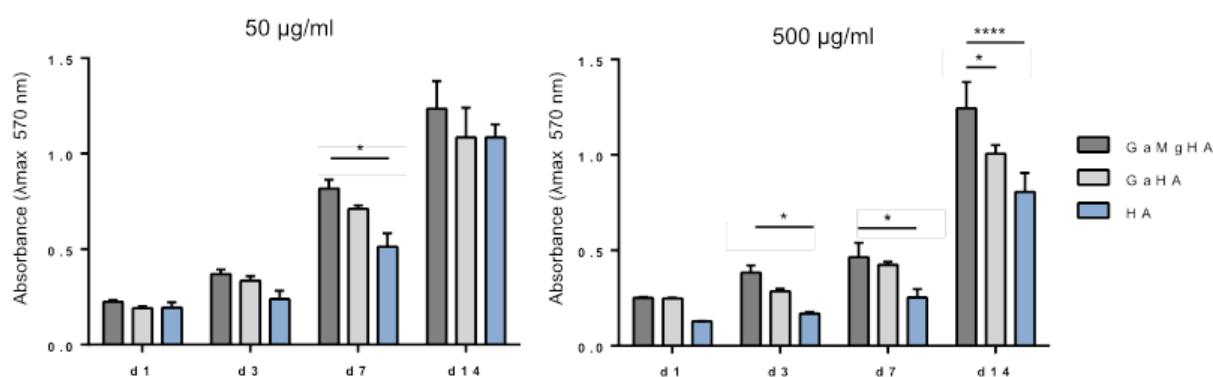


Figure 3.7. Analysis of cells proliferation by MTT assay, after 1, 3, 7 and 14 days of ASCs seeded with 50 µg/ml and 500 µg/ml of the new phases. * $p \leq 0.05$; **** $p \leq 0.0001$. $n = 3$.

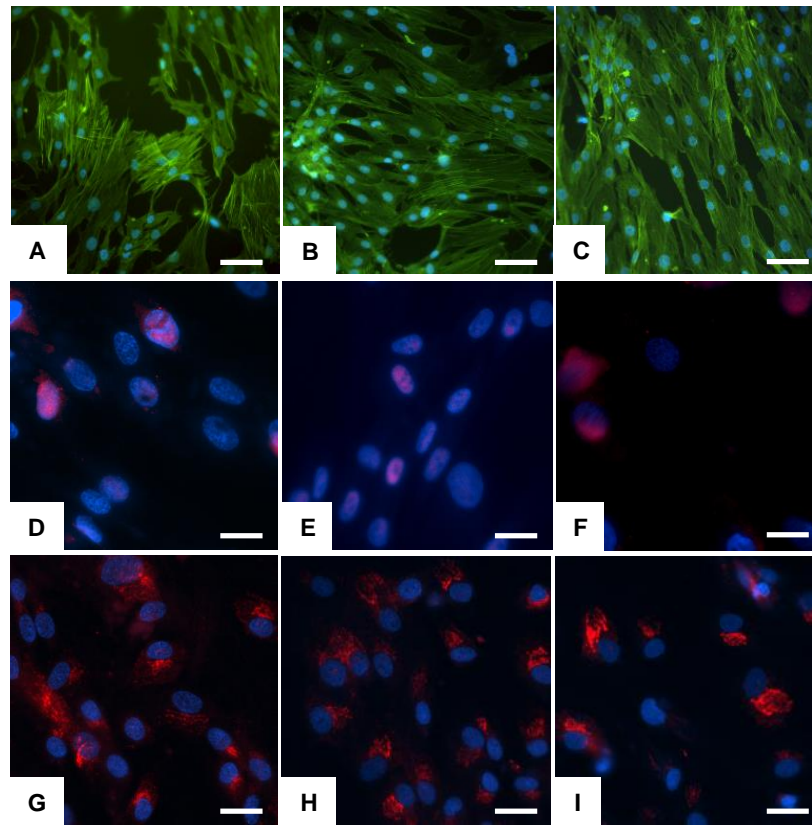


Figure 3.8. Analysis of cell morphology at day 3 seeded with the higher concentration of samples (A-C). Phalloidin in green stains for actin filaments and DAPI in blue stains for cell nuclei. Immunofluorescent analysis of RUNX2 (D-F) at day 7 (500 $\mu\text{g/ml}$). Staining of RUNX2 (in red) and cell nuclei (in blue). Immunofluorescent analysis of COL-I (G-I) at day 7 (500 $\mu\text{g/ml}$). Staining of COL-I (in red) and cell nuclei (in blue). A, D and G: HA group. B, E and H: GaHA. C, F and I: GaMgHA. Scale bars: A-C 80 μm ; D-F 30 μm ; G-I 50 μm .

Morphological evaluation of ASCs seeded in culture with the new phases was a further marker of cytocompatibility of the samples. The results showed no changes in cell morphology induced by the presence of the foreign ions Ga, Mg and CO_3 in the apatite structure, as highlighted by actin filaments staining. Cells were well spread and firmly attached to the well plates without difference among groups and concentrations (**Fig.3.8**).

In order to assess any osteoinductive effect of the new phases on ACS differentiation, gene expression analysis of ALPL was evaluated by qPCR, and RUNX2 and COL-I proteins were qualitative detected by immunofluorescent analysis. The results showed that ALPL was

significantly up regulated by the presence of the highest concentration of Ga-MCHA-5 only at day 14 with respect to Ga-HA-2 (*p≤ 0.05) and HA (*p≤ 0.05) used as control group (**Fig. 3.9**). Instead, the lower concentration of the Ga-MCHA-5 did not have any effect of the ALPL expression (**Fig. 3.9**). By fluorescent antibody labeling, RUNX2 and COL-I, early markers associated with osteoblast differentiation, were visualized after 7 days of culture and no qualitative differences were seen among the groups at both concentrations (**Fig. 3.8**).

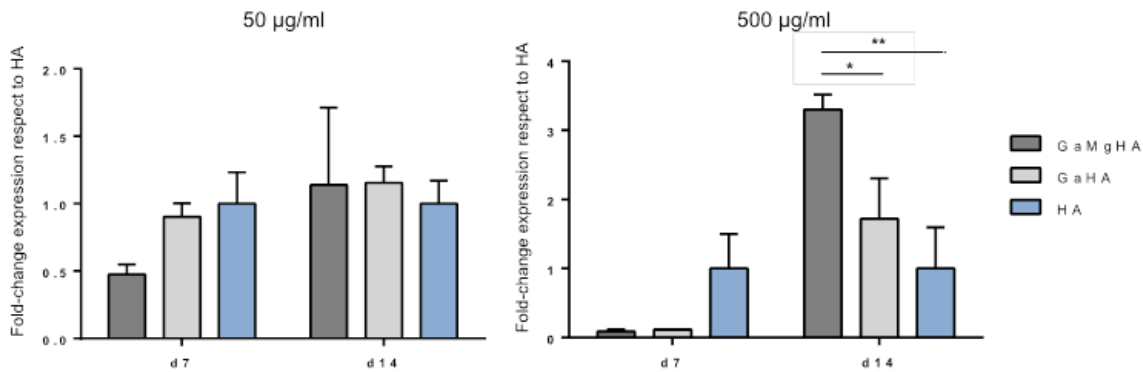


Figure. 3.9: ALPL gene expression analysis. Relative quantification ($2^{-\Delta\Delta Ct}$) of gene expression after 7 and 14 days of ASCs cultured in contact with all the samples. Mean and standard error of the technical triplicate of ALPL, with respect to the expression of cells in contact with HA, used as control. (*p≤ 0.05; ** p≤ 0.01).

3.2.5. Antibacterial test

The new materials already tested for ion release (HA, Ga-HA-2, Ga-HA-3, Ga-MCHA-5) were used also for antibacterial tests. The antibacterial effect of the new phases was tested with 4 different bacterial strains and yeast (*Pseudomonas Aeruginosa*, *Escherichia Coli*, *Staphylococcus Aureus* and *Candida Albicans*, respectively two gram-, one gram+ and a yeast). The antibacterial tests were carried out on two different sets of materials: the first set (coded as NON-COND) was used as synthesized; a second set (coded as COND) was used after conditioning by soaking into

pH=7.4 buffer solution (Ca and Mg free Hank's Balanced Salt solution) for 15 days, i.e. in the same experimental conditions used for the analysis of ion release. The results of the bacterial reduction are showed in **Figures 3.10 and 3.11**, for NON-COND and COND sets of samples, respectively. All NON-COND samples showed ability of bacterial reduction higher than 80% after 24 hours. Also, the analysis of NON-COND samples evidenced a higher antibacterial activity in the Ga-substituted apatites, in respect to the undoped HA. Moreover bacterial inactivation was reached more rapidly in doped and, particularly, in multi-doped materials.

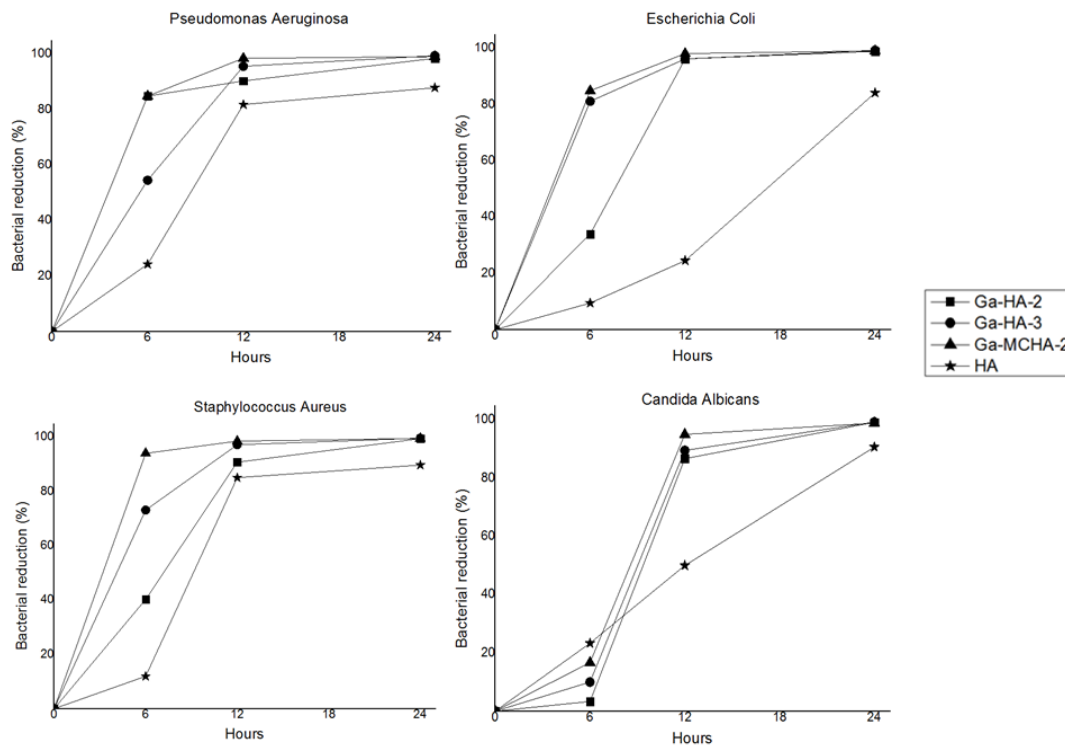


Figure 3.10. Bacterial reduction for all the bacterial strains and all the compositions tested (NON-COND).

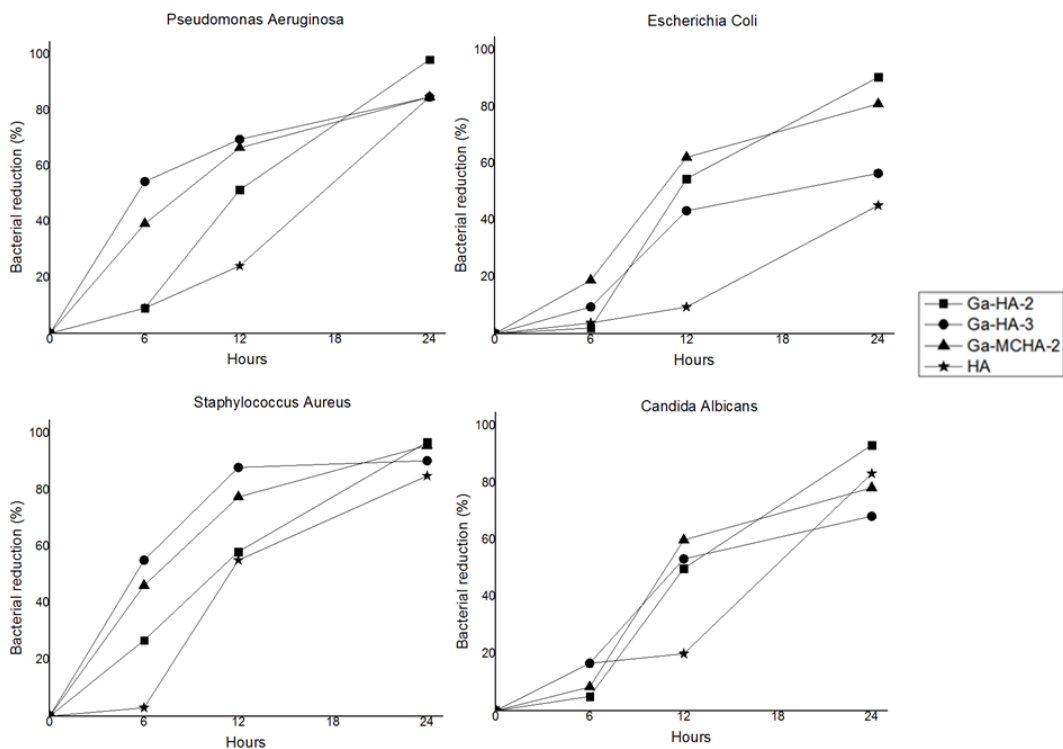


Figure 3.11. Bacterial reduction for all the bacterial strains and all the compositions tested (COND).

The analysis of the COND samples evidenced slower, and more specific activity of bacterial reduction; particularly, *Escherichia Coli* and *Candida Albicans* showed higher resistance to inactivation, whereas a strong antibacterial effect was confirmed for *Staphylococcus Aureus*. The effect of gallium on the bacterial inactivation was confirmed in the COND samples series; the most marked effects were recorded for *Pseudomonas aeruginosa* and *Staphylococcus Aureus*. In all the groups the undoped HA was confirmed as the less effective agent against bacterial proliferation, for all the considered strands.

3.2.6. Discussion

New ion-substituted nanocrystalline apatites were synthesized by direct introduction of gallium and other foreign ions into the apatite crystal during its formation in aqueous medium. The evidence of a direct relationship between the initial amount of gallium and the extent of

incorporation in the structure of the final apatite (see ICP analysis in **Table 3.IV**) opens to the possibility to obtain Ga-doped apatites as pure nanocrystalline phases with designed ion content (See **Figure 3.2**, **Table 3.II**, **Table 3.III** and **Table 3.IV**). The effect of Ga doping on the HA crystals development was evidenced by the reduced crystallinity, lattice distortion and, also, the strong reduction of the domain size (see **Table 3.II** and **Table 3.III**). All these effects were previously reported in the case of doped and multi-doped hydroxyapatite, as an effect of effective ion substitution in the apatite lattice [9] [22] [26] [32] [33] [34]. Particularly, the increase of cell volume in Ga-doped HA suggested a substitutional positioning of Ga^{3+} ions in the HA lattice, due to its larger volume compared to Ca^{2+} . The effective entering of gallium is also confirmed by the reduction of OH^- groups and the increase of spontaneous carbonation (see **Figure 3.3** and **Table 3.IV**), as an effect of charge imbalance occurring upon ion substitution. These results confirm the ability of the apatite structure to easily accommodate the introduction of foreign ions and to balance the electric charge by expulsion of charged groups such as hydroxyl ions, as already showed in previous studies [33].

In the case of multiple substitution with also Mg and CO_3 , various effects on the HA crystal development co-existed. The chemical analysis of the new apatites highlighted that higher amounts of gallium limited the incorporation of magnesium in the final apatite (**Table 3.IV**). In respect to single-substituted Ga-HAs, the introduction of additional Mg^{2+} and CO_3^{2-} ions provoked further reduction of the apatite lattice volume, but a marked increase of the coherent domain size. This finding suggests that at least a fraction of the initial Mg^{2+} ions could enter into the apatite lattice, thus substantially enhancing the crystal instability in respect to the feasibility of incorporation of the larger gallium ions; in such conditions the apatite lattice characterized by a reduced volume could develop and grow, but in a lesser extent than the lattice of the undoped

apatite. Hence, even though the presence of gallium seemed to prevent the incorporation of magnesium in the final material, it is evident that the co-doping substantially hampered the population of the apatite crystal sites with gallium, whereas partial substitution of calcium with magnesium resulted more energetically favored.

Therefore, in the simultaneous presence of magnesium, gallium ions could be segregated in the disordered layer typically present in low crystallinity apatites [35], rather than being included in the HA lattice. This hypothesis is supported by the much higher release of gallium in Mg-CO₃ co-substituted apatites (**Figure 3.5** and **Figure 3.6**), as gallium ions included in a non-crystalline structure were likely more weakly bound to the HA structure. Co-doped HAs showed a lower release of calcium, instead; this can be considered as a marker of the higher stability of the apatite lattice in co-doped materials, in respect to single-substituted Ga-HAs.

The incorporation of at least a fraction of gallium and magnesium ions into the disordered non-apatitic layer in all doped HAs can also explain the two-stage release kinetics recorded during the test (**Figures 3.5, 3.6**). In this respect, the early stage of release could involve mainly those ions included in the superficial non-apatitic layers surrounding the more crystalline cores, whereas the subsequent stage, characterized by a less steep straight line, could be referred to ions released by inner and more crystalline layers. Apatite carbonation in B position is a relevant phenomenon for biological purposes, as it confers enhanced solubility in vivo and affinity with cells [36][36][36][36][36][36][36][36][36]. It can spontaneously occur during the HA synthesis, as carbon dioxide present in the air atmosphere can dissolve in the alkaline suspension where the HA phase nucleates and mature [32]. The ICP and TG analyses in **Table 3.IV** showed that the presence of gallium favored the spontaneous apatite carbonation, whereas it did not hamper retention of carbonate groups when apatite was introduced in the reaction vessel.

In respect to stoichiometric, undoped apatite, the higher solubility and the presence of multiple ions in the apatite structure can represent a source of signals for cells in assistance to the bone regenerative cascade. Recently mesenchymal stem cells have attracted a lot of attention for therapeutic uses due to the great ability to differentiate into cellular phenotypes of several tissues including cartilage, bone, muscle, nervous system, and they also regulate the innate immune system. In this view adipose tissue represents an abundant and accessible source of adult stem cells with the ability to differentiate in bone cells (i.e. osteoblasts) [37] [38]. Focusing on a synergistic use of biomaterial and cellular therapy in certain orthopedic disorders (e.g. osteoporosis), a pilot *in vitro* study was performed [39] to evaluate for the first time the ACSs behavior in response to the new multi-substituted apatite phases, subject of the present study. Our results showed that Ga-doped HAs did not negatively affected cell morphology that maintained their fibroblast-like (elongated spindle) morphology with abundant cytoplasm and large nuclei. Besides, when combined with Mg cell viability and the up regulation of ALPL osteo-related gene were significantly enhanced.

Despite their positive effect on human adipose mesenchymal stem cells, all the tested apatites showed a remarkable bactericidal effect, particularly enhanced in the new multi-substituted apatites (**Figures 3.10 and 3.11**), on four major post-surgery infective lines, including three different types of infective agents: gram positive, gram negative and yeast. The comparison between the two COND and NON-COND sample series highlighted that undoped HA was the material with lower antibacterial effect in all cases; also, in respect to non-conditioned samples a retard in the bacterial reduction effect for conditioned materials was detected and, particularly for *E. Coli* and *C. Albicans*, a reduced antibacterial effect after 24 hours. This finding suggests that the intensive ion release occurring during the first day in the culture medium could have induced

a faster bacterial reduction in the NON-COND series. However, in COND samples a remarkable antibacterial effect was maintained, in spite a much slower ions release was expected in these samples, as suggested by data showed in **Figures 3.5 and 3.6**. This suggests the activation of a different inactivation mechanism in COND samples, induced by the residual surface charge of the investigated apatites, rather than by the ionic strength of the environment enhanced by the intensive ion release.

For some bacterial strands a specific effect of Gallium could be evidenced, even though precise dose-dependent effects could not be observed. These preliminary results, however, encourage to investigate Ga-Mg-CO₃-doped apatites as a new system with antibacterial effect. Indeed, substituted apatite phases have been widely developed in previous research, with the purpose to mimic the inorganic part of bone; however, the present study shows that ion-substituted apatites can display additional antibacterial functionality that can be exploited for the production of bone implants or of coating for prostheses, thus being able to promote and sustain new bone formation and, at the same time, to lower the occurrence of infections and biofilm formation at the interface between the implant and the native bone, thanks to the steady and prolonged release of active ions. These two factors can significantly improve the bone healing process in a number of clinical cases, with positive impact on the health and wellness of the population. In particular, the outcomes of the *in vitro* tests, along with the well-known HA effect on several genes involved in osteogenesis [40] [41], and along with the proved significant increase in bone calcium content occurring in gallium-treated bone (reducing the osteoclast activity) [42] [43], demonstrate the promising features of these multi-substituted apatites in bone homeostasis regulation in degenerative diseases like osteoporosis.

3.2.7. Conclusion

The steady increase of disabling bone diseases requires effective and durable therapies for effective tissue healing and, also, to prevent undesired secondary effects jeopardizing or retarding the healing process. In this respect, the novel multi-doped apatites developed in this work are promising as cell-instructive biomaterials with double functionality of enhanced osteogenic and antibacterial effect, in comparison with undoped and single-doped apatites. Particularly, the doping with gallium was effective in inducing antibacterial effect against some bacterial strands, without reducing the viability of human cells. However, apatites multi-doped with magnesium and carbonate demonstrated enhanced effects, in respect to the expression of genes relevant for the regenerative cascade and of the inactivation of all the studied infective agents.

These results show, for the first time, that gallium can be incorporated in designed amounts, in the structure of nanocrystalline apatites, as effective antibacterial agent; in addition, the present work confirmed the relevant role of magnesium and carbonate in the bone regeneration process, so that the association of such key properties makes the multi-doped apatites developed in this work as novel multi-functional materials for the preparation of advanced scaffolds or coatings for bone implants.

3.3. Zinc-doped multisubstituted hydroxyapatite nanophases

Zinc is a fundamental ion present in the human body and is also present in natural hydroxyapatite. It can substitute Ca in the apatite lattice because, it is isovalent with it and has a lower ionic radius (Ca 114pm, Zn 74pm). In this respect, Zn doped calcium phosphates have been already studied. A first in vivo study was performed on rabbit using Zn-TCP and biphasic Zn-TCP/HA with excellent results [44]. Then, hydroxyapatites doped with Zn were developed finding enhanced ability to promote osteoblast adhesion and proliferation as well as differentiation and proliferation of human adipose mesenchymal stem cells. The antibacterial properties of Zn-HA were also studied, thus finding specific inhibitory effect against *Staphylococcus Aureus* [45]. In this chapter zinc substituted HA (Zn-HA) and zinc-magnesium-carbonate multi-substituted HA (Zn-MCHA) phases were synthesized to explore with a larger number of bacterial strain the efficacy of Zn-HA as antibacterial agent and to find synergistic effects when is present a simultaneous substitution of Zn, Mg and carbonate, that could improve biomimicry and solubility of the phase.

3.3.1. Synthesis

For the preparation of the new hydroxyapatite phases a precipitation method was used, particularly a neutralization reaction, between an aqueous suspension of calcium hydroxide ($\text{Ca}(\text{OH})_2$, Sigma Aldrich, 95% purity), 10g in 150ml, and a solution of phosphoric acid (H_3PO_4 , Fluka, 85% purity), 9.72g in 100ml. The synthesis technique was chosen for the easiness of the reaction procedure and for the possibility of the insertion of foreign ions during the formation of

the apatite crystals. To introduce foreign ions in the final product, cations, zinc and magnesium, were added by dissolving suitable reactants in the aqueous calcium suspension, zinc nitrate ($\text{Zn}(\text{NO}_3)_2$, Sigma Aldrich), for Zinc, and magnesium chloride (MgCl_2 , Sigma Aldrich) for Magnesium. To introduce carbonate anions in the reaction vessel, a solution of calcium bicarbonate (NaHCO_3 , Sigma Aldrich) was dropped in the basic suspension simultaneously with the phosphoric acid solution. The Ca/P ratio was set to 1.67, i.e. equal to that of stoichiometric hydroxyapatite. Additional ions were added, to induce substitutions in the apatite structure in defined extents, listed in **Table 3.V.** In the present work, undoped HA phase was synthesized as a reference material. Then zinc-doped materials were prepared, with different nominal X_{Zn} (where X_{Zn} is the molar ratio Zn/Ca). Also different multi-substituted materials were prepared with simultaneous substitution of Zn, with different X_{Zn} , and Mg, with different X_{Mg} (where X_{Mg} is the initial molar ratio Mg/Ca), and carbonate with X_{CO_3} (where X_{CO_3} is the initial molar ratio CO_3/PO_4).

Table 3.V. initial molar composition

<i>Samples</i>	<i>Molar Ca/P</i>	X_{Mg}	X_{Zn}	X_{CO_3}	<i>Tot cat/ PO₄</i>	<i>Tot cat/ Tot an</i>
HA	1.67	---	---	---	1.67	1.67
Zn-HA-1	1.67	---	0.05	---	1.75	1.75
Zn-HA-2	1.67	---	0.1	---	1.84	1.84
Zn-CHA-1	1.67	---	0.05	0.15	1.75	1.52
Zn-MCHA-1	1.67	0.1	0.015	0.15	1.86	1.62
Zn-MCHA-2	1.67	0.1	0.03	0.15	1.89	1.64
Zn-MCHA-3	1.67	0.05	0.05	0.15	1.84	1.60
Zn-MCHA-4	1.67	0.1	0.05	0.15	1.92	1.67
Zn-MCHA-5	1.67	0.15	0.05	0.15	2.00	1.74

After the end of the dropping, the suspension was maintained under stirring for 2h to complete the reaction and homogenize the product. The whole synthesis process was carried out at 40 °C to limit the extent of crystallization of the final apatite phase. After 2h the suspension was closed and left overnight for maturation and deposition of the product. Then, the supernatant liquid was removed and the solid product was separated by the residual fluid by centrifugation, repeatedly washed in bi-distilled water, and finally dried at 40 °C. The dried powders were manually milled, sieved at 106 µm and stored in dry environment for further analysis.

3.3.2. Chemical characterization

XRD analysis reported that all the as-obtained materials were composed of hydroxyapatite (HA) only, (according to the reference pattern PDF card #09-0432), as showed in **Figure 3.12**. No additional peaks belonging to other crystalline phases were detected. The XRD spectra of the various doped materials are characterized by broader patterns, if compared with the reference HA, that could be ascribed to a reduction in the crystalline order due to the introduction of foreign ions into the HA structure [24] [25] [26] [27]. The variation of the crystal index is particularly evident in multi-substituted Zn-MCHA materials (average C.I.= 3.16) and reveals that HA is the most ordered among the examined phases (C.I.=3.68). Another important variable on peak broadening is the dimension of crystallites. The dimension of non-substituted HA is 21.3nm while the average dimension for the substituted phases is 14.03nm, without significant difference between the mono- and multi- substituted phases. Particularly in the mono-substituted phases it is possible to find a dose-dependency with the average crystallites dimension. The average dimensions decreased linearly with the increase of Zn content, as shown in **Figure 3.13**.

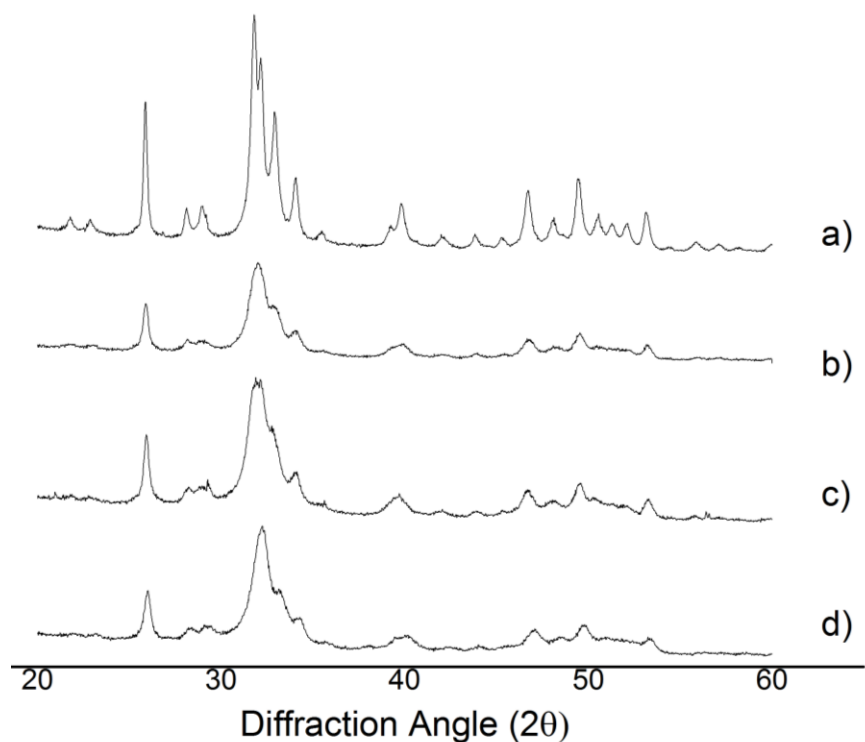


Figure 3.12. XRD patterns of undoped and some doped materials. (a) HA, b) Zn-HA-1, c) Zn-HA-2 and d) Zn-MCHA-5

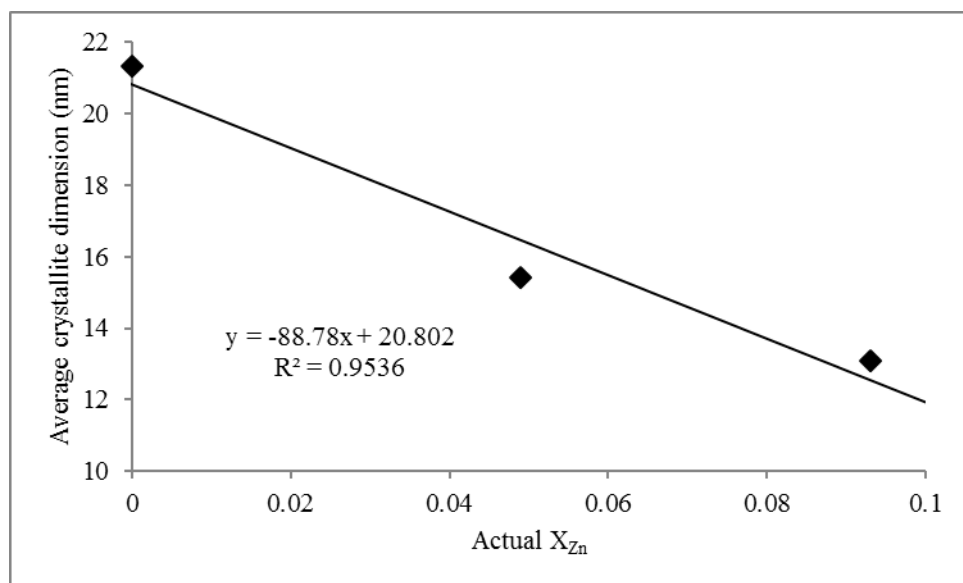


Figure 3.13. Variation of average crystallite dimension in Zn-HA in function of actual Zn content

In this respect, considering only mono-substituted Zn-HA, full profile analysis by Rietveld method evidenced a slight deformation of the HA lattice (**Table 3.VI.**), particularly an increase of the a cell parameter, particularly evident in Zn-HA-2, the phase with the maximum content of Zn, and a decrease of the c parameter that could be ascribed to the entering of Zn^{2+} ions in substitutional position into the calcium sites of the HA lattice, thus yielding to a decrease of the c/a ratio. The decrease of the c axis continue also for multi-substituted powders while the effect on the a axis is more difficultly valuable because the concomitant substitution of Mg^{2+} result instead in a decrease of the a axis [46].

Table 3.VI. Crystallographic analysis of the as-obtained new phases.

<i>Sample</i>	a (Å)	c (Å)	c/a	<i>Cell Vol.</i> (Å ³)	D_{av} (nm)	D_{300} (nm)	D_{002} (nm)	$D_{002}/$ D_{300}	<i>C.I.</i>
HA	9.432 (1)	6.895 (1)	0.731 (1)	531.2 ±0.1	21.3 ±2.1	22.8 ±0.4	56.0 ±1.5	2.46	3.68
Zn-HA-1	9.423 (5)	6.887 (4)	0.730 (9)	529.7 ±0.2	15.4 ±1.2	16.7 ±0.8	31.2 ±0.9	1.87	3.81
Zn-HA-2	9.453 (9)	6.885 (5)	0.728 (3)	532.9 ±0.1	13.1 ±1.7	16.7 ±1.0	31.7 ±0.8	1.90	3.58
Zn-CHA-1	9.416 (3)	6.899 (0)	0.732 (7)	529.7±0. 1	15.0 ±1.1	17.9 ±0.9	29.0 ±0.7	1.62	3.38
Zn-MCHA-1	9.417 (4)	6.888 (9)	0.731 (5)	529.1 ±0.1	13.7 ±1.1	17.1 ±0.8	29.9 ±0.7	1.75	3.07
Zn-MCHA-2	9.422 (4)	6.883 (1)	0.730 (5)	529.2 ±0.2	10.8 ±1.3	17.1 ±0.8	29.9 ±0.7	1.79	3.15
Zn-MCHA-3	9.402 (0)	6.891 (1)	0.732 (9)	527.5 ±0.1	18.4 ±1.3	22.7 ±1.0	38.3 ±0.9	1.69	3.41
Zn-MCHA-4	9.400 (5)	6.893 (6)	0.733 (3)	527.6 ±0.1	14.3 ±1.1	20.2 ±0.9	32.2 ±0.8	1.59	3.02
Zn-MCHA-5	9.378 (6)	6.880 (5)	0.733 (6)	524.1 ±0.2	11.6 ±1.6	18.2 ±1.1	25.6 ±0.8	1.41	3.13

By separate evaluation of the domain size along the two orthogonal axes of the hexagonal HA lattice, it was found that all the HA phases showed anisotropic crystal development along the c axis. However, crystal anisotropy tended to decrease in substituted HAs and even more markedly in the multi-substituted materials (**Table 3.VI.**).

FTIR spectra collected on the new doped apatites (**Figure 3.14.**) showed the characteristic absorption bands of phosphate group at 980–1100 and 560–600 cm^{-1} . As the water adsorbed on the powdered samples was eliminated by heating prior to FTIR spectra acquisition, the broad bands at $\sim 3500 \text{ cm}^{-1}$ and at 1640 cm^{-1} only addressed the presence of structural water into the HA structure [47]. The FTIR absorption bands appear weakly resolved, particularly in **Figure 3.14.c.**, as confirmed by the splitting factors reported in **Table 3.VI.** FTIR analysis reported also the presence of carbonate in the doped apatitic phases, particularly with the absorption bands at ~ 1450 , 1430 and 870 cm^{-1} [31], confirming that the carbonate group substituted the phosphate group (B-type substitution) in all the new phases (see **Figure 3.14.**).

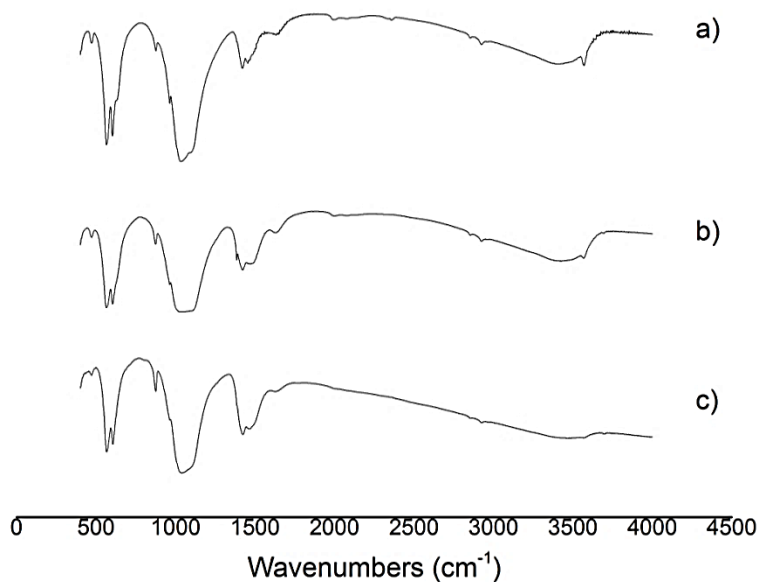


Figure 3.14. FTIR spectra of some different substituted hydroxyapatites. a) HA, b) Zn-HA-1, c) Zn-MCHA-5

FTIR spectra also highlighted the reduction of the OH^- absorption peak at 3570 cm^{-1} in the monosubstituted and, in higher extent, in the multisubstituted phase (similar amount of Zinc but also containing Mg and CO_3), if compared to undoped HA. Also, an increase of the carbonation extent in multi-doped phases with the increase of Zinc content was detected (**Table 3.VII.**). A possible mechanism to explain the decrease of the oxidrile peak is the charge compensation for the carbonate uptake in substitution of a phosphate group, resulting in a lack of a negative charge. This charge could be balanced by the contemporaneous discharge of a Ca^{2+} and of an OH^- [48]. Both Zn-HA and Zn-MCHA have an enhanced carbonation. The enhanced carbonation detected in the multi-substituted Zn-MCHA apatites (**Table 3.VII.**), could be explained by the claimed ability of magnesium to favor the CO_3^{2-} uptake in HA [49]. In the multisubstituted Zn-MCHA powders it is also possible to see a linear increment of carbonate content in function of X_{Zn} , comparing Zn-MCHA-1/2/4, that has the same initial X_{Mg} , as shown in **Figure 3.15.** Contrarily the enhanced carbonation in the monosubstituted phases, that increase linearly at the augment of Zn content (**Table 3.VII.**, **Figure 3.15.**), could only be explained by a similar ability of Zn. In **Figure 3.15.**

It is possible to see two different lines, one for Zn-HA and one for Zn-MCHA. The slope of the Zn-HA line is due only to the effect of Zn while the slope of the Zn-MCHA line is due to the simultaneous effect of zinc, magnesium and dropping of carbonate.

The chemical analysis of the as-obtained powders, reported in **Table 3.VII.**, shown that Zn is really found in the final apatite but only a fraction of zinc nominally introduced in the reaction vessel remained incorporated in the apatite structure.

Table 3.VII. Chemical analysis of the as-obtained new phases.

<i>Samples</i>	<i>Molar Ca/P</i>	<i>Actual X_{Mg}</i>	<i>Initial X_{Mg}</i>	<i>% Mg remained</i>	<i>Actual X_{Zn}</i>	<i>Initial X_{Zn}</i>	<i>% Zn remained</i>	<i>Actual</i>
HA	1.69	---	---	---	---	0.00	---	0
Zn-HA-1	1.69	---	---	---	0.049	0.05	98	0
Zn-HA-2	1.51	---	---	---	0.093	0.10	93	0
Zn-CHA-1	1.67	---	---	---	0.049	0.05	98	0
Zn-MCHA-1	1.67	0.053	0.10	53	0.011	0.015	73	0
Zn-MCHA-2	1.67	0.053	0.10	52	0.021	0.03	70	0
Zn-MCHA-3	1.67	0.026	0.05	52	0.038	0.05	77	0
Zn-MCHA-4	1.67	0.048	0.10	48	0.040	0.05	79	0
Zn-MCHA-5	1.67	0.071	0.15	47	0.040	0.05	80	0

Considering only mono-substituted Zn-HA an average yield of Zn incorporation of $95.5 \pm 3.5\%$ is reached. It is an optimal degree of incorporation, that is probably due to the high affinity of Zinc for the apatitic phase. Considering instead material co-doped with Zn and CO₃ ions, the degree of incorporation raised to 98%. It is not a significant result, because it is only one sample and is included in the error, but could reveal a higher affinity of Zn for carbonated-HA. The affinity of Zn for carbonated apatite is also evidenced in the augment of carbonation in Zn-MCHA at the augment of Zn content. Considering instead multi-substituted Zn-MCHA, the materials co-doped with Zn, Mg and CO₃ ions, the average yield of Zn incorporation falls down to $75.8 \pm 4.1\%$. This data is very far from the almost total incorporation of Zn into the mono-substituted apatitic phase or into the double substituted phase. This finding could reveal a

competition for the same crystallographic site between Zn and Mg. The reduction of Zn incorporation yield is not dose dependent on Mg quantity as revealed by the degree of incorporation for Zn-MCHA-3-4-5, with the same X_{Zn} but different X_{Mg} . These three phases have the same Zn incorporation yield ($78.8 \pm 2.7\%$). For Zn-MCHA-1-2-5, samples with the same initial X_{Mg} but with different X_{Zn} it is possible to consider the degree of incorporation of Mg in presence of Zinc. The degree of incorporation of Mg decrease almost linearly at the augment of zinc content. These data confirm a competitiveness between Zn and Mg. However Zn has a higher affinity than Mg for the apatitic phase, as demonstrated by the different degree of incorporation (75% for Zn compared with 50% for Mg).

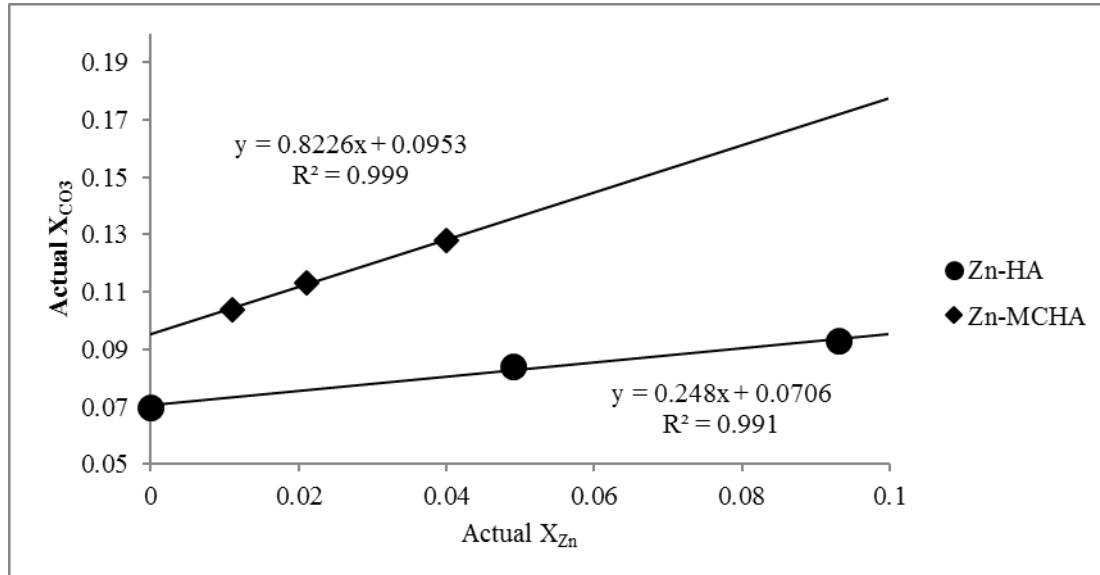


Figure 3.15. Carbonate content in function of the actual Zn content in mono- and multi-substituted phases

3.3.3. Ion release test

To conclude the characterization of the new obtained phases and investigate the potential bioactivity and antibacterial effect of the Zn apatitic phases, the release of ions in simulated physiological fluid was recorded for Zn-HA-1, Zn-HA-2 and Zn-MCHA-5 in comparison with the non-substituted HA taken as a reference.

Those phases were selected to evidence the dose dependency of Zn in two different mono substituted phase and the comparison between a Zn monosubstituted and a Zn-Mg-CO₃ multisubstituted phase with the same Zn content to evaluate the synergistic effect of Mg and carbonate.

A first remarkable effect of ions release tests is the absence of Zn release, despite it was searched. It was confirmed that Zn has high affinity for entering into the apatitic lattice in a stable form so that it was not released in solution at a neutral pH. The release profiles of Ca and Mg, in all the investigated materials, can be described as the summation of two different trends, due to two different release mechanisms . A first predominant effect is a burst ion release, particularly relevant in the first 3 days, followed by a secondary slower release profile. (**Figure 3.16.** and **Figure 3.17.**) The burst release of the first 3 days could be explained by the release of ions from the superficial and less ordered layer of the crystal, that are more soluble while the second slower profile is probably due to the dissolution of the crystals.

The calcium release rate increased steadily with calcium content in Zn-doped apatites but, unexpectedly, decreased in multi-doped materials. This effect could be due to the concomitant easiest release of Mg, 10% in the first 3 days, 15% overall. This release of cations inhibits the release of higher amount of calcium, to avoid the creation of a lack of positive charge inside the lattice.

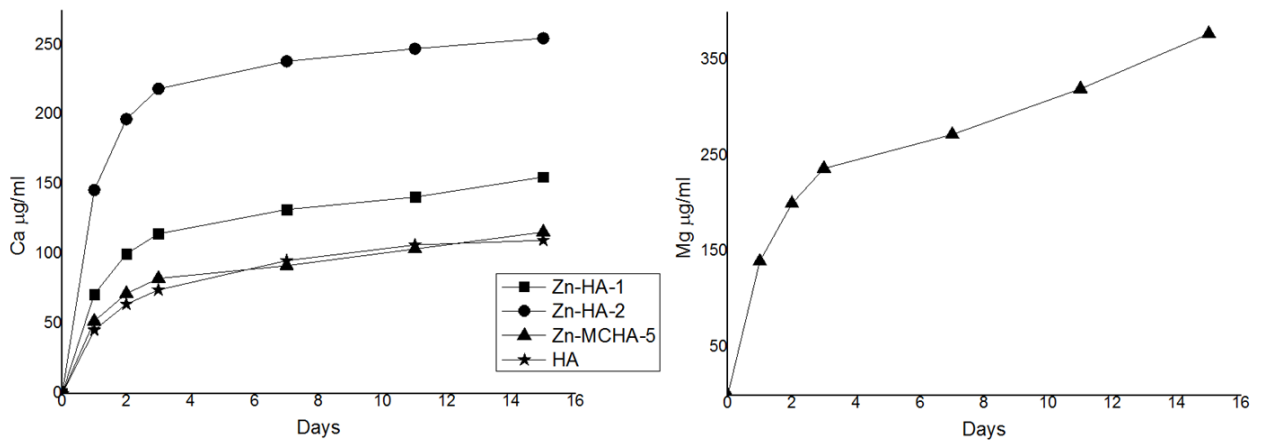


Figure 3.16. Ion release tests for all the selected composition. The results are expressed as absolute concentrations.

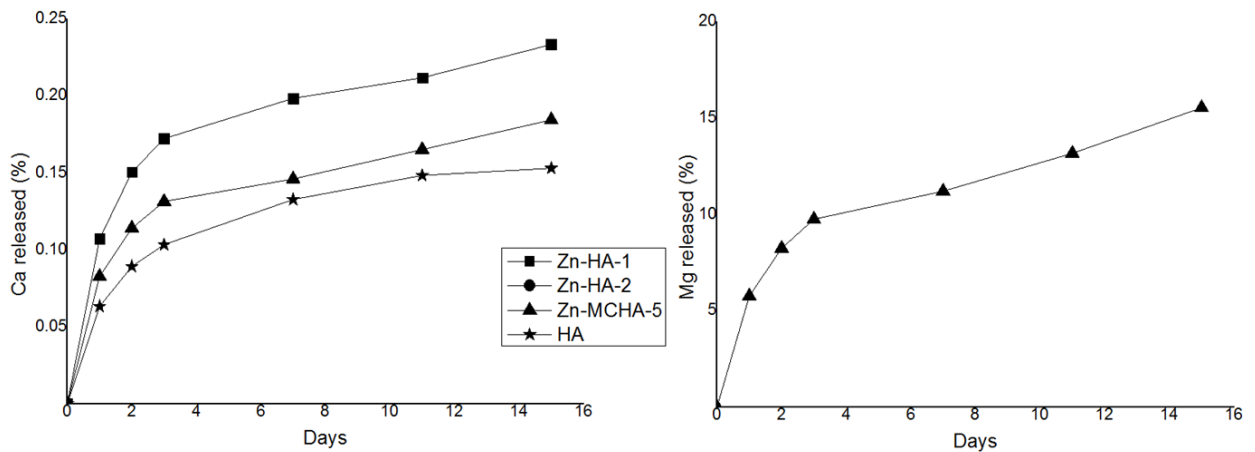


Figure 3.17. Ion release tests for all the selected composition. The results are showed as percentage ion loss in respect to the starting material.

3.3.4. Biological characterization

In vitro cell analysis was carried out on three selected materials: Zn-HA-1, coded for biological tests as ZnHA, Zn-MCHA-5, coded for biological tests as ZnMgHA and the undoped HA, as a reference. The ACSs behavior in contact with two different concentrations of powders was investigated *in vitro* looking at the cell viability, cell morphology and cell differentiation up to 14 days of culture. The quantification of metabolically active cells showed a significant

enhancement in cell proliferation induced by the presence of Zn. This effect seems to be dose dependent, in fact, a significant difference was observed early (day 7) in the cells cultured in presence of 500 $\mu\text{g/ml}$ whether in presence of 50 $\mu\text{g/ml}$ the induction of proliferation is evident at day 14 (**Fig. 3.7**).

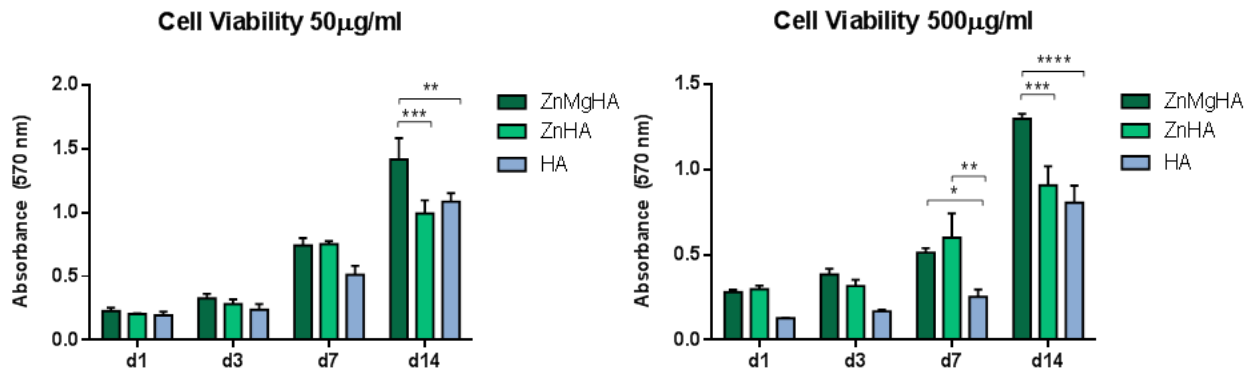


Figure 3.18. Analysis of cells proliferation by MTT assay, after 1, 3, 7 and 14 days of ASCs seeded with 50 $\mu\text{g/ml}$ and 500 $\mu\text{g/ml}$ of the new phases. * $p \leq 0.05$; **** $p \leq 0.0001$. $n = 3$.

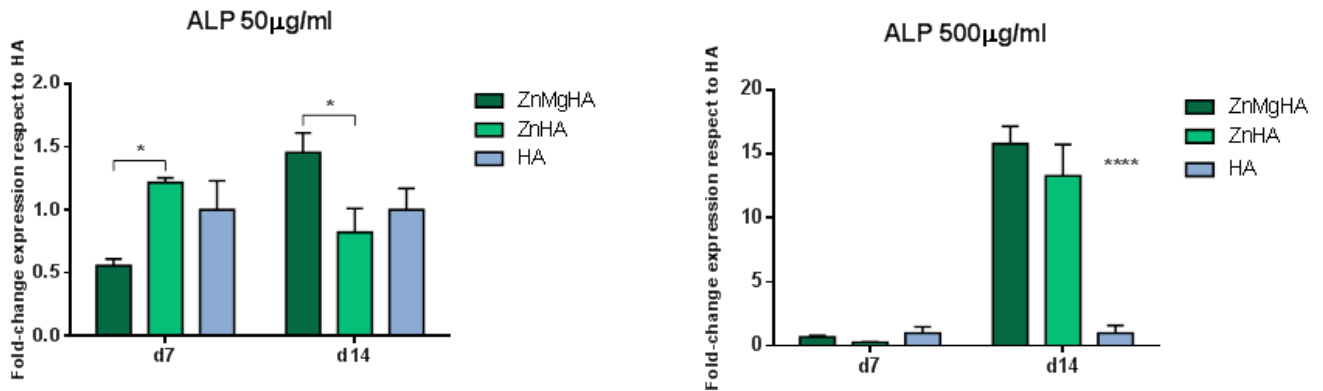


Figure. 3.19: ALPL gene expression analysis. Relative quantification ($2^{-\Delta\Delta\text{Ct}}$) of gene expression after 7 and 14 days of ASCs cultured in contact with all the samples. Mean and standard error of the technical triplicate of ALPL, with respect to the expression of cells in contact with HA, used as control. (* $p \leq 0.05$; ** $p \leq 0.01$).

In order to assess any osteoinductive effect of the new phases on ACS differentiation, gene expression analysis of ALPL was evaluated by qPCR, and RUNX2 and COL-I proteins were qualitative detected by immunofluorescent analysis. The results showed that ALP was significantly up regulated by the presence of the highest concentration of ZnMgHA only at day

14 with respect to Zn-HA (* $p \leq 0.05$) and HA (* $p \leq 0.05$) used as control group (**Figure 3.19.**) for 50 μ g/l. The results for 500 μ g/l showed instead that ALPL was significantly up regulated by the presence of both the concentration of Zn after 14 days of culture (**Figure 3.19.**).

3.3.5. Antibacterial test

The new phases already tested for ion release (HA, Zn-HA-1, Zn-HA-2, Zn-MCHA-5) were tested also for antibacterial activity. The antibacterial effect of the new phases was tested with 4 different bacterial strains and yeast (*Pseudomonas Aeruginosa*, *Escherichia Coli*, *Staphylococcus Aureus* and *Candida Albicans*, respectively two gram-, one gram+ and a yeast). The antibacterial tests were carried out on two different sets of materials: the first set (coded as NON-COND) was used as synthesized; a second set (coded as COND) was used after conditioning by soaking into pH=7.4 buffer solution (Ca and Mg free Hank's Balanced Salt solution) for 15 days, i.e. in the same experimental conditions used for the analysis of ion release. The results of the bacterial reduction are showed in **Figures 3.20.** and **Figure 3.21.**, for NON-COND and COND sets of samples, respectively. All NON-COND samples showed ability of bacterial reduction higher than 85% after 24 hours. Also, the analysis of NON-COND samples evidenced a higher antibacterial activity in the Zn-substituted apatites, in respect to the undoped HA. Moreover the antibacterial effect was reached more rapidly in doped and, particularly, in multi-doped materials, particularly for *E. Coli* and *C. Albicans*.

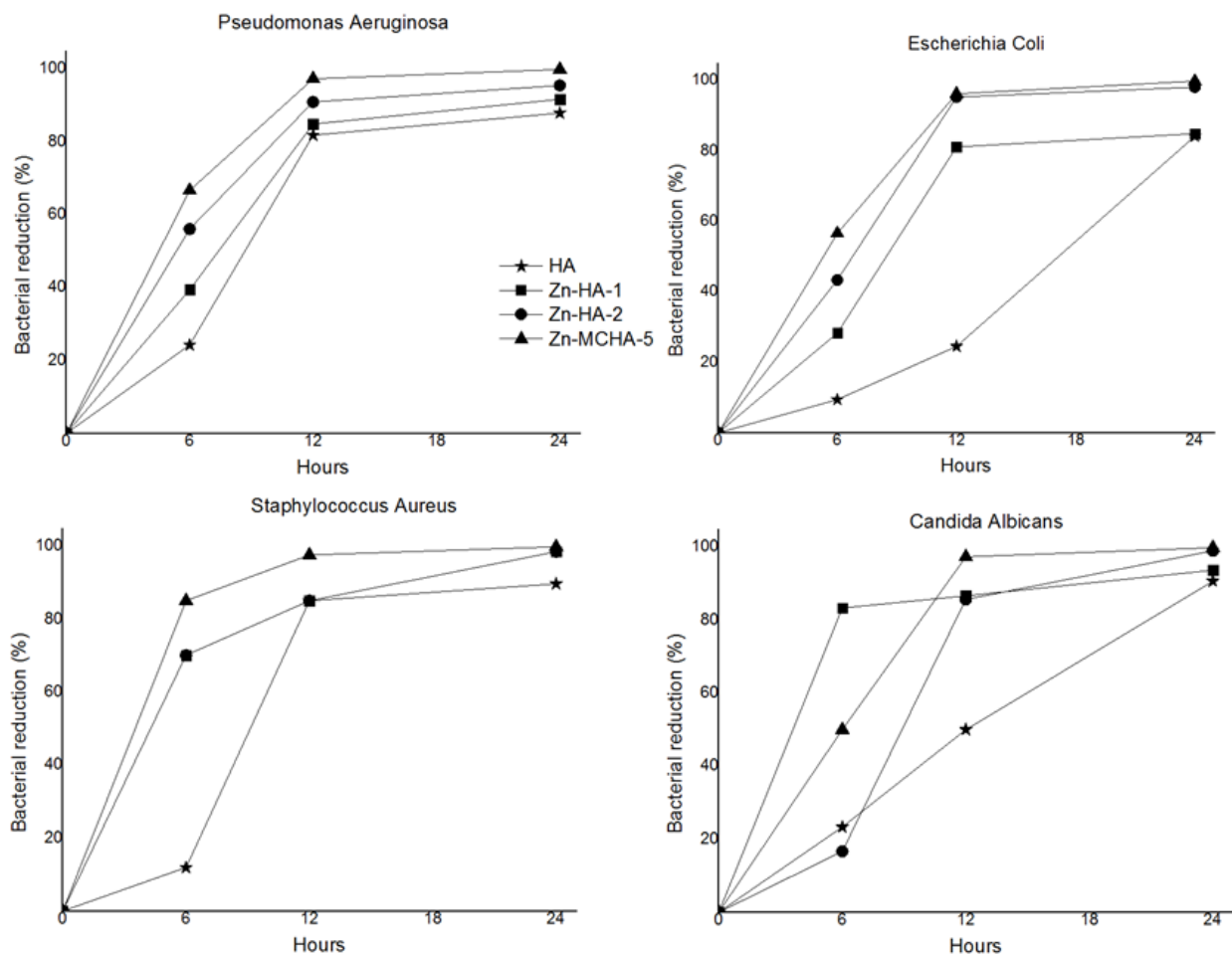


Figure 3.20. Bacterial reduction for all the bacterial strains and all the compositions tested (NON-COND).

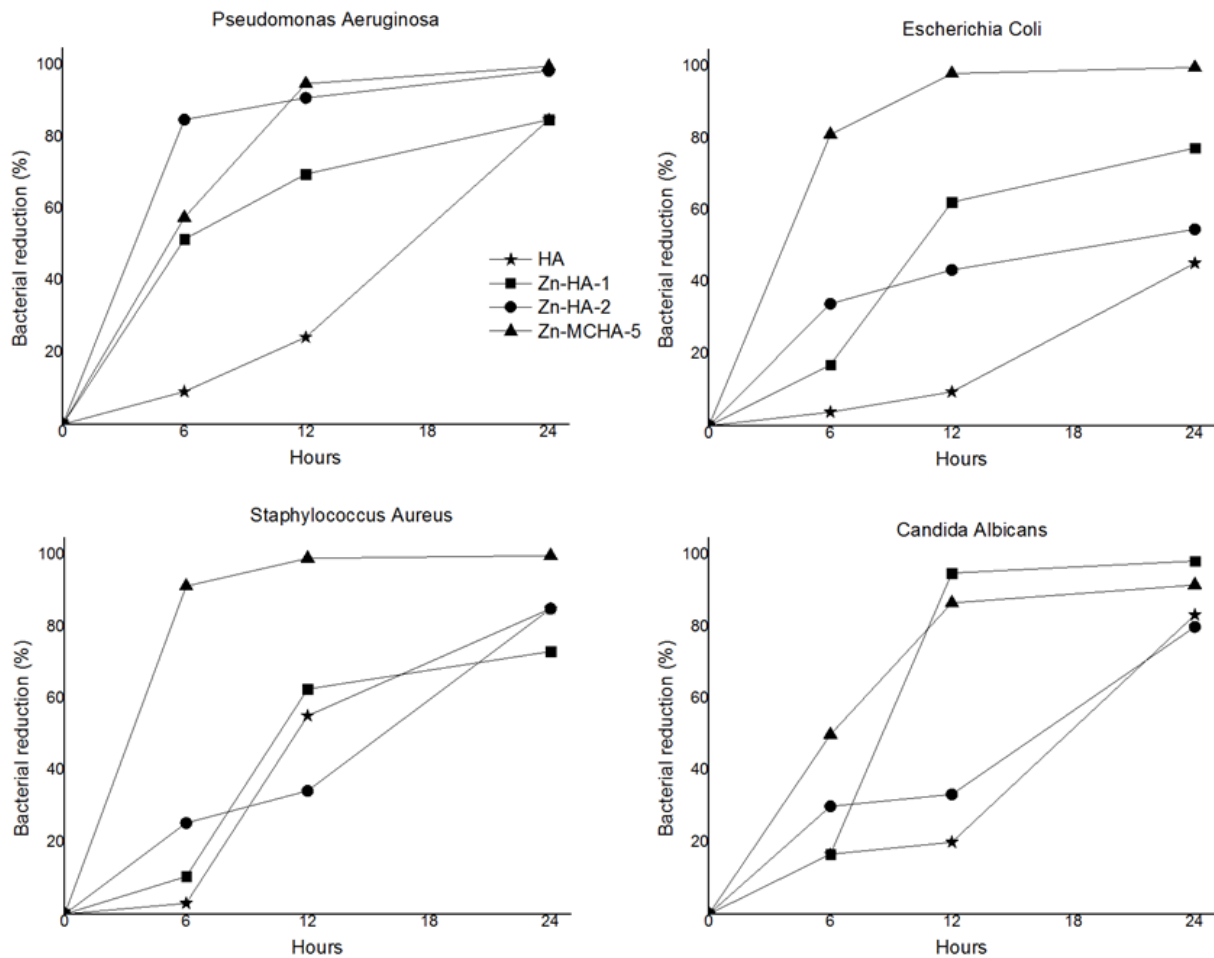


Figure 3.21. Bacterial reduction for all the bacterial strains and all the compositions tested (COND).

The analysis of the COND samples evidenced a great difference between Zn-MCHA and the other phases. For the other phases was seen an extensive reduction of the antibacterial activity while for Zn-MCHA the activity remain at the same level of the NON-COND samples. A possible explanation of this effect could be researched by comparison with the release tests. It is possible to notice that for Zn-MCHA the release of Mg continues slowly also after 15 days, so the apatite could be considered still active. In all the groups the undoped HA was confirmed as the less effective agent against bacterial proliferation, for all the considered strands.

3.3.6. Discussion

New ion-substituted nanocrystalline apatites were synthesized by direct introduction of zinc and other foreign ions into the apatite crystal during its formation in aqueous medium. The evidence of a direct relationship between the initial amount of zinc and the extent of incorporation in the structure of the final apatite (see ICP analysis in **Table 3.VII.**) opens to the possibility to obtain Zn-doped apatites as pure nanocrystalline phases with designed ion content (See **Figure 3.12.**, **Table 3.VI**, and **Table 3.VII.**). The effective entering of zinc is also confirmed by changing of the lattice parameters, the reduction of OH⁻ groups and the increase of spontaneous carbonation (see **Figure 3.14.**, **Table 3.VI.** and **Table 3.VII.**), as an effect for balancing the lattice distortion. These results confirm the ability of the apatite structure to easily accommodate the introduction of foreign ions.

In the case of multiple substitution with also Mg and CO₃, various effects on the HA crystal development co-existed. A linear correlation between the Mg incorporation reduction and the presence of zinc was found. Zinc incorporation yield is also correlated to Mg presence, but without dose dependency (see **Table 3.VI.**). This effect could be explained by a competition between the two ions for the same crystallographic site. In this competition Zn was favored against Mg. In respect to single-substituted Zn-HAs, the introduction of additional Mg²⁺ and CO₃²⁻ ions provoked a reduction of the apatite lattice volume and also a marked decrease of average crystallite dimension.

It is also possible that part of Mg ions could be segregated in the disordered layer typically present in low crystallinity apatites [35], rather than being included in the HA lattice. This hypothesis is supported by the much higher release of Mg in the first days immersion (**Figure 3.16.** and **Figure 3.17.**). Contrarily zinc ions were never been released in solution. This effect

could be explained by a strong bond between Zn ions and the apatite lattice.

The incorporation of at least a fraction of calcium and magnesium ions into the disordered non-apatitic layer in all doped HAs can also explain the two-stage release kinetics recorded during the test (**Figure 3.16.** and **Figure 3.17.**). In this respect, the early stage of release could involve mainly those ions included in the superficial non-apatitic layers surrounding the more crystalline cores. A subsequent stage of release, characterized by a less steep straight line, could be referred to a continuous release of ions, particularly Mg, from an inner and more crystalline layers [50]. Apatite carbonation in B position is a relevant phenomenon for biological purposes, as it confers enhanced solubility *in vivo* and affinity with cells [36]. It can spontaneously occur during the HA synthesis, as carbon dioxide present in the air atmosphere can dissolve in the alkaline suspension where the HA phase nucleates and mature, or by direct introduction of carbonate ions. The ICP and TG analyses in **Table 3.VI.** showed that the presence of zinc favored the spontaneous apatite carbonation, and the simultaneous substitution of Mg and the appositely introduction of carbonate ions magnify this effect (**Figure 3.15.**).

In respect to stoichiometric, undoped apatite, the higher solubility and the presence of multiple ions in the apatite structure can represent a source of signals for cells in assistance to the bone regenerative cascade. Recently mesenchymal stem cells have attracted a lot of attention for therapeutic uses due to the great ability to differentiate into cellular phenotypes of several tissues including cartilage, bone, muscle, nervous system, and they also regulate the innate immune system. In this view adipose tissue represents an abundant and accessible source of adult stem cells with the ability to differentiate in bone cells (i.e. osteoblasts). Focusing on a synergistic use of biomaterial and cellular therapy in certain orthopedic disorders (e.g. osteoporosis, Paget's disease), a pilot *in vitro* study was performed to evaluate for the first time the ACSs behavior in

response to the new multi-substituted apatite phases, subject of the present study. Our results showed that Zn-doped HAs cell viability was enhanced at the presence of Zn, also in case of low concentration of the material for Zn-MCHA-5, and the up regulation of ALPL, osteo-related gene, were significantly enhanced both in the mono-doped and multi-doped material.

Despite their positive effect on human adipose mesenchymal stem cells, all the tested apatites showed a remarkable bactericidal effect, particularly enhanced in the new multi-substituted apatites (**Figure 3.20.** and **Figure 3.21.**), on four major post-surgery infective lines, including three different types of infective agents: gram positive, gram negative and yeast. The comparison between the two COND and NON-COND sample series highlighted that undoped HA was the material with lower antibacterial effect in all cases; also, in respect to non-conditioned samples a retard in the bacterial reduction effect for conditioned materials was detected and, particularly for *E. Coli* and *C. Albicans*, a reduced antibacterial effect after 24 hours. Particularly relevant is the antibacterial effect of Zn-MCHA COND that, after 15 days of release, does not vary its antibacterial effect, that remains, for all the bacterial strains, over 95%. This finding suggests that for Zn-MCHA the intensive ion release occurring during the first day is not the driving force of the antibacterial effect, as suggested by data showed in **Figures 3.5 and 3.6.** This suggests the activation of a remarkable effect of antibacterial activity through the direct interaction between bacteria and the solid material in Zn-MCHA COND sample. These preliminary results, however, encourage to investigate Zn-Mg-CO₃-doped apatites as a new system with prolonged antibacterial effect. Indeed, substituted apatite phases have been widely developed in previous research, with the purpose to mimic the inorganic part of bone; however, the present study shows that ion-substituted apatites can display additional antibacterial functionality that can be exalted in presence of multi-substitution. This effect could be exploited for the production of bone implants

or of coating for prostheses, thus being able to promote and sustain new bone formation and, at the same time, to lower the occurrence of infections and biofilm formation at the interface between the implant and the native bone with a prolonged antibacterial effect, thanks to the steady and progressive release of active ions, like Mg and carbonate. These two factors can significantly improve the bone healing process in a number of clinical cases, with positive impact on the health and wellness of the population. In particular, the outcomes of the *in vitro* tests, along with the well-known HA effect on several genes involved in osteogenesis demonstrate the promising features of these multi-substituted apatites in bone homeostasis regulation in degenerative diseases like osteoporosis or Paget's disease.

3.3.7. Conclusion

The steady increase of disabling bone diseases requires effective and durable therapies for effective tissue healing and, also, to prevent undesired secondary effects jeopardizing or retarding the healing process. In this respect, the novel multi-doped apatites developed in this work are promising as cell-instructive biomaterials with double functionality of enhanced osteogenic and antibacterial effect, in comparison with undoped and single-doped apatites. Particularly, the doping with zinc was effective in inducing antibacterial effect against some bacterial strands, without reducing the viability of human cells. However, apatites multi-doped with magnesium and carbonate demonstrated enhanced effects, in respect to the expression of genes relevant for the regenerative cascade and of prolonged antibacterial activity without sensible reduction.

These results show, for the first time, that zinc, magnesium and carbonate can be incorporated simultaneously in designed amounts, in the structure of nanocrystalline apatites, as effective antibacterial agent. In addition, the present work confirmed the relevant role of magnesium and

carbonate multi-substitution in the bone regeneration process and evidence their effect also as antibacterial agents. So that the association of such key properties makes the multi-doped apatites developed in this work as novel multi-functional materials for the preparation of advanced scaffolds or coatings for bone implants.

3.4. References

- [1] Palmer LC, Newcomb CJ, Kaltz SR, Spoerke ED, Stupp SI. Biomimetic systems for hydroxyapatite mineralization inspired by bone and enamel. *Chemical reviews* 2008;108:4754-83.
- [2] Kane R, Ma PX. Mimicking the nanostructure of bone matrix to regenerate bone. *Materials today* 2013;16:418-23.
- [3] Song Z, Borgwardt L, Hoiby N, Wu H, Sorensen TS, Borgwardt A. Prosthesis infections after orthopedic joint replacement: the possible role of bacterial biofilms. *Orthopedic reviews* 2013;5:65-71.
- [4] Parent M, Magnaudeix A, Delebasse S, Sarre E, Champion E, Viana Trecant M, et al. Hydroxyapatite microporous bioceramics as vancomycin reservoir: Antibacterial efficiency and biocompatibility investigation. *Journal of biomaterials applications* 2016;31:488-98.
- [5] Yazdi M, Bernick S, Paule WJ, Nimni ME. Postmortem degradation of demineralized bone matrix osteoinductive potential. Effect of time and storage temperature. *Clinical orthopaedics and related research* 1991:281-5.
- [6] Li SH, De Wijn JR, Layrolle P, de Groot K. Synthesis of macroporous hydroxyapatite scaffolds for bone tissue engineering. *Journal of biomedical materials research* 2002;61:109-20.
- [7] Allegrini S, Jr., Rumpel E, Kauschke E, Fanghanel J, Konig B, Jr. Hydroxyapatite grafting promotes new bone formation and osseointegration of smooth titanium implants. *Annals of anatomy = Anatomischer Anzeiger : official organ of the Anatomische Gesellschaft* 2006;188:143-51.

- [8] Gibson IR, Bonfield W. Preparation and characterization of magnesium/carbonate co-substituted hydroxyapatites. *Journal of materials science Materials in medicine* 2002;13:685-93.
- [9] Landi E, Logroscino G, Proietti L, Tampieri A, Sandri M, Sprio S. Biomimetic Mg-substituted hydroxyapatite: from synthesis to in vivo behaviour. *Journal of materials science Materials in medicine* 2008;19:239-47.
- [10] Young RA. Biological apatite vs hydroxyapatite at the atomic level. *Clinical orthopaedics and related research* 1975:249-62.
- [11] Holmes RE, Bucholz RW, Mooney V. Porous hydroxyapatite as a bone graft substitute in diaphyseal defects: a histometric study. *Journal of orthopaedic research : official publication of the Orthopaedic Research Society* 1987;5:114-21.
- [12] Zhou H, Lee J. Nanoscale hydroxyapatite particles for bone tissue engineering. *Acta biomaterialia* 2011;7:2769-81.
- [13] Swetha M, Sahithi K, Moorthi A, Saranya N, Saravanan S, Ramasamy K, et al. Synthesis, characterization, and antimicrobial activity of nano-hydroxyapatite-zinc for bone tissue engineering applications. *Journal of nanoscience and nanotechnology* 2012;12:167-72.
- [14] Kolmas J, Groszyk E, Kwiatkowska-Rozycka D. Substituted hydroxyapatites with antibacterial properties. *BioMed research international* 2014;2014:178123.
- [15] Rameshbabu N, Sampath Kumar TS, Prabhakar TG, Sastry VS, Murty KV, Prasad Rao K. Antibacterial nanosized silver substituted hydroxyapatite: synthesis and characterization. *Journal of biomedical materials research Part A* 2007;80:581-91.
- [16] Bernstein LR. Mechanisms of therapeutic activity for gallium. *Pharmacological reviews* 1998;50:665-82.

- [17] Bai X, Sandukas S, Appleford M, Ong JL, Rabiei A. Antibacterial effect and cytotoxicity of Ag-doped functionally graded hydroxyapatite coatings. *Journal of biomedical materials research Part B, Applied biomaterials* 2012;100:553-61.
- [18] Thian ES, Konishi T, Kawanobe Y, Lim PN, Choong C, Ho B, et al. Zinc-substituted hydroxyapatite: a biomaterial with enhanced bioactivity and antibacterial properties. *Journal of materials science Materials in medicine* 2013;24:437-45.
- [19] Ito A, Ojima K, Naito H, Ichinose N, Tateishi T. Preparation, solubility, and cytocompatibility of zinc-releasing calcium phosphate ceramics. *Journal of biomedical materials research* 2000;50:178-83.
- [20] Kurtjak M, Vukomanovic M, Kramer L, Suvorov D. Biocompatible nano-gallium/hydroxyapatite nanocomposite with antimicrobial activity. *Journal of materials science Materials in medicine* 2016;27:170.
- [21] Darouiche RO. Treatment of infections associated with surgical implants. *The New England journal of medicine* 2004;350:1422-9.
- [22] Landi E, Sprio S, Sandri M, Celotti G, Tampieri A. Development of Sr and CO₃ co-substituted hydroxyapatites for biomedical applications. *Acta biomaterialia* 2008;4:656-63.
- [23] Melnikov P, Teixeira AR, Malzac A, Coelho MdB. Gallium-containing hydroxyapatite for potential use in orthopedics. *Mater Chem Phys* 2009;117:86-90.
- [24] Bertoni E, Bigi A, Cojazzi G, Gandolfi M, Panzavolta S, Roveri N. Nanocrystals of magnesium and fluoride substituted hydroxyapatite. *J Inorg Biochem* 1998;72:29-35.
- [25] Bigi A, Boanini E, Capuccini C, Gazzano M. Strontium-substituted hydroxyapatite nanocrystals. *Inorg Chim Acta* 2007;360:1009-16.

- [26] Yin ZL, Wang XY, Wang XH, Zhang N, Chen L, Qu HY, et al. Facile Synthesis of Element-Substituted Hydroxyapatite Whiskers Using β -Tricalcium Phosphate as Precursors. *Int J Appl Ceram Tec* 2015;12:1000-7.
- [27] Iafisco M, Ruffini A, Adamiano A, Sprio S, Tampieri A. Biomimetic magnesium-carbonate-apatite nanocrystals endowed with strontium ions as anti-osteoporotic trigger. *Mat Sci Eng C-Mater* 2014;35:212-9.
- [28] Pathi SP, Lin DD, Dorvee JR, Estroff LA, Fischbach C. Hydroxyapatite nanoparticle-containing scaffolds for the study of breast cancer bone metastasis. *Biomaterials* 2011;32:5112-22.
- [29] Tampieri A, Celotti G, Landi E, Sandri M. Magnesium doped hydroxyapatite: Synthesis and characterization. *Euro Ceramics VIII, Pts 1-3* 2004;264-268:2051-4.
- [30] Landi E, Tampieri A, Celotti G, Vichi L, Sandri M. Influence of synthesis and sintering parameters on the characteristics of carbonate apatite. *Biomaterials* 2004;25:1763-70.
- [31] Landi E, Celotti G, Logroscino G, Tampieri A. Carbonated hydroxyapatite as bone substitute. *Journal of the European Ceramic Society* 2003;23:2931-7.
- [32] Sprio S, Tampieri A, Landi E, Sandri M, Martorana S, Celotti G, et al. Physico-chemical properties and solubility behaviour of multi-substituted hydroxyapatite powders containing silicon. *Mat Sci Eng C-Bio S* 2008;28:179-87.
- [33] Gibson IR, Bonfield W. Preparation and characterization of magnesium/carbonate co-substituted hydroxyapatites. *J Mater Sci-Mater M* 2002;13:685-93.
- [34] Landi E, Tampieri A, Mattioli-Belmonte M, Celotti G, Sandri M, Gigante A, et al. Biomimetic Mg- and Mg,CO₃-substituted hydroxyapatites: synthesis characterization and in vitro behaviour. *J Eur Ceram Soc* 2006;26:2593-601.

- [35] Cazalbou S, Combes C, Eichert D, Rey C, Glimcher MJ. Poorly crystalline apatites: evolution and maturation in vitro and in vivo. *J Bone Miner Metab* 2004;22:310-7.
- [36] Rey C, Renugopalakrishnan V, Collins B, Glimcher MJ. Fourier-Transform Infrared Spectroscopic Study of the Carbonate Ions in Bone-Mineral during Aging. *Calcified Tissue Int* 1991;49:251-8.
- [37] de Girolamo L, Sartori MF, Albisetti W, Brini AT. Osteogenic differentiation of human adipose-derived stem cells: comparison of two different inductive media. *Journal of tissue engineering and regenerative medicine* 2007;1:154-7.
- [38] Gimble JM, Katz AJ, Bunnell BA. Adipose-derived stem cells for regenerative medicine. *Circ Res* 2007;100:1249-60.
- [39] Panseri S, Montesi M, Iafisco M, Adamiano A, Ghetti M, Cenacchi G, et al. Magnetic Labelling of Mesenchymal Stem Cells with Iron-Doped Hydroxyapatite Nanoparticles as Tool for Cell Therapy. *Journal of biomedical nanotechnology* 2016;12:909-21.
- [40] Montesi M, Panseri S, Iafisco M, Adamiano A, Tampieri A. Effect of hydroxyapatite nanocrystals functionalized with lactoferrin in osteogenic differentiation of mesenchymal stem cells. *Journal of biomedical materials research Part A* 2015;103:224-34.
- [41] Suto M, Nemoto E, Kanaya S, Suzuki R, Tsuchiya M, Shimauchi H. Nanohydroxyapatite increases BMP-2 expression via a p38 MAP kinase dependent pathway in periodontal ligament cells. *Archives of oral biology* 2013;58:1021-8.
- [42] Bockman R. The effects of gallium nitrate on bone resorption. *Seminars in oncology* 2003;30:5-12.
- [43] Chitambar CR. Medical Applications and Toxicities of Gallium Compounds. *International journal of environmental research and public health* 2010;7:2337-61.

- [44] Kawamura H, Ito A, Miyakawa S, Layrolle P, Ojima K, Ichinose N, et al. Stimulatory effect of zinc-releasing calcium phosphate implant on bone formation in rabbit femora. *J Biomed Mater Res* 2000;50:184-90.
- [45] Thian ES, Konishi T, Kawanobe Y, Lim PN, Choong C, Ho B, et al. Zinc-substituted hydroxyapatite: a biomaterial with enhanced bioactivity and antibacterial properties. *J Mater Sci-Mater M* 2013;24:437-45.
- [46] Bigi A, Falini G, Foresti E, Ripamonti A, Gazzano M, Roveri N. Magnesium influence on hydroxyapatite crystallization. *Journal of Inorganic Biochemistry* 1993;49:69-78.
- [47] Yoder CH, Pasteris JD, Worcester KN, Schermerhorn DV. Structural water in carbonated hydroxylapatite and fluorapatite: Confirmation by solid state ^2H NMR. *Calcified Tissue International* 2012;90:60-7.
- [48] Ivanova T, Frank-Kamenetskaya O, Kol'tsov A, Ugolkov V. Crystal structure of calcium-deficient carbonated hydroxyapatite. Thermal decomposition. *Journal of Solid State Chemistry* 2001;160:340-9.
- [49] Campbell AA, LoRe M, Nancollas GH. The influence of carbonate and magnesium ions on the growth of hydroxyapatite, carbonated apatite and human powdered enamel. *Colloids and surfaces* 1991;54:25-31.
- [50] Rey C, Renugopalakrishnan V, Shimizu M, Collins B, Glimcher MJ. A Resolution-Enhanced Fourier-Transform Infrared Spectroscopic Study of the Environment of the $\text{Co}_3(2-)$ Ion in the Mineral Phase of Enamel during Its Formation and Maturation. *Calcified Tissue Int* 1991;49:259-68.

4. STRONTIUM SUBSTITUTED HYDROXYAPATITE AS COATINGS FOR POLY ETHER ETHER KETONE (PEEK)

4.1. Introduction

The application of bone implants in osteoporotic patients remains a clinical challenge in orthopedic surgery because this condition hampers primary stability, biological fixation and ultimately osseointegration [1]. Sr^{2+} is known in literature as a doping ion for calcium phosphates (CaP) because its osteogenic effect at low doses inhibits bone resorption and improves bone formation which is promising for the treatment of osteoporotic patients [2]. The therapeutic efficacy of Sr^{2+} ions has been reported extensively [2] and administration of Sr-ranelate has been shown to reduce the incidence of fracture in osteoporotic patients [3, 4]. Sr^{2+} is present in the mineral phase of bone, especially in the regions of high metabolic turnover [5]. It was also demonstrated that synthetic CaPs doped with different amounts of Sr^{2+} substituting Ca^{2+} stimulate in vitro osteoblast activity and inhibit osteoclast proliferation [6, 7].

CaPs are being extensively investigated as materials for coating of various bone implants because they are able to enhance the surface bioactivity and improve in vivo performance (i.e. biocompatibility, biodegradation, osseoconductivity, osseointuctivity), thanks to the high

chemical similarity with the inorganic phase of bone [8, 9]. In particular, hydroxyapatite (HA) can host a wide variety of functional ions in its lattice [10]. Upon contact with the biological environment these ions can activate specific biochemical mechanisms related to new bone formation and resorption [10].

Particularly, this chapter describes the development of Sr-doped apatite for the development of targets addressed to deposition of bioactive coatings with increased functionality. Several wet-chemical [11-13] and physical deposition strategies such as radio frequency magnetron sputtering [14], thermal plasma spray [15], vacuum plasma spray [16], cold spray [17] and ion beam assisted deposition (IBAD) [18], have been tested to fabricate CaPs coatings.

Among the materials used for bone implants, poly(etheretherketone) (PEEK), an organic colourless semicrystalline thermoplastic polymer of the family of polyaryletherketone, is one of the most promising candidates for replacing metal implants components in the field of orthopedics and traumatology [19-21] due to its excellent mechanical resistance and chemical inertness in physiological environment.

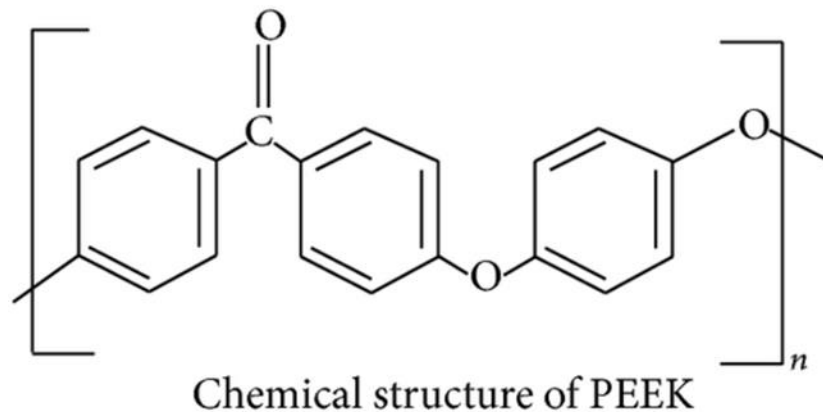


Figure 4.1. Structure of Poly-ether-ether-ketone

PEEK was approved as an implantable biomaterial by the U.S. Food and Drug Administration (FDA), and nowadays it is used in a variety of orthopedic implants especially for spinal fusion

thanks to its biocompatibility, chemical and sterilization resistance, translucency to X-Rays and optimal mechanical properties which can be further improved with carbon fibers [19, 22]. It has an elastic modulus closer to human cortical bone (14GPa) [23] (4 GPa for pure PEEK [19] and 18 GPa for carbon-reinforced PEEK [22]) if compared with titanium or titanium alloy (102-110 GPa) [24]. Consequently, the stress-shielding effect caused by a mismatch in elastic modulus between the foreign implant and host bone tissue can be reduced using PEEK-based implants [21]. However, the main problem with PEEK, common to most polymers, is its very low bioactivity (i.e. in the scientific literature PEEK is categorized as a bioinert material) and thus the lack of osseointegration properties that limits biological fixation in bone tissue and long-term in vivo stability [25, 26]. Therefore, to facilitate the formation of a tight bond of the bone with the implant surface, significant effort is being dedicated today to the modification of PEEK surface properties by physical or chemical methods or by coating. [27, 28]. Various bioactive materials have been deposited onto PEEK including calcium phosphates (CaPs) [11, 12, 13, 28, 29], titanium [30, 31], titanium oxides [32, 33] and zirconium [34].

Once selected PEEK as the material on which the deposition has to be made, the characteristics required for the elective deposition technique are multiple. It needs to have strong control over stoichiometry and deposition rate, to enable control of the coating thickness. In addition, the deposition has to be carried out at low temperature, thus permitting the deposition on heat-sensitive materials, like thermoplastic polymers. Pulsed electron deposition (PED) match all these characteristics, and is an emerging, effective and versatile physical deposition technique [35, 36]. Another main advantage of PED technique is the possibility to coat heat-sensitive materials such as thermoplastic polymers, since the technique works efficiently even at room temperature [37, 38]. When compared to the conceptually similar but more diffused pulsed laser

deposition (PLD) technique, PED presents several advantages due the different nature of the ablating source (electrons vs. photons) including higher pulse energy, capability to ablate wide band-gap and highly reflective materials, and much lower costs for industrial scalability [39, 40]. Recently, bioactive CaP coatings have been successfully deposited by PED on titanium alloy substrates in order to improve the osseointegration of common orthopedic implantable devices [41]. However, to the best of my knowledge no reports are available in literature concerning the deposition of ionically substituted CaP coatings onto PEEK. Therefore, the use of PEEK implants coated by Sr²⁺-doped CaPs can be an effective strategy to improve the bone-implant integration, particularly for osteoporotic patients.

4.2. Materials and Methods

Raw materials

Phosphoric acid (H₃PO₄, purity ≥85 wt.%), calcium hydroxide (Ca(OH)₂, purity ≥95%), strontium nitrate (Sr(NO₃)₂, purity ≥98%), potassium bromide (KBr, FT-IR grade, purity ≥99%), nitric acid (HNO₃, purity ≥70%), isopropyl alcohol ((CH₃)₂CHOH, purity ≥98%) were purchased from Sigma Aldrich. Poly(etheretherketone) (PEEK) sheets (thickness ~6mm) were purchased from Direct Plastics Ltd (Sheffield, UK) and used after ultrasonic cleaning in isopropyl alcohol for 5 min and then in water for an additional 5 min. Ultrapure water (0.22 mS, 25 °C) was used in all experiments.

Synthesis of Sr²⁺-substituted CaP powders

The synthesis of Sr²⁺-free powder (hereafter CaP) in the crystalline form of HA was carried out at 40 °C by a neutralization reaction in aqueous environment dropping 600 mL of H₃PO₄ aqueous solution (1.25 M) into 750 mL of a basic aqueous suspension of Ca(OH)₂ (1.7 M) (Ca/P

molar ratio of 1.67). Sr²⁺-doped CaPs (hereafter SrCaPs) were prepared under the same conditions of CaP by adding Sr(NO₃)₂ to the Ca(OH)₂ suspension. The quantity of Ca²⁺ and PO₄³⁻ was kept constant in the preparations while different quantities of Sr²⁺ were added in the basic suspension to accomplish an initial Sr/Ca molar ratio of 0.04, 0.10 and 0.20 for SrCaP1, SrCaP2 and SrCaP3, respectively. After the neutralization reaction, the mixture was kept stirring at 40 °C for 2h, then it was left standing overnight at room temperature to allow the deposition of the inorganic phase. This latter was isolated by centrifugation of the reaction mixture, repeatedly washed with water and dried at 40 °C overnight. The dried powders were manually milled and sieved at 106 µm.

Targets preparation

Cylindrical CaPs targets (diameter = 23 mm, thickness 4 mm) were prepared by compacting 5 g of powder at room temperature by uniaxial pressing at 30 MPa, followed by cold isostatic pressing at 300 MPa. To improve the strength and lowering the porosity of the final targets, the prepared pellets were thermally treated in air at 1250 °C for 1 h, with a heating rate of 2.5 °C min⁻¹ using a LHT02/16 furnace (Nabertherm GmbH, Lilienthal, Germany).

Coating Deposition

Coatings were deposited by a Pulsed Electron Deposition (PED) process based on a commercially available Ionized Jet Deposition system (Noivion Srl, Rovereto (TN), Italy). The deposition was achieved through the ablation of the target mounted on a rotating target holder by a fast pulse (100 ns) of high energy (10 J) and high-density (109 W cm⁻²) electrons. The ablated material was then directed toward the substrate (i.e. PEEK cubes with side ~6 mm) mounted on a rotating holder and located at a distance of 10 cm from the target in order to obtain a homogenous layer while maintaining a suitable deposition rate (~130 Å min⁻¹). The vacuum chamber was

initially evacuated down to a base pressure of 1.0×10^{-7} mbar by a turbomolecular pump (EXT255H, Edwards, Crawley, England) and then raised by controlled flow of oxygen (purity level = 99.999%) to 1.2×10^{-4} mbar. The working voltage and the electron beam frequency were set at 17 kV and 8 Hz, respectively. After deposition, films were annealed at 130 °C for 6 h in air, using a LHT02/16 furnace (Nabertherm GmbH, Lilienthal, Germany) mounting a C42-type controller, with a ramp of 4 °C min^{-1} both for the heating and the cooling steps.

Characterizations

The X-ray diffraction (XRD) patterns of the powders as well as of the targets were recorded on a D8 Advance diffractometer (Bruker, Karlsruhe, Germany) equipped with a Lynx-eye position sensitive detector using Cu K α radiation ($\lambda = 1.54178 \text{ \AA}$) generated at 40 kV and 40 mA. XRD spectra were recorded in the 2θ range from 10 to 60° with a step size (2θ) of 0.02° and a counting time of 0.5 s. XRD patterns of the coatings were recorded in out-of-plane and grazing incidence geometry, using a Smart Lab diffractometer (Rigaku Co., Tokyo, Japan) equipped with a rotating anode (Cu K α , $\lambda = 1.54180 \text{ \AA}$). The incidence angle was 0.8° in order to reduce the diffraction from the substrate.

Evaluation of the crystal parameters was performed by full-profile Rietveld analysis of the XRD spectrum (TOPAS v. 4.2, Bruker AXS, Karlsruhe, Germany).

Fourier transform infrared (FTIR) spectroscopy analyses were achieved on a Nicolet 5700 spectrometer (Thermo Fisher Scientific Inc., Waltham, USA). The powder sample (about 1 mg) was mixed with about 200 mg of anhydrous KBr and pressed into 7 mm diameter discs. Spectra were registered with a resolution of 2 cm^{-1} by accumulation of 64 scans covering the 4000 to 400 cm^{-1} range.

Calcium, phosphate and strontium contents of the powders were determined by inductively coupled plasma optical emission spectrometry (ICP-OES) using a 5100 spectrometer (Agilent Technologies, Santa Clara, USA). Samples were prepared dissolving an aliquot of 20 mg in 50 mL of a 1 wt% HNO₃ solution.

The carbonate content of the powders was evaluated by thermogravimetric analysis (TGA) investigations using a STA 449 Jupiter (Netzsch GmbH, Selb, Germany) apparatus. About 10 mg of sample was weighted in a platinum crucible and heated from room temperature to 1200 °C under airflow with a heating rate of 10 °C min⁻¹.

Microstructural, chemical and morphological characterization of the coatings was carried out by field emission gun scanning electron microscopy (FEG-SEM) using a Sigma NTS GmbH (Carl Zeiss, Oberkochen, Germany) equipped with an energy dispersive X-ray spectroscopy (EDX) microanalysis system (INCA Energy 300, Oxford instruments, Abingdon-on-Thames, UK). Prior to the morphological analyses the specimens were covered with a coating of Au using a Sputter Coater E5100 (Polaron Equipment, Hertfordshire, UK).

Film morphology and roughness were also evaluated by an Atomic Force Microscope (AFM) operating in semi-contact mode at ambient conditions (Stand-Alone SMENA AFM, NT-MDT, Moscow, Russia). The AFM was equipped with a SFC050 head, mounting silicon probes with a guaranteed curvature radius of about 10 nm and resonance frequencies of 190–330 kHz (NSG series probes, NT-MDT, Moscow, RU). The reported values for the Root Mean Square roughness

(RMS = $\sqrt{\frac{1}{n} \sum_{i=1}^n y_i^2}$ where y_i is the i -th vertical distance from the mean line to the data point and n is the number of image pixels) were calculated by averaging the values obtained upon several non-overlapping sample regions, whose dimensions ranged from (10 × 10) μm² to (2 × 2) μm².

All the images were unfiltered, except for a 2nd order leveling, and acquired with a resolution of (512 x 512) pixels.

Nanoindentation tests were performed with an instrumented indenter (Nanoindenter Tester NHT2, CSM Instruments - Anton Paar S.r.l, Peseux, Switzerland) in order to determine the indentation hardness (HIT) and the Young's modulus (EIT) of both as-deposited and annealed films, according to the Oliver-Pharr method [42]. All tests were performed in air and at room temperature using a Berkovich diamond tip, after a preliminary calibration on standard fused silica. At least ten indentations were performed on different areas of the coated samples according to the following protocol: loading to the maximum load (P_{max}) in 10 s, holding time of 2 s and unloading in 10 s; the indentation was performed at constant strain mode with a maximum load of 6 mN.

The surface wettability was characterized by water contact angle (CA) measurement using a Digidrop contact angle meter (GBX Instrumentation Scientifique, Romance, France). The volume of the drop was $\sim 0,5 \mu\text{l}$, corresponding to a contact radius with the surface, uncoated or coated, of $\sim 0,5 \text{ mm}$. Contact angle values were acquired on at least three different positions over the sample surface and the mean value was provided.

4.3. Results and discussion

4.3.1. Sr^{2+} -substituted CaP powders

The chemical-physical features of the precursor powders were evaluated to determine the nature of the materials prior to use them as a target for the deposition of coatings.

The chemical composition of the synthesized powders evaluated by ICP-OES, for Ca, Sr and P content, and TGA, for CO_3^{2-} content, is reported in **Table 4.I**.

Table 4.I. Chemical composition of the powder samples

<i>Sample</i>	<i>Ca/P</i>	<i>Sr/Ca</i>	<i>Tot cat./ PO₄³⁻</i>	<i>PO₄³⁻/CO₃²⁻</i>	<i>Tot cat/ Tot anions</i>
CaP	1.69	---	1.69	0.04	1.63
SrCaP1	1.57	0.04	1.63	0.05	1.55
SrCaP2	1.54	0.09	1.68	0.07	1.57
SrCaP3	1.45	0.15	1.66	0.07	1.55

The Ca/P molar ratio of CaP is close to 1.67, which corresponds to stoichiometric HA, and similar to the reactants used in the preparations. A small variation was caused by a B-type CO_3^{2-} substitution (i.e. replacing PO_4^{3-} ions; see FT-IR characterization below). The amount of Sr^{2+} inside the structure of SrCaPs increases up to about 9 wt% as a function of the quantity of $\text{Sr}(\text{NO}_3)_2$ added in the basic solution during the syntheses. Similarly, the Ca/P molar ratio decreases according to the substitution of Sr^{2+} for Ca^{2+} ions. The comparison between the Sr/Ca molar ratios of the powders with those of the reactants suggests that at low concentration, all Sr^{2+} ions are able to enter in the crystal structure, while at higher concentrations only a partial substitution occurred. The (Ca+Sr)/P molar ratio of the doped samples was similar to the Ca/P of the undoped sample independently of the Sr^{2+} content indicating an effective replacement of Sr^{2+} for Ca^{2+} in the crystal lattice. Samples were not synthesized under inert gas, therefore a limited amount of CO_3^{2-} adsorbed on the surface and/or entrapped in the lattice of the material derived from unintentionally dissolved CO_2 in the preparation media, is present. The amount of CO_3^{2-}

was evaluated according to the weight loss observed in TGA curves between 550 and 950 °C (**Fig. 4.2.**) [43].

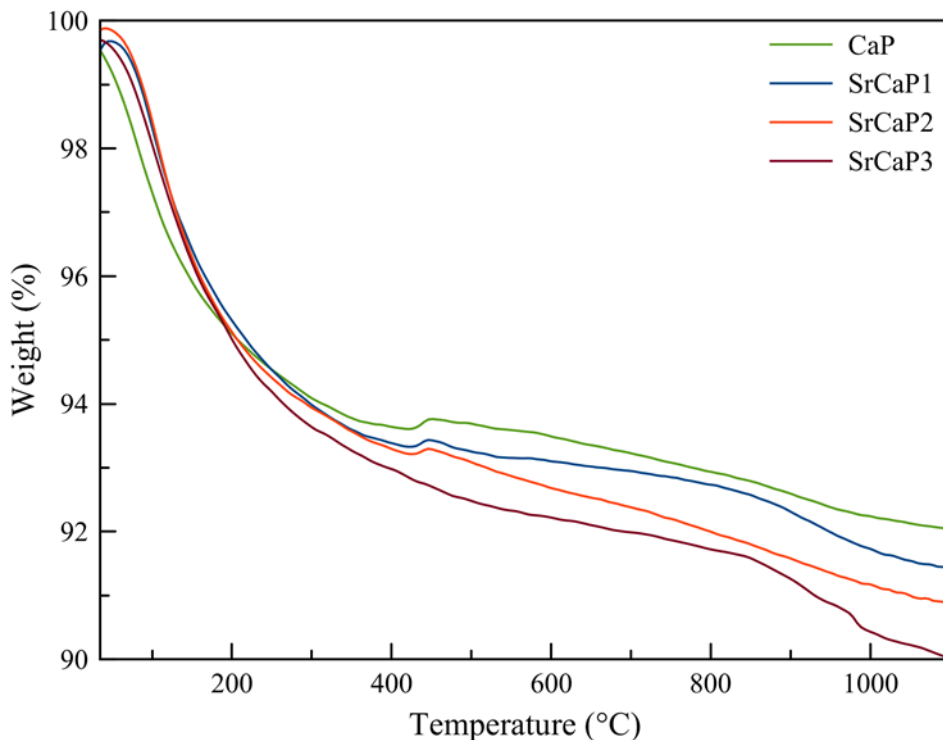


Figure 4.2. TGA curve of CaP, SrCaP1, SrCaP2 and SrCaP3 powders

The CO_3^{2-} substitution slightly increases as a function of Sr^{2+} extent as a consequence of the structural strain caused by the partial replacement of Sr^{2+} for Ca^{2+} , which allows to accommodate more CO_3^{2-} ions as reported previously [44].

The XRD patterns of the powders are reported in **Figure 4.3.A**. All diffraction patterns display the typical features of nanocrystalline HA single phase (ICSD: 081442). The shift of the XRD reflection peaks to lower angles as a function of Sr^{2+} content (**Figure 4.4.** and **Table 4.II.**) confirms an increase of d-spacings and the effective substitution of Sr^{2+} for Ca^{2+} as previously reported [45, 46]. Moreover, the crystal parameters of the samples calculated by full-profile Rietveld analysis of the XRD patterns (**Table 4.II.**) reveal that the inclusion of Sr^{2+} , which has a

larger ionic radius compared to Ca^{2+} (1.12 vs. 0.99 Å), caused the expansion of the lattice parameters (mainly along the c axis) and the increase of cell volume [45, 46].

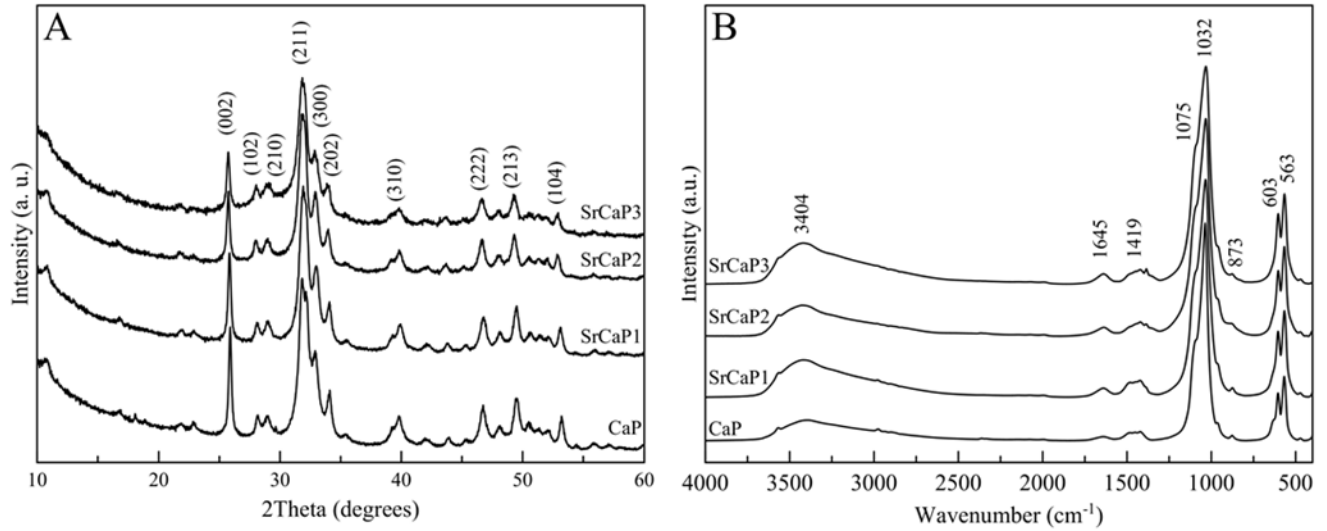


Figure 4.3. (A) XRD patterns and (B) FTIR spectra of the powder samples.

Table 4.II. Crystal parameters and splitting factor (SF) of the CaP, SrCaP1, SrCaP2 and SrCaP3 powders.

<i>Samples</i>	<i>Position</i> ($2\theta^\circ$)(I_{002})	$a = b$ (Å) ^a	c (Å) ^a	<i>Cell volume</i> (Å ³) ^a	<i>Splitting Factor</i> (SF) ^b
CaP	25.90	9,433(1)	6,890(1)	531,0(1)	4,67
SrCaP1	25.84	9,414(1)	6,902 (1)	529,7(1)	3,90
SrCaP2	25.76	9,433(1)	6,930(1)	534,0(1)	3,71
SrCaP3	25.74	9,441(2)	6,930(1)	535,0(2)	3,71

^aTheoretical values of stoichiometric HA used for the Rietveld refinement are: $a = b = 9.421(8)$ Å and $c = 6.881(3)$ Å with a cell volume = $529.02(0)$ Å³.

^bCalculated from FTIR spectra (SF: measure consists on sum of the heights of the stretching of PO_4^{3-} signals at 603 and 560 cm^{-1} and divided by the height of the valley between them at ~ 588 cm^{-1} ; all heights were measured above a baseline drawn from approximately 780–495 cm^{-1}).

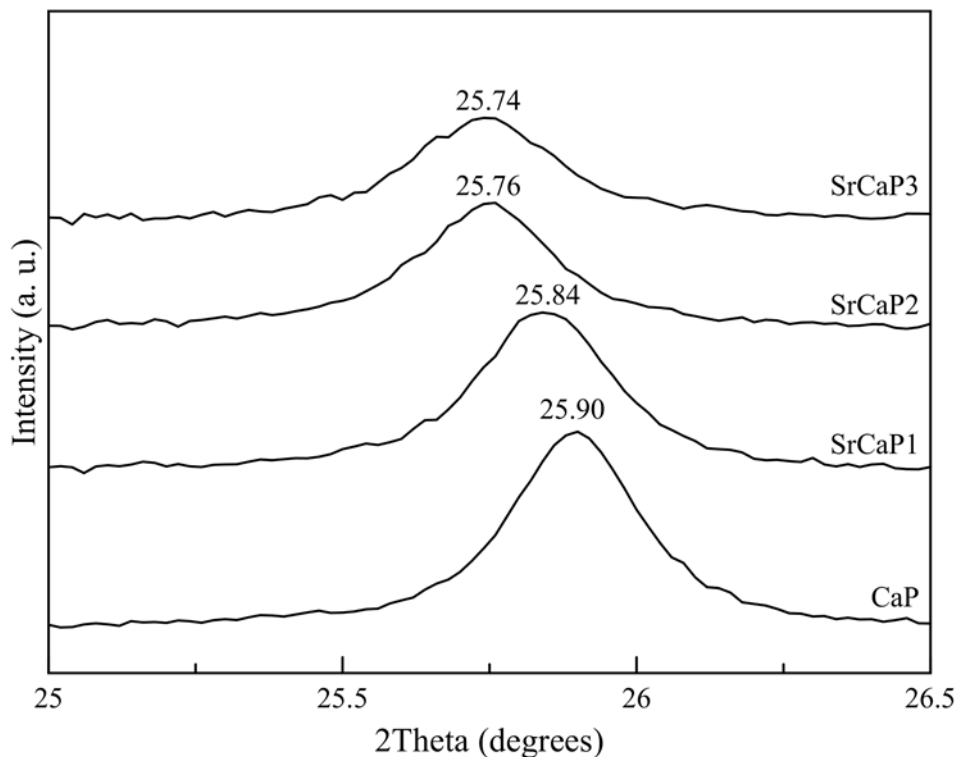


Figure 4.4. Magnification of the XRD spectra of CaP, SrCaP1, SrCaP2 and SrCaP3 powders in the region of (002) reflection.

The FTIR spectra of the powders (**Figure 4.3.B.**) show the characteristic signals of HA [9]. In particular, they display a main broad band at about 1032 cm^{-1} with a shoulder at about 1075 cm^{-1} attributed to the triply degenerated asymmetric stretching mode of the PO_4^{3-} groups ($\nu_3\text{PO}_4$). Other signals appear at 605 and 563 cm^{-1} that were attributed to the triply degenerated bending mode of the PO_4^{3-} groups ($\nu_4\text{PO}_4$). In addition, bands of the CO_3^{2-} incorporated in the structure are evident at 1419 ($\nu_3\text{CO}_3$ B-type) and 873 cm^{-1} ($\nu_2\text{CO}_3$ B-type) as well as the signal at 1645 cm^{-1} ($\nu\text{H}_2\text{O}$) and the broad band at 3404 cm^{-1} ($\nu\text{sH}_2\text{O}$ and $\nu\text{asH}_2\text{O}$) attributed to adsorbed water. The curve-fitting analyses of the FTIR spectra of the powder samples in the regions $700\text{-}500\text{ cm}^{-1}$ and $1900\text{-}1300\text{ cm}^{-1}$ as well as their assignments are reported in **Figure 4.5** and **Table 4.III.**

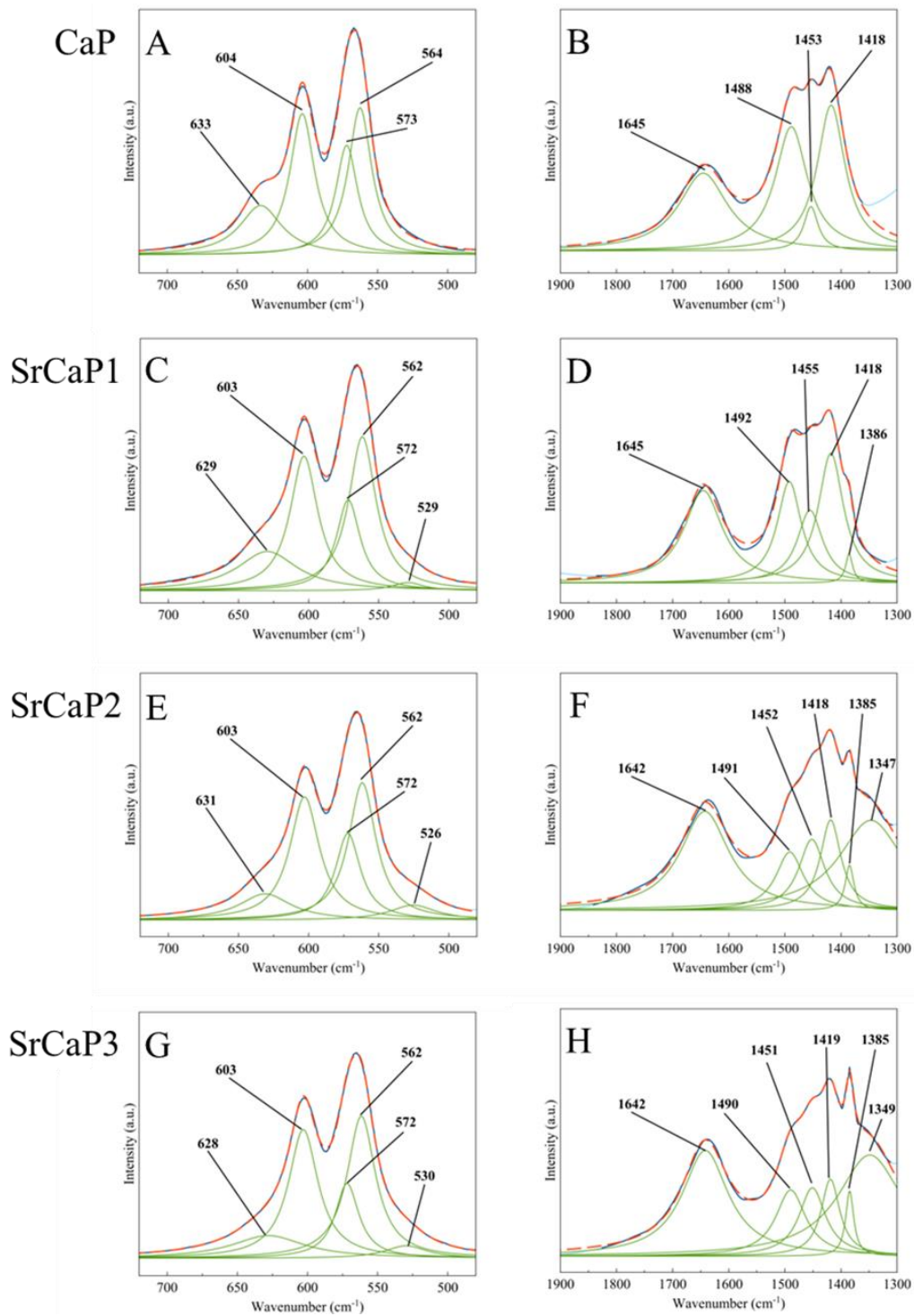


Figure 4.5. Curve fitting of the FTIR bands in the regions 700-500 cm⁻¹ and 1900-1300 cm⁻¹ of CaP (A,B), SrCaP1 (C,D) SrCaP2 (E,F) SrCaP3 (G,H) powders. Spectra were deconvoluted by non-linear fitting using Lorentzian curves with Magic Plot 2.5.1 software.

Table 4.III. Assignment of the FTIR peaks in the regions 700-500 cm⁻¹ and 1900-1300 cm⁻¹

	<i>Peak position range (cm⁻¹)</i>	<i>Assignments</i>
Region 700-500 cm⁻¹	629 - 633	v _L OH
	603 - 604	v ₄ PO ₄
	572 - 573	v ₄ PO ₄
	562 - 564	v ₄ PO ₄
	526 - 530	v ₄ HPO ₄
Region 1900-1300 cm⁻¹	1642 - 1645	v H ₂ O
	1488 - 1492	v ₃ CO ₃ (A-type)
	1451 - 1455	v ₃ CO ₃ (B-type)
	1418 - 1419	v ₃ CO ₃ (B-type)
	1385 - 1386	v ₃ NO ₃
	1347 - 1349	v ₃ HPO ₄

Considering the region 700-500 cm⁻¹, the signal at about 530 cm⁻¹ assigned to the v₄HPO₄ appeared when the Sr²⁺-substitution occurred and its relative intensity increases as a function of Sr²⁺ content, while the relative intensity of the signal at about 630 cm⁻¹ attributed to the v_LOH decreases. These findings are in agreement with several works previously published [45-48] confirming that substitution of Ca²⁺ by Sr²⁺ induces the accommodation of HPO₄²⁻ groups in the crystalline structure and decreases the hydroxylation level of the materials (as also revealed by the broadening of v₁OH signal at 3571 cm⁻¹). Considering the region 1900-1300 cm⁻¹, the appearance in the SrCaP2 and SrCaP3 samples of the signal at about 1350 cm⁻¹ attributed to the v₃HPO₄, is in agreement with the accommodation of HPO₄²⁻ groups at high Sr²⁺ doping extent. Moreover, a sharp peak was observed at 1385 cm⁻¹, which corresponds to a small amount of NO₃⁻ coming from the Sr(NO₃)₂. A detailed analysis of the carbonate signals revealed that in all the samples both A- and B-type CO₃²⁻ ions were present and that the amount of A-type decreased as a function of Sr²⁺ content in agreement with a decreased amount of OH⁻ groups.

FTIR spectra were also analyzed to calculate the splitting factor (SF) value which is a well-reported index for the evaluation of crystallinity degree [49]. SF values (**Table 4.II**) show a clear decreasing trend in the crystallinity degree as a function of Sr^{2+} content.

From these findings it is clear that Sr^{2+} -doped CaPs in the crystalline form of HA with a Sr^{2+} substitution for Ca^{2+} in the range of 0-9 wt% were successfully prepared. Furthermore, there is evidence of B-type CO_3^{2-} substitution within the all the samples in the range 1.3-2.1 wt%.

4.3.2. Sr^{2+} -substituted CaP targets

Compact targets were prepared by pressing the as-synthesized powders followed by thermal treatment at 1250 °C for 1h. All the targets were characterized by a dense and residual porosity-free surface, and the corresponding XRD patterns (**Figure 4.6.A.**) show the typical signals of high crystalline HA without the presence of secondary phases. Also in this case a clear shift of the XRD peaks to lower angles (**Figure 4.6.B.**) as well as the expansion of the lattice parameters and the increase of cell volume (**Table 4.IV.**) were detected as a function of Sr^{2+} content in the starting powders, corroborating the fact that Sr^{2+} was retained in the crystal structure of the sintered materials as substituent for Ca^{2+} .

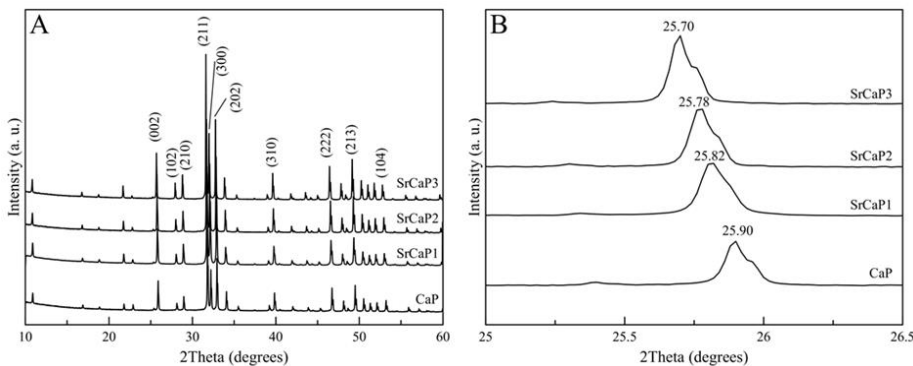


Figure 4.6. (A) XRD patterns of the targets and (B) magnification of the patterns in the region of (002) reflection.

Table 4.IV. Crystal parameters of the CaP, SrCaP1, SrCaP2 and SrCaP3 targets.

<i>Sample</i>	<i>Position (2θ) (I_{002})</i>	<i>a = b (Å)^a</i>	<i>c (Å)^a</i>	<i>Cell volume (Å³)^a</i>
CaP	25.90	9.422(1)	6.887(1)	529.5(1)
SrCaP1	25.82	9.437(1)	6.903(1)	531.7(1)
SrCaP2	25.78	9.451(1)	6.917(1)	535.1(1)
SrCaP3	25.70	9.472(1)	6.939(1)	539.1(1)

^aTheoretical values of stoichiometric HA used for the Rietveld refinement are: a = b = 9.421(8) Å and c = 6.881(3) Å with a cell volume = 529.02(0) Å³.

4.3.3. Sr²⁺ substituted CaP coatings on PEEK

XRD patterns of the as-deposited coatings (**Figure 4.7.A.**) revealed that they were mainly composed of an amorphous phase because no other peaks in addition to those of PEEK were detected. The presence of CaO was evidenced by the occurrence of the peak at 37.4° related to the plane (200) (ICSD: 060199). The presence of the accessory CaO phase has been already reported for CaP coatings prepared with similar techniques [41, 50-52]; its presence is particularly hard to avoid because the plasma-target interaction can produce species due to HA decomposition such as Ca₄P₂O₉, Ca₃(PO₄)₂, CaO, P₂O₅, and H₂O. The formation of an amorphous rather than a crystalline phase was ascribed to the low kinetic energy of the incoming ions, which was insufficient to create a crystalline structure since the deposition was carried out at room temperature. It is well reported that all the coating techniques based upon ablation or plasma produce amorphous materials and a thermal treatment post deposition is required to enhance the crystallinity of the coatings to avoid rapidly-dissolving amorphous phases which can lead to detrimental implant mobilization [27, 51]. The annealing temperature was set to 130 °C to remain below the glass transition temperature of PEEK that is 143 °C [53]. After the annealing, crystalline phases were obtained in all the samples. In particular, the XRD patterns of the

annealed CaP, SrCaP1, SrCaP2, and SrCaP3 (**Figure 4.7.B.**) showed relatively intense peaks at about 25.8° and at 31.7° related to the (002) and (211) planes of HA (ICSD: 081442). Magnification of the annealed patterns (**Figure 4.VI**) revealed also the presence of the other less intense peaks at 32.8° and 34.0° related to the (112) and (202) planes of HA. The XRD signals of HA are broad and not well defined indicating a relatively low degree of crystallinity close to that of biogenic HA [54]. The pattern of annealed SrCaP3 showed also two other peaks at 26.6° and 28.4° that were attributed to unidentified secondary phases. The peak coming from CaO was not detected after annealing. Comparing the peak position of the (002) plane of SrCaP1, SrCaP2, and SrCaP3 (**Figure 4.8.**) a shift to lower angles seems to occur, indicating modifications of the lattice parameters due to the presence of Sr^{2+} .

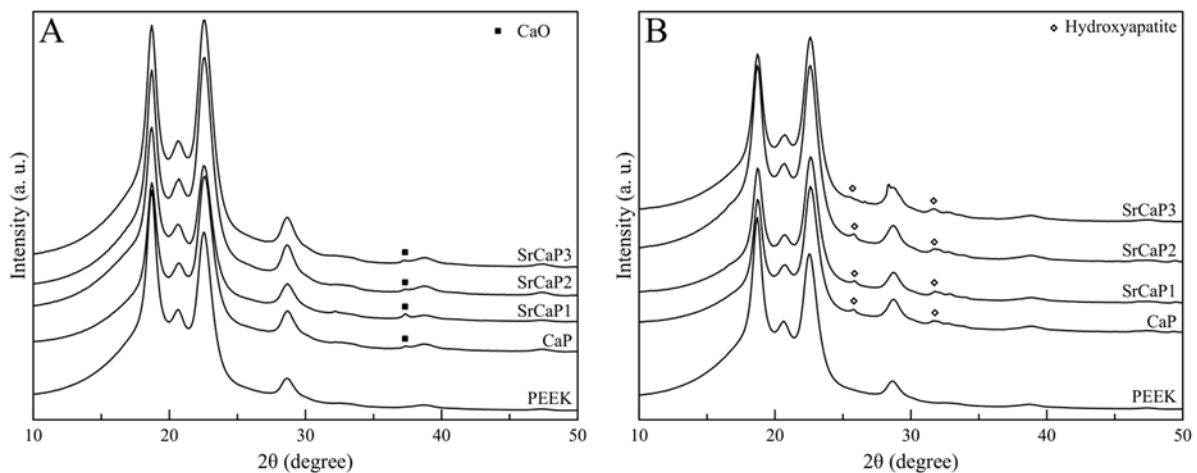


Figure 4.7. XRD patterns of the (A) as-deposited and (B) annealed coatings.

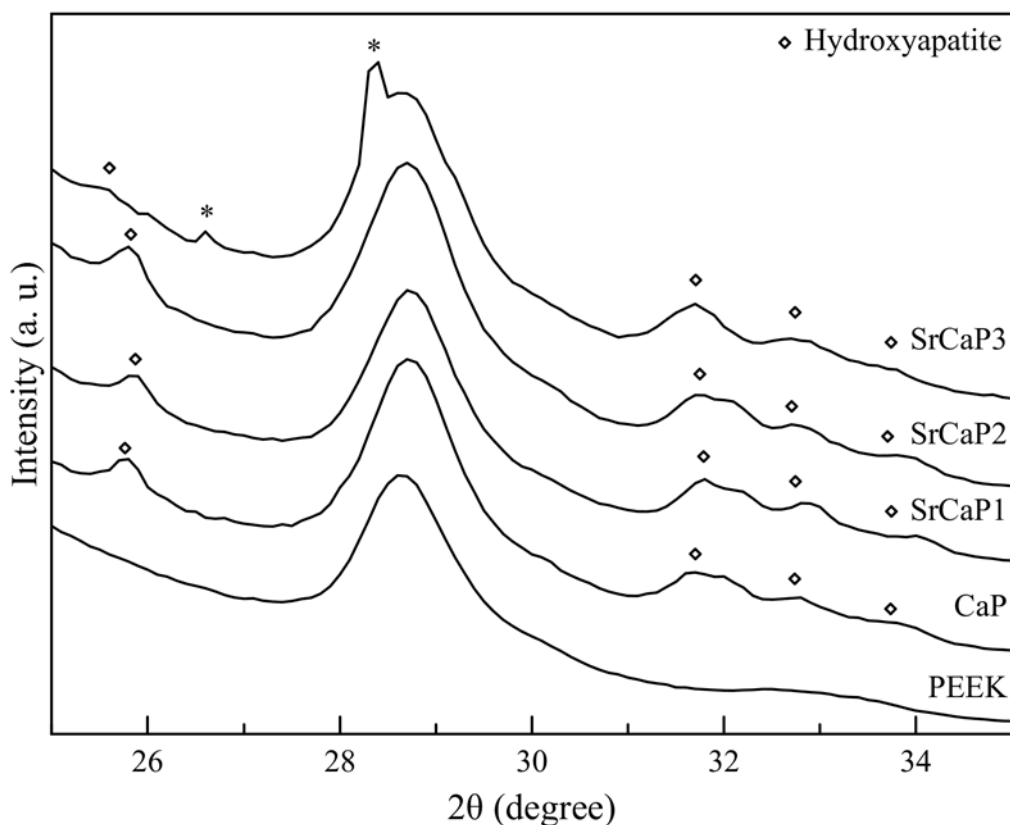


Figure 4.8. Magnification of XRD patterns of the annealed coatings. * indicates unattributed peaks.

The chemical composition of the as deposited and annealed coatings evaluated by EDX (**Table 4.V.**) showed an increased amount of Sr^{2+} as a function of that contained in targets. Remarkably, the Sr/Ca molar ratios of the as-deposited SrCaPs coatings matched closely with those of the targets while the Ca/P molar ratios were different. It was extensively reported that the Ca/P ratio is strongly influenced by deposition parameters [51]. A Ca/P ratio higher than that of the target is commonly observed when the deposition involves a low-pressure ambient environment (10-4–10-2 torr) because volatile byproducts as P_2O_5 may be lost leading to a P deficiency [55]. However, CaPs with a high Ca/P ratio were shown to increase osteoblast adhesion [56], therefore this aspect is not to be considered as a disadvantage. The annealing treatment slightly decreased

the Ca/P ratio, while it did not affect the Sr/Ca molar ratio. The (Ca+Sr)/P molar ratio of the annealed SrCaP coatings was close to the Ca/P ratio of the un-doped film, indicating a replacement of Sr²⁺ for Ca²⁺ in the crystal lattice of HAs constituting the film as observed by XRD analyses.

Table 4.V. Chemical composition of the as-deposited and annealed coatings evaluated by EDX.

<i>Sample</i>	<i>As deposited</i>			<i>Annealed</i>		
	<i>Ca/P</i>	<i>Sr/Ca</i>	<i>(Ca+Sr)/P</i>	<i>Ca/P</i>	<i>Sr/Ca</i>	<i>(Ca+Sr)/P</i>
Ca/P	2.72±0.05	---	---	2.43±0.04	---	---
SrCaP1	2.49±0.03	0.04±0.02	2.58±0.05	2.25±0.03	0.03±0.02	2.32±0.04
SrCaP2	2.52±0.03	0.08±0.02	2.71±0.04	2.33±0.03	0.08±0.02	2.52±0.03
SrCaP3	2.39±0.03	0.15±0.03	2.74±0.04	2.21±0.04	0.16±0.02	2.56±0.04

The surface morphology of the as-deposited and annealed coatings (**Figure 4.9.**) was evaluated by FEG-SEM revealing that in all the cases they are dense and uniform films constituted by particles of globular and in some cases splat-like shape typical of CaP films prepared with similar techniques [41, 51, 52, 57, 58, 59]. CaP coatings mainly showed sub-micrometer size particles, while SrCaP coatings exhibited also particles up to few micrometers in size. The annealing treatment and the amount of Sr²⁺ did not significantly change the morphology as well the dimensions of the particles. For the sake of simplicity in **Figure 4.9.**, only the FEG-SEM micrographs of as-deposited and annealed CaP and SrCaP3 are reported, in fact the micrographs of the other SrCaP samples showed similar features to those of SrCaP3. EDX map (**Figure 4.10.**) of the annealed SrCaP3 is consistent with a homogenous Sr²⁺ distribution.

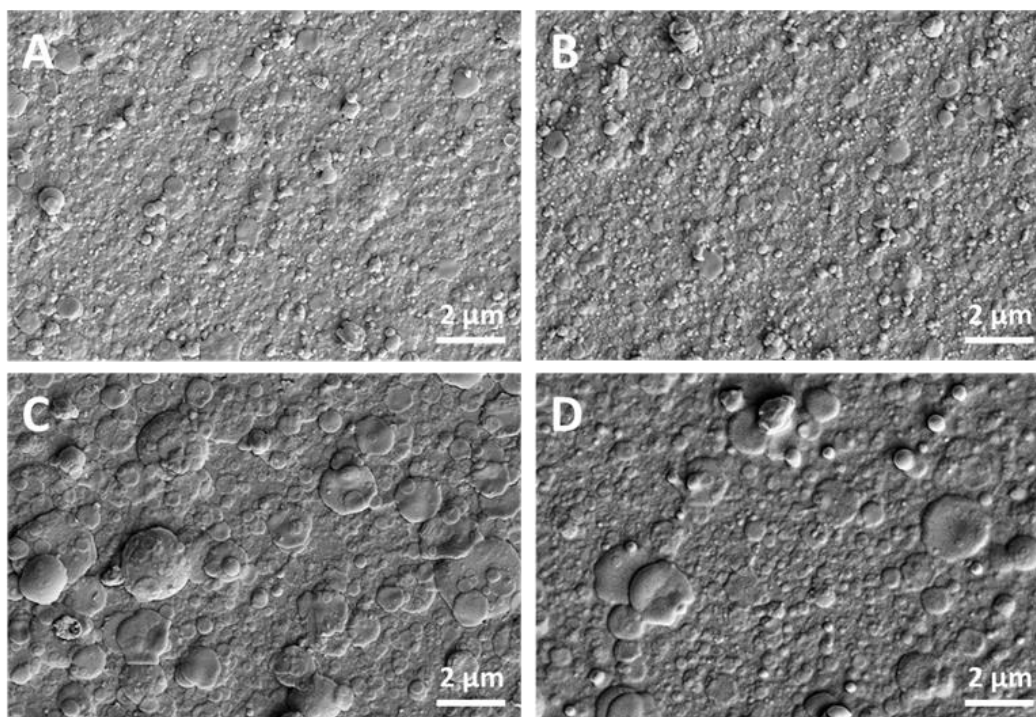


Figure 4.9. FEG-SEM micrographs of (A) as-deposited CaP, (B) annealed CaP, (C) as-deposited SrCaP3, and (D) annealed SrCaP3 coatings.

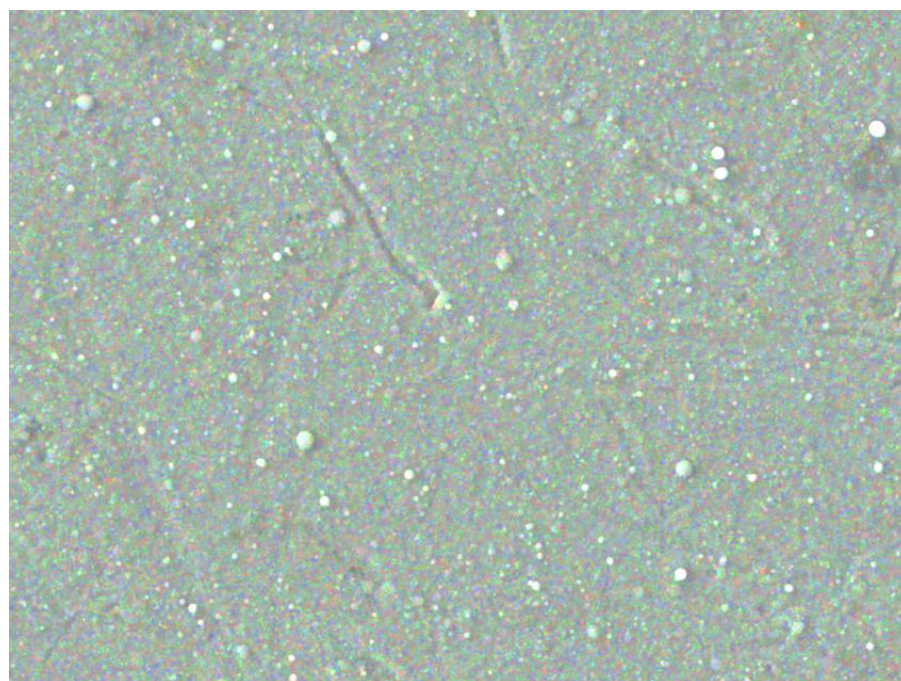


Figure 4.10. EDX map recorded from the annealed SrCaP3 coating. Green: Sr.

Surface nano-topography was investigated in detail by AFM (**Figure 4.11** and **Table 4.VI**). AFM topographical images of as-deposited as well as annealed coatings (**Figures 4.11.A-G.**) indicated that the larger particles were indeed composed of aggregated small sub-micrometric grains, the size of which ranged mainly from 50 to 100 nm. The formation of this nano-structure should be emphasized since nano-topography plays an important role on the ability of the coatings to promote new bone apposition [55]. Nanostructured coatings are known to exhibit a higher surface area, leading to enhanced cell adhesion and proliferation and promoting bone tissue regeneration as compared to micro-structured coatings [60].

AFM analysis also confirmed that the presence of Sr^{2+} slightly enhanced the size of the grains, as indicated by the moderate increase of RMS values in comparison to those of CaP coatings (**Figure 4.11.I.** and **Table 4.VI**). The annealing treatment did not affect the surface topography as well as the roughness of the coatings as already suggested by FEG-SEM images. Noteworthy, the apposition of the CaP layers by PED on the bare PEEK increased the surface roughness (**Figure 4.11.I.**) while decreasing the water contact angle, corresponding to a higher wettability (**Figure 4.11.J.** and **Table 4.VI**), thus achieving devices with potentially improved biocompatibility and osseointegration ability compared to bare PEEK. In fact it was reported that the improvement of PEEK surface roughness and wettability increases adhesion, spreading, proliferation, and differentiation of bone cells [27]. The partial substitution of Sr^{2+} to Ca^{2+} led to a slight decrease of wettability, however the contact angle values of all the SrCaP coatings remained suitable for bone cell adhesion, proliferation and differentiation [61].

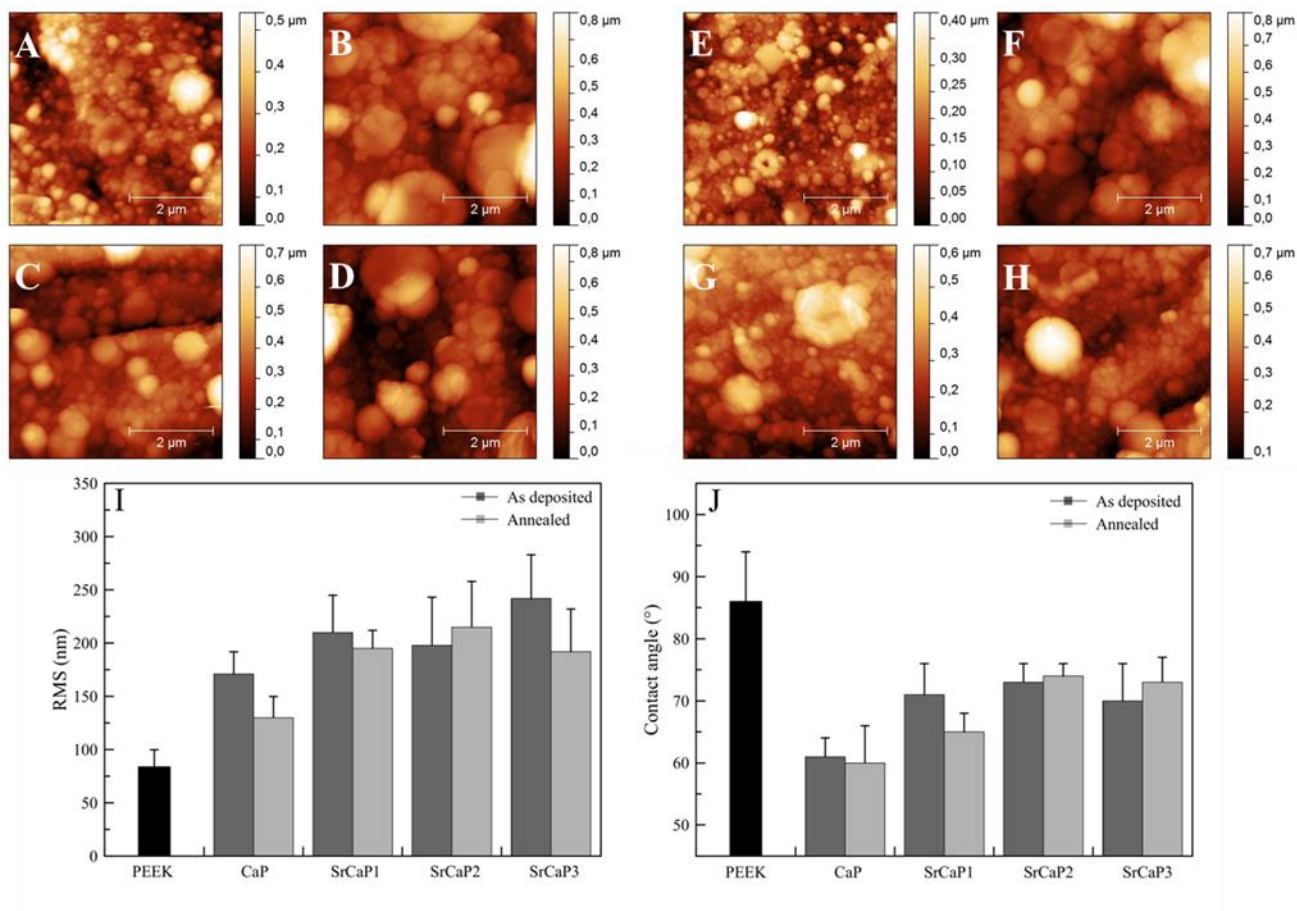


Figure 4.11. AFM topographical images of the (A-D) as-deposited and (E-H) annealed coatings; (A, E) CaP, (B, F) SrCaP1, (C, G) SrCaP2 and (D, H) SrCaP3. (I) RMS (calculated on a 10x10 μm² area) and (J) water contact angle of bare PEEK and the as-deposited and annealed coatings.

Table 4.VI. Root Mean Square roughness (RMS) and water contact angle (CA) values of PEEK and the as-deposited and annealed coatings

		<i>RMS (nm)</i>			<i>CA (°)</i>
		<i>(10 x 10) μm</i>	<i>(5 x 5) μm</i>	<i>(2 x 2) μm</i>	
	PEEK	84±16	64±15	25±8	86±8
As-deposited	CaP	171±21	84±5	43±2	61±3
	SrCaP1	210±35	151±25	58±6	71±5
	SrCaP2	198±45	94±21	57±13	73±3
	SrCaP3	242±41	140±32	62±12	70±6
Annealed	CaP	130±20	88±19	48±3	60±6
	SrCaP1	195±17	137±25	58±1	65±3
	SrCaP2	215±43	93±19	40±8	74±2
	SrCaP3	192±40	125±36	73±24	73±4

Nano-mechanical properties of as-deposited and annealed coatings were investigated by nano-indentation tests (**Figure 4.12**). Hardness (HIT) and the Young's modulus (EIT) of the coatings are in the range 3.3-5.3 GPa and 73-93 GPa, respectively. These values are in agreement with those reported for CaP coatings deposited with similar techniques [51]; however it must be noted that these properties strongly dependent on the porosity and the homogeneity of the coating. The presence of Sr²⁺ did not affect the mechanical properties of the as deposited coatings, since all coatings were amorphous. The annealing treatment improved the mechanical properties in terms of HIT only of the CaP and SrCaP films, while the values of EIT were comparable among the samples. Similar results have been reported by Dinda et al. [55] showing that the crystalline films

are more mechanically resistant and present higher hardness compared to the amorphous coatings but their Young's modulus remains analogous. Interestingly, the differences in HIT comparing the as-deposited and annealed samples were absent on the coatings contained higher quantity of Sr^{2+} (i.e. SrCaP2 and SrCaP3). This finding suggests that the re-arrangement of the material into a crystal structure upon a mild thermal treatment that leads to an improved HIT, was hindered when significant amounts of Sr^{2+} ions were present.

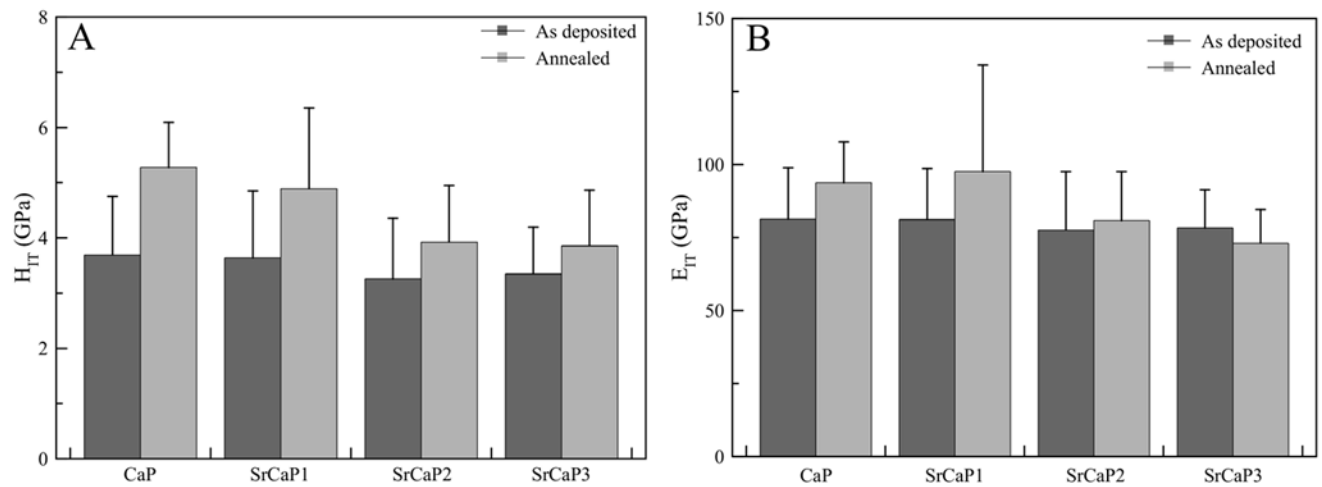


Figure 4.12. (A) Indentation hardness (HIT) and (B) Young's modulus (EIT) of the as-deposited and annealed coatings.

4.4. Conclusions

Herein we have investigated the feasibility to deposit nanostructured Sr^{2+} -doped CaP coatings onto PEEK substrates by PED. This mainly aims at improving the biological fixation with bone tissue and the long-term in vivo stability of PEEK implants especially in the case of osteoporotic patients thanks to the anabolic effect of Sr^{2+} . Targets composed of nanocrystalline HA doped with tailored amounts of Sr^{2+} ions from 0 up to 9 wt% were prepared and used for the coating deposition. Dense and uniform nanostructured amorphous CaP films having a Sr/Ca molar ratio very close to the Sr/Ca ratio of the targets were deposited at room temperature. The RMS and the wettability of the bare PEEK were significantly enhanced after coating deposition, achieving materials with potentially better biocompatibility and osseointegration properties. The presence of Sr^{2+} led to a slight increase of the size of the grains as well as of the RMS of the coatings that remained mainly composed of nanostructured aggregates. After a mild annealing treatment (130 °C for 6 h) – which did not compromise the physical-chemical properties of PEEK - amorphous CaP coatings converted into nanocrystalline Sr^{2+} -doped HA films having Sr/Ca molar ratios close to the ratios of the as-deposited films. The mild annealing treatment did not affect the topography and the roughness of the coatings, while the mechanical properties of the films un-doped and doped at low-extent improved only in terms of HIT. The data obtained here clearly show for the first time that PED is a reliable technique to deposit ion doped CaP coatings onto PEEK implants with a tuned amount of Sr^{2+} ions controlled by the stoichiometry of the target (i.e. in terms of Sr/Ca).

4.5. References

- [1] M. Franchi, M. Fini, G. Giavaresi, V. Ottani, Peri-implant osteogenesis in health and osteoporosis, *Micron* 36 (2005) 630-644.
- [2] P.J. Marie, Strontium as therapy for osteoporosis, *Curr. Opin. Pharmacol.* 5 (2005) 633-636.
- [3] W. Querido, A.L. Rossi, M. Farina, The effects of strontium on bone mineral: A review on current knowledge and microanalytical approaches, *Micron* 80 (2016) 122-134.
- [4] J.Y. Reginster, M.L. Brandi, J. Cannata-Andia, C. Cooper, B. Cortet, J.M. Feron, H. Genant, S. Palacios, J.D. Ringe, R. Rizzoli, The position of strontium ranelate in today's management of osteoporosis, *Osteoporos. Int.* 26 (2015) 1667-1671.
- [5] S.G. Dahl, P. Allain, P.J. Marie, Y. Mauras, G. Boivin, P. Ammann, Y. Tsouderos, P.D. Delmas, C. Christiansen, Incorporation and distribution of strontium in bone, *Bone* 28 (2001) 446-453.
- [6] N.D. Ravi, R. Balu, T.S. Sampath Kumar, Strontium-Substituted Calcium Deficient Hydroxyapatite Nanoparticles: Synthesis, Characterization, and Antibacterial Properties, *J. Am. Ceram. Soc.* 95 (2012) 2700-2708.
- [7] C. Capuccini, P. Torricelli, E. Boanini, M. Gazzano, R. Giardino, A. Bigi, Interaction of Sr-doped hydroxyapatite nanocrystals with osteoclast and osteoblast-like cells, *J. Biomed. Mater. Res. A*, 89A (2009) 594-600.
- [8] J. Gómez-Morales, M. Iafisco, J.M. Delgado-López, S. Sarda, C. Drouet, Progress on the preparation of nanocrystalline apatites and surface characterization: Overview of fundamental and applied aspects, *Prog. Cryst. Growth Charact. Mater.* 59 (2013) 1-46.

- [9] M. Iafisco, R. Bosco, S.C.G. Leeuwenburgh, J.J.J.P. van den Beucken, J.A. Jansen, M. Prat, N. Roveri, Electrostatic Spray Deposition of Biomimetic Nanocrystalline Apatite Coatings onto Titanium, *Adv. Eng. Mat.* 14 (2012) B13-B20.
- [10] E. Boanini, M. Gazzano, A. Bigi, Ionic substitutions in calcium phosphates synthesized at low temperature, *Acta Biomater.* 6 (2010) 1882-1894.
- [11] P. Johansson, R. Jimbo, Y. Naito, P. Kjellin, F. Currie, A. Wennerberg, Polyether ether ketone implants achieve increased bone fusion when coated with nano-sized hydroxyapatite: a histomorphometric study in rabbit bone, *Int. J. Nanomedicine* 11 (2016) 1435-1442.
- [12] S. Barkarmo, A. Wennerberg, M. Hoffman, P. Kjellin, K. Breiding, P. Handa, V. Stenport, Nano-hydroxyapatite-coated PEEK implants: A pilot study in rabbit bone, *J. Biomed. Mater. Res. A* 101A (2013) 465-471.
- [13] D. Almasi, S. Izman, M. Assadian, M. Ghanbari, M.R. Abdul Kadir, Crystalline ha coating on peek via chemical deposition, *Appl. Surf. Sci.* 314 (2014) 1034-1040.
- [14] A. Rabiei, S. Sandukas, Processing and evaluation of bioactive coatings on polymeric implants, *J. Biomed. Mater. Res. A* 101A (2013) 2621-2629.
- [15] P. Robotti, G. Zappini, Chapter 9 - Thermal Plasma Spray Deposition of Titanium and Hydroxyapatite on Polyaryletheretherketone Implants A2 - Kurtz, Steven M, in: *PEEK Biomaterials Handbook*, William Andrew Publishing, Oxford, 2012, pp. 119-143.
- [16] F. Suska, O. Omar, L. Emanuelsson, M. Taylor, P. Gruner, A. Kinbrum, D. Hunt, T. Hunt, A. Taylor, A. Palmquist, Enhancement of CRF-PEEK osseointegration by plasma-sprayed hydroxyapatite: A rabbit model, *J. Biomater. Appl.* 29 (2014) 234-242.

- [17] J.H. Lee, H.L. Jang, K.M. Lee, H.-R. Baek, K. Jin, K.S. Hong, J.H. Noh, H.-K. Lee, In vitro and in vivo evaluation of the bioactivity of hydroxyapatite-coated polyetheretherketone biocomposites created by cold spray technology, *Acta Biomater.* 9 (2013) 6177-6187.
- [18] J.W. Durham Iii, A. Rabiei, Deposition, Deposition, heat treatment and characterization of two layer bioactive coatings on cylindrical PEEK, *Surf. Coat. Technol.* 301 (2016) 106-113.
- [19] S.M. Kurtz, J.N. Devine, PEEK biomaterials in trauma, orthopedic, and spinal implants, *Biomaterials* 28 (2007) 4845-4869.
- [20] Y.-W. Du, L.-N. Zhang, Z.-T. Hou, X. Ye, H.-S. Gu, G.-P. Yan, P. Shang, Physical modification of polyetheretherketone for orthopedic implants, *Front. Mater. Sci.* 8 (2014) 313-324.
- [21] J.M. Toth, M. Wang, B.T. Estes, J.L. Scifert, H.B. Seim Iii, A.S. Turner, Polyetheretherketone as a biomaterial for spinal applications, *Biomaterials* 27 (2006) 324-334.
- [22] D.F. Williams, A. McNamara, R.M. Turner, Potential of polyetheretherketone (PEEK) and carbon-fibre-reinforced PEEK in medical applications, *J. Mater. Sci. Lett.* 6 (1987) 188-190.
- [23] J.Y. Rho, R.B. Ashman, C.H. Turner, Young's modulus of trabecular and cortical bone material: Ultrasonic and microtensile measurements, *J. Biomech.* 26 (1993) 111-119.
- [24] M. Niinomi, Mechanical properties of biomedical titanium alloys, *Mat. Sci. Eng. A* 243 (1998) 231-236.
- [25] M. Zhao, M. An, Q. Wang, X. Liu, W. Lai, X. Zhao, S. Wei, J. Ji, Quantitative proteomic analysis of human osteoblast-like MG-63 cells in response to bioinert implant material titanium and polyetheretherketone, *J. Proteomics* 75 (2012) 3560-3573.

- [26] K.B. Sagomonyants, M.L. Jarman-Smith, J.N. Devine, M.S. Aronow, G.A. Gronowicz, The in vitro response of human osteoblasts to polyetheretherketone (PEEK) substrates compared to commercially pure titanium, *Biomaterials* 29 (2008) 1563-1572.
- [27] R. Ma, T.T. Tang, Current Strategies to Improve the Bioactivity of PEEK, *Int. J. Mol. Sci.* 15 (2014) 5426-5445.
- [28] D. Almasi, N. Iqbal, M. Sadeghi, I. Sudin, M.R. Abdul Kadir, T. Kamarul, Preparation Methods for Improving PEEK's Bioactivity for Orthopedic and Dental Application: A Review, *Int. J. Biomater.* 2016 (2016) 12.
- [29] B.-D. Hahn, D.-S. Park, J.-J. Choi, J. Ryu, W.-H. Yoon, J.-H. Choi, J.-W. Kim, C.-W. Ahn, H.-E. Kim, B.-H. Yoon, I.-K. Jung, Osteoconductive hydroxyapatite coated PEEK for spinal fusion surgery, *Appl. Surf. Sci.* 283 (2013) 6-11.
- [30] D.M. Devine, J. Hahn, R.G. Richards, H. Gruner, R. Wieling, S.G. Pearce, Coating of carbon fiber-reinforced polyetheretherketone implants with titanium to improve bone apposition, *J. Biomed. Mater. Res. B* 101B (2013) 591-598.
- [31] C.-M. Han, E.-J. Lee, H.-E. Kim, Y.-H. Koh, K.N. Kim, Y. Ha, S.-U. Kuh, The electron beam deposition of titanium on polyetheretherketone (PEEK) and the resulting enhanced biological properties, *Biomaterials* 31 (2010) 3465-3470.
- [32] H.-K. Tsou, P.-Y. Hsieh, C.-J. Chung, C.-H. Tang, T.-W. Shyr, J.-L. He, Low-temperature deposition of anatase TiO₂ on medical grade polyetheretherketone to assist osseous integration, *Surf. Coat. Technol.* 204 (2009) 1121-1125.
- [33] C.-M. Han, T.-S. Jang, H.-E. Kim, Y.-H. Koh, Creation of nanoporous TiO₂ surface onto polyetheretherketone for effective immobilization and delivery of bone morphogenetic protein, *J. Biomed. Mater. Res. A* 102 (2014) 793-800.

- [34] T.J. Dennes, J. Schwartz, A Nanoscale Adhesion Layer to Promote Cell Attachment on PEEK, *J. Am. Chem. Soc.* 131 (2009) 3456-3470.
- [35] Y. Dmitry, N. Petr, G. Svetlana, E.K. Yakov, M. Giuseppe, A. Cosimo, B. Aldo, B. Ivano, T. Carlo, Characterization of Deposited Films and the Electron Beam Generated in the Pulsed Plasma Deposition Gun, *Jap. J. Appl. Phys.* 50 (2011) 08JD03.
- [36] R. Wan, M. Yang, Q. Zhou, Q. Zhang, Transparent conductive indium zinc oxide films prepared by pulsed plasma deposition, *J. Vac. Sci. Technol. A* 30 (2012) 061508.
- [37] E. Arisi, I. Bergenti, M. Cavallini, M. Murgia, A. Riminucci, G. Ruani, V. Dediu, Room temperature deposition of magnetite thin films on organic substrate, *J. Magn. Magn. Mater.* 316 (2007) 410-412.
- [38] M. Bianchi, M. Boi, N. Lopomo, M.C. Maltarello, F. Liscio, S. Milita, A. Visani, A. Russo, M. Maracacci, Nanomechanical characterization of zirconia thin films deposited on UHMWPE by pulsed plasma deposition, *J. Mech. Med. Biol.* 15 (2015) 1550070.
- [39] S. Gleizer, D. Yarmolich, J. Felsteiner, Y.E. Krasik, P. Nozar, C. Taliani, Electron beam and plasma modes of a channel spark discharge operation, *J. Appl. Phys.* 106 (2009) 073301.
- [40] J.E. Mathis, H.M. Christen, Factors that influence particle formation during pulsed electron deposition of YBCO precursors, *Phys. C Supercond.* 459 (2007) 47-51.
- [41] M. Boi, M. Bianchi, A. Gambardella, F. Liscio, S. Kaciulis, A. Visani, M. Barbalinardo, F. Valle, M. Iafisco, L. Lungaro, S. Milita, M. Cavallini, M. Maracacci, A. Russo, Tough and adhesive nanostructured calcium phosphate thin films deposited by the pulsed plasma deposition method, *RSC Adv.* 5 (2015) 78561-78571.

- [42] W.C. Oliver, G.M. Pharr, An improved technique for determining hardness and elastic-modulus using load and displacement sensing indentation experiments, *J. Mater. Res.* 7 (1992) 1564-1583.
- [43] E. Skwarek, Thermal analysis of hydroxyapatite with adsorbed oxalic acid, *J. Therm. Anal. Calorim.* 122 (2015) 33-45.
- [44] T. Kanno, J.-I. Horiuchi, M. Kobayashi, Y. Motogami, T. Akazawa, Characteristics of the carbonate ions incorporated into calcium-, partially-strontium-substituted and strontium apatites, *J. Mater. Sci. Lett.* 18 (1999) 1343-1345.
- [45] M. Iafisco, A. Ruffini, A. Adamiano, S. Sprio, A. Tampieri, Biomimetic magnesium–carbonate-apatite nanocrystals endowed with strontium ions as anti-osteoporotic trigger, *Mater. Sci. Eng. C Mater. Biol. Appl.* 35 (2014) 212-219.
- [46] J. Terra, E.R. Dourado, J.-G. Eon, D.E. Ellis, G. Gonzalez, A.M. Rossi, The structure of strontium-doped hydroxyapatite: an experimental and theoretical study, *Phys. Chem. Chem. Phys.* 11 (2009) 568-577.
- [47] A.R. Boyd, L. Rutledge, L.D. Randolph, B.J. Meenan, Strontium-substituted hydroxyapatite coatings deposited via a co-deposition sputter technique, *Mater. Sci. Eng. C Mater. Biol. Appl.* 46 (2015) 290-300.
- [48] Z.Y. Li, W.M. Lam, C. Yang, B. Xu, G.X. Ni, S.A. Abbah, K.M.C. Cheung, K.D.K. Luk, W.W. Lu, Chemical composition, crystal size and lattice structural changes after incorporation of strontium into biomimetic apatite, *Biomaterials* 28 (2007) 1452-1460.
- [49] J.D. Termine, A.S. Posner, Infra-Red Determination of the Percentage of Crystallinity in Apatitic Calcium Phosphates, *Nature* 211 (1966) 268-270.

- [50] J.V. Rau, M. Fosca, I. Cacciotti, S. Laureti, A. Bianco, R. Teghil, Nanostructured Si-substituted hydroxyapatite coatings for biomedical applications, *Thin Solid Films* 543 (2013) 167-170.
- [51] R.A. Surmenev, A review of plasma-assisted methods for calcium phosphate-based coatings fabrication, *Surf. Coat. Technol.* 206 (2012) 2035-2056.
- [52] G. Graziani, M. Bianchi, E. Sassoni, A. Russo, M. Marcacci, Ion-substituted calcium phosphate coatings deposited by plasma-assisted techniques: A review, *Mater. Sci. Eng. C Mater. Biol. Appl.* in press
- [53] Y. Lee, R.S. Porter, Double-melting behavior of poly(ether ether ketone), *Macromolecules* 20 (1987) 1336-1341.
- [54] N. Roveri, B. Palazzo, M. Iafisco, The role of biomimetism in developing nanostructured inorganic matrices for drug delivery, *Expert Opin. Drug Deliv.* 5 (2008) 861-877.
- [55] G.P. Dinda, J. Shin, J. Mazumder, Pulsed laser deposition of hydroxyapatite thin films on Ti-6Al-4V: Effect of heat treatment on structure and properties, *Acta Biomater.* 5 (2009) 1821-1830.
- [56] C. Ergun, H. Liu, T.J. Webster, E. Olcay, Ş. Yilmaz, F.C. Sahin, Increased osteoblast adhesion on nanoparticulate calcium phosphates with higher Ca/P ratios, *J. Biomed. Mater. Res. A* 85 (2008) 236-241.
- [57] Ballardini A., Ballardini G., Sangiorgi A., This is my family, *V.S.Ipp.*20, from .6j1989
- [58] I. Pereiro, C. Rodríguez-Valencia, C. Serra, E.L. Solla, J. Serra, P. González, Pulsed laser deposition of strontium-substituted hydroxyapatite coatings, *Appl. Surf. Sci.* 258 (2012).

- [59] C. Capuccini, P. Torricelli, F. Sima, E. Boanini, C. Ristoscu, B. Bracci, G. Socol, M. Fini, I.N. Mihailescu, A. Bigi, Strontium-substituted hydroxyapatite coatings synthesized by pulsed-laser deposition: In vitro osteoblast and osteoclast response, *Acta Biomater.* 4 (2008) 1885-1893.
- [60] A. Klymov, L. Prodanov, E. Lamers, J.A. Jansen, X.F. Walboomers, Understanding the role of nano-topography on the surface of a bone-implant, *Biomater. Sci.* 1 (2013) 135-151.
- [61] R.A. Gittens, L. Scheideler, F. Rupp, S.L. Hyzy, J. Geis-Gerstorfer, Z. Schwartz, B.D. Boyan, A review on the wettability of dental implant surfaces II: Biological and clinical aspects, *Acta Biomater.* 10 (2014) 2907-2918.

5. HIERARCHICALLY STRUCTURED BIOMIMETIC SCAFFOLD FOR REGENERATION OF LOAD BEARING BONES

5.1. Introduction

Multi-substituted apatite phases are widely recognized as the elective materials for bone tissue engineering approaches addressed to bone regeneration [1]. However, the development of biomimetic apatites in the form of 3-D massive scaffolds is still an open challenge and this substantially limits the possibility of developing bone substitutes with effective regenerative ability, particularly when it comes to treat load-bearing bones. In fact, to obtain bone regeneration bioactive scaffolds are claimed to provide a plethora of signals to cells, many of which are activated by fine compositional features such as specific ion doping in apatite lattice [2]. Additionally, a pore architecture enabling new bone penetration in the inner parts of the scaffold is needed also for sake of providing substantial vascularization which is mandatory for the new bone metabolism [3]. As highly porous materials have reduced mechanical properties, a smart pore architecture is required to maximize strength to withstand the early biomechanical loads. In this respect, bone tissue is characterized by multi-scale pore hierarchy, which provide bones with remarkable mechanical properties, in spite of their lightness, and ability to dissipate mechanical stresses down to the smallest bone trabeculae, where damages can be more easily repaired. Indeed, the self-repair ability of bone is also related to its hierarchical structure and there is

increasing evidence that such structure is relevant for activation of mechano-transduction phenomena at the basis of bone remodeling [4].

The fulfilment of all the above-reported requirements, simultaneously, is particularly critical when it comes to treat load-bearing bones and for this reason, in the lack of bone substitutes with the required bioactivity and morphological/mechanical features, the treatment of critical size, load-bearing bone defects is still a concern for orthopedic surgeons, and probably the most relevant challenge. Typical approaches in this respect are based on the use of metallic components (screws, plates) and pieces of cadaver bones to reconstruct the missing bone part. However, these components do not possess the required bioactivity to trigger substantial regeneration so that they can only act as physical sustains and consequently the patient is exposed to several possible complications and forced to repeated revision surgery [5]. Very often, the bone functionality is compromised and in a significant number of cases, when limb bones are involved, amputation must often be performed.

On this basis, material scientists are since long time engaged to find a solution to develop bone scaffolds exhibiting chemical, morphological and mechanical mimesis of bone tissue, simultaneously [6]. In this respect, ceramic materials have to be subjected to a thermal treatment (sintering) for physical consolidation with the scope of providing mechanical strength; in particular sintering temperatures for hydroxyapatite lie in the range 1150-1300 °C [7]. Unfortunately the elective materials for bone scaffolding, i.e. ion-doped apatite nanomaterials, are extremely labile when heated above few hundreds of degrees, as thermal energy tends to stabilize stoichiometric apatite phase and to segregate foreign ions outside the apatite lattice; on the other hand, as ion-doped apatites are calcium-deficient, secondary calcium phosphate phases form (typically tricalcium phosphate: $\text{Ca}_3(\text{PO}_4)_2$) so that the final material is a mixture of

stoichiometric apatite and tricalcium phosphate [8]. Therefore, thermal treatments destroy the fine chemical features that make synthetic apatite much closer to the bone mineral composition; additionally, at higher temperatures (i.e. above 1000 °C) surface reactions occur on the apatite nanoparticles, driving mass transfer to contact points among particles thus inducing particle coalescence and growth up to several microns. Simultaneously, due to this phenomenon the overall porosity is decreased and the ceramic body results well consolidated, with substantial rise of the mechanical strength, reducing at the same time the scaffold bioactivity. Indeed, even though technological progress experienced in the last decades enable the development of porous ceramics with good strength, their reduced surface activity and also the absence of an organized and pervious porosity hampered so far the achievement of full success in regeneration of large, load-bearing bone parts.

To overcome these limitations, some years ago Tampieri et al. [9] [10] proposed a completely new approach for scaffold synthesis, based on biomorphic transformation of natural structures endowed with pore architecture suitable for application as bone substitutes.

Biomorphic transformations consist in a sequence of heterogeneous reactions at the interface between a solid template and a reactant, carried out with the purpose of inducing phase transformation in the whole 3-D template but maintaining the original shape and microstructural features in the final material. The process was developed into six reactive steps, namely pyrolysis, carburization, oxidation, hydration, carbonation and phosphatization, carried out in a highly controlled fashion, in terms of temperature, atmosphere and reaction time, in order to accommodate the volume changes occurring in the solid body following compositional modifications, and thus to transform natural woods such as pine and rattan into final hydroxyapatite scaffolds retaining carbonation in B position, and multi-scale porosity very close

to the one showed by the original wood template. This achievement generated a new concept in biomaterials synthesis, as for the first time a nanocrystalline, ion-doped apatite was obtained in the form of a macroscopic 3-D solid body.

The new frontier in this respect is to obtain scaffolds of relevant size for real clinical applications. However, the careful control of all the parameters inherent in the various chemical reactions occurring during the different steps is a very hard challenge for materials scientists, particularly due to the need to cope with diffusive phenomena for which the various reactions should occur also in the bulk and not only at the template surface. For instance, during pyrolysis organic components, that in the case of wood are prevalently lignin and cellulose, decompose upon heating in absence of oxygen, thus leaving a scaffold made of pure carbon. When pyrolysis process is applied to bulk materials, the elimination of such products may cause structural damaging and disruption, with loss of mechanical strength, therefore pyrolysis process should be carried out by applying very slow thermal gradients. Another relevant example is the carbonation process, which is based on the reaction between a calcium oxide template and gaseous carbon dioxide, previous works highlighted that such process has limited success if carried out at low pressures or low temperatures, due to the formation of a surface layer of calcite that prevents further penetration of carbon dioxide into the bulk. For this reason the carbonation process can be very slow and even incomplete, if the bulk diffusion of the reaction product remains limited to the most superficial layers. Moreover, as the intermediate and final products are ceramic materials, their crystallinity and particle size are relevant parameters, besides composition, in determining chemical reactivity which in turn influences the reaction kinetics. More generally, when an intermediate product is obtained at lower temperatures, its crystallinity and grain growth is limited, thus resulting in increased reactivity during the subsequent process step.

With this in mind, the application of biomorphic transformation to large or less porous natural templates is not trivial and requires substantial investigation, control and optimization, of a plethora of simultaneously occurring phenomena. In this respect, the present chapter will describe the approaches by which this multi-step transformation process was optimized to yield biomorphic apatitic scaffolds in large size, adequate for real applications in bone surgery. In particular, each step of the process was thoroughly investigated and modified to achieve the desired phase transformation, whereas maintaining original shape and microstructural features, until the final achievement of nanocrystalline apatite presenting multiple ion doping and organized into a 3-D massive body exhibiting hierarchical pore organization and outstanding mimicry of the compact bone.

5.2. Materials and Methods

5.2.1. Scaffold production

Pyrolysis

The three-dimensional, highly oriented pore channel anatomy of native rattan (*Calamus manan*) were used as a template. The test were carried out using rattan canes, from different suppliers (signed B, C, F, G and N). The canes were cut to obtain hollowed cylinder with the following dimensions: outer diameter in the range of 30-50mm, an inner diameter in the range of 10-15mm and length in the range of 30-45mm. Then the samples were placed on inert refractory support, inside an horizontal split tube furnace (mark: Carbolite mod.: HST-12/600) suitable for pyrolysis process.

All the process is carried out under nitrogen flow atmosphere from room temperature up to high temperature (maximum 1200°C): the outlet gas was eliminated by exhaust smoke vent system.

The nitrogen flow rate inside the furnace was in the range of 1-3 l/min.

At the end of the process, the furnace was opened when room temperature was reached inside the process chamber.

The pyrolysed samples are extracted, measured all the dimensions by caliper and weighed in order to calculate the loss on ignition, the volume-loss and total porosity. The loss of ignition is calculated using the following equation:

$$LOI(\%) = ((W_{pre} - W_{post})/W_{pre})\%$$

where LOI(%) is the loss of ignition as percentage, W_{pre} is the initial weight and W_{post} is the final weight of the sample.

In addition, the micro- meso- macro- porosity of the pyrolysed samples is evaluated by SEM analysis and porosimetry. Accordingly to their diameter, the pores were divided into 3 different categories: micropores ($\varnothing = 1-20 \mu\text{m}$), mesopores ($\varnothing = 20-200 \mu\text{m}$), macropores ($\varnothing = 200-800 \mu\text{m}$).

Carburization

The carburization process converts carbon template into calcium carbide by reaction with metallic granular calcium (Sigma Aldrich, 99%) at high temperature and vacuum condition.

The pyrolysed sample are placed in a graphite crucible up the calcium source. The calcium amount was two times the stoichiometric need, to ensure the complete conversion of the carbon template.

The crucibles were inserted in a vacuum graphite furnace (mark: Pro.ba mod.: SINTER VF 800/S) by setting the thermal cycle up to about 1300°C. A pump (mark: Robuschi mod.: RBS-45/AV-V) has been connected to the furnace chamber to make vacuum inside.

At the end of the process, the furnace was opened when room temperature was reached inside the chamber. The carburized samples were extracted and analyzed. The samples were analyzed for: cracks formation, yield of reaction (weight variation), specific surface area (SSA), phase composition (XRD), total porosity and porosity distribution and crystal size and shape (SEM).

Oxidation

The carburized rattan templates has undergone an oxidation process at high temperature (over 1000°C) to be converted into calcium oxide.

The reaction was performed inside a tubular furnace (mark: Nabertherm mod.: RS 120/500/13) and checked by the use of a balance able to continuously weight the sample, placed on an alumina based refractory. The reaction was stopped by switch off of the furnace when the samples did not changed their weight anymore,.

When the furnace reached the room temperature, it was opened and samples were analyzed for: yield (weight variation), phase composition (XRD), crystal size and shape(SEM), and specific surface area, (SSA).

Hydration

Before the successive carbonation process, calcium oxide template was hydrated by immersion in a solution of 50ml of acetone (Sigma Aldrich, 98%) and water. The water amount was calculated to obtain the appropriate hydration yield (from 1 to 20% molar). The immersion time was 48h and then the acetone was evaporated in a vacuum chamber for 2 hours. Finally the samples were weighted to check the accordance between the final hydration and the calculated one.

Carbonation

Calcium carbonate template was obtained by carbonation of the calcium oxide at high temperature and CO₂ pressure. The samples were placed on inert refractory support and inserted inside a pressure-resistant reactor allocated in an horizontal split tube furnace (mark: Carbolite mod.: HST-12/600). All the process was carried out under carbon dioxide atmosphere: the internal pressure has been adjusted using an electronic pressure transmitter linked with a panel, able to adjust automatically the pressure inside the reactor.

At room temperature the furnace was opened and the sample was weighted in order to calculate the carbonation yield. The sample was evaluated for porosity, phase composition (XRD), crystal size and shape (SEM) and specific surface area (SSA)

Phosphatization

The chemical synthesis converting the calcium carbonate bodies into the final apatitic scaffold was carried out in hydrothermal condition at the following conditions 1,5M phosphate buffer solution (pH=7.5) obtained using an aqueous solution of Na₂HPO₄ and NaH₂PO₄ (Sigma Aldrich, analytical grade). The template was immersed in the solution and heated up to 200°C under a water vapor pressure for 72h.

In addition ion-doped apatitic scaffolds were obtained by following immersion of the carbonate substituted hydroxyapatite sample in an aqueous solution containing 0.5M Sr(NO₃)₂ and 0.5M Mg(NO₃)₂ salts for 24h.

5.2.2. Materials characterization

Phase composition

The phase composition of the product was obtained by X-ray diffraction (XRD) of the powders, by using a D8 Advance Diffractometer (Bruker Karlsruhe, Germany) equipped with a Lynx-eye position sensitive device using Cu K α radiation ($\lambda = 1.54178 \text{ \AA}$) generated at 40kV and 40mA. XRD spectra were recorded in the 2θ range from 20 to 60° 2θ with a counting time of 0.5s and a step size of 0.02°. XRD spectra elaboration through Rietveld full profile spectra analysis was conducted using TOPAS software v. 4.2.

Morphology evaluation

Field emission gun scanning electron microscopy (FEG-SEM) (Sigma NTS GmbH, Carl Zeiss, Oberkochen, Germany) was used to evaluate the morphology and the size of the apatite particles. Small pieces of the material were placed on an aluminum stub and covered with a thin layer of gold to improve conductivity before the analysis.

Porosity and pore distribution evaluation

Mercury porosimetry was used to evaluate pore size distribution (<50 μm) by two different apparatus (Carlo-Erba Porosimeter 2000 and Macropores Unit 120) working on separate pore size ranges. Density of porous bodies was measured by Archimedes' method (the so-called real density) and geometrical weight-volume evaluation (the so-called apparent density).

Specific Surface Area (SSA)

The specific surface area (SSABET) of the powders was measured by the Brunauer–Emmett–Teller (BET) gas adsorption method (Sorptly 1750, Carlo Erba, Milan, Italy).

Chemical composition analysis

The chemical analysis was performed on dried samples using ICP-OES spectrometer (Agilent 5100). About 20mg of hydroxyapatite was weighed and dissolved into 2ml of nitric acid (Sigma Aldrich 65 vol%) then diluted in 100ml of milliQ water. The solution was then analyzed using standard prepared from primary standards (1000ppm, Fluka). The analytical emission wavelengths were: Ca 422.673 nm, Mg 280.270 nm, Sr 421.552 nm and P 213.618 nm.

The evaluation of the carbonate content was made by thermogravimetric analysis (TGA) of dried samples, using a Stanton STA 1500 (Stanton, London, UK). About 10mg of the sample was weighed in an alumina crucible and heated from room temperature to 1100°C under nitrogen flow. The heating rate was 10°C/min. An empty alumina crucible was used as reference standard. The carbonate content was evaluated on the basis of the weight loss detected between 600°C and 1100°C [11].

Infrared spectroscopy was performed on the as-obtained powders, by using a Nicolet 380 FTIR spectrometer (Thermo Fisher Scientific Inc., Waltham, MA, US). The FTIR spectra were recorded in the wavelength range from 4000 to 400 cm^{-1} on small pellets obtained by mixing 1mg of the sample powder with 150mg of anhydrous potassium bromide (KBr). The mixture was pressed at 10t pressure into 7mm diameter disks. Before the acquisition of the FTIR spectra the disks were heated for a period of 24h at 100°C to expel the physically adsorbed water. A pure KBr disk was used as blank.

Evaluation of ion release

The evaluation of the ion release with time was made by immersing pieces of materials (1.5g of powder each) into 1l of pH=7.3 buffer solution (TRIZMA buffer, Sigma Aldrich) and maintained under shaking at 37°C. At scheduled times (i.e. after 6 hours, 1, 2, 3, 7 and 14 days) was removed 1ml of the solution for the analysis. The liquids containing the ions released after the prefixed

times were analyzed by ICP-OES for the quantitative determination of Ca, Mg, Sr and P. The results were presented as cumulative data. All the experiments were made in triplicate.

Mechanical Properties

The compressive strength of the materials was measured on particular cylindrical specimens 20 mm×14 mm (height×diameter) using a ZWICK; model Z050, with a crosshead speed of 1 mm/min. To avoid shear stress concentration, a thin foil was inserted between each end of the cylinder and the loading plates of the machine. The compressive strength was calculated from the maximum load registered during the test divided by the original area (six specimens were tested).

5.2.3. Biological evaluation

In vitro cell cultures

Mouse mesenchymal stem cells (C57BL/6 mMSCs, GIBCO) were used for the biological study. In detail mMSCs were cultured in DMEM Glutamax medium (Gibco) containing 10% Fetal Bovine Serum (FBS) and 1% penicillin-streptomycin (100 U/ml-100 µg/mL). The cell culture was kept at 37°C in an atmosphere of 5% CO₂. Cells were detached from culture flasks by trypsinization, centrifuged and re-suspended. Cell number and viability were assessed with the trypan-blue dye exclusion test.

Each sample (diameter 8.00 mm, height 4.00 mm), sterilized by 25 kGy γ -ray radiation prior to use, was placed one per well in a 24-well plate and pre-soaked in culture medium for 72 h at 37°C. S-HA scaffolds, already commercially available as bone grafts (Engipore, Finceramica Faenza SpA, Italy), were used as control group.

For the cell viability and cell morphology study, the samples were seeded by carefully dropping 20 µl of cell suspension (5.0×10^4 cells) onto the scaffold upper surface, and allowing cell

attachment for 20 min in the incubator, before the addition of 1 ml of cell culture medium (α MEM Glutamax Gibco, 10% FBS and 1% penicillin-streptomycin 100 U/ml-100 μ g/mL).

For the osteogenic gene expression profiling, the U-CUP perfusion bioreactor system (Cellec Biotek AG) was used. Briefly mMSCs were seeded at 2.0×10^6 cells/scaffold with a bidirectional flow rate of 3 ml/min for 18 h, then all the media were collected and the seeding efficiency was evaluated by counting the cells number left in the culture media after trypan-blue staining.

The cell-seeded constructs were then cultured with a bidirectional perfusion flow rate of 0.3 ml/min for additional 14 days [24].

The medium was changed twice a week. All the cell-handling procedures were performed in a sterile laminar flow hood. All cell-culture incubation steps were performed at 37°C with 5% CO₂.

Cell viability assay

Live/Dead assay kit (Invitrogen) was performed according to manufacturer's instructions. Briefly, the samples were washed with 1x PBS for 5 min and incubated with Calceinacetoxymethyl (Calcein AM) 2 μ M plus Ethidium homodimer-1 (EthD-1) 4 μ M for 15 min at 37°C in the dark, the samples were rinsed in PBS 1x [25]. Images were acquired by an inverted Nikon Ti-E fluorescence microscope (Nikon). One sample per group was analysed at day 1.

Cell morphology evaluation

One sample per group was used for fluorescence and SEM analysis at day 1 and day 3 of cell culture. In order to visualize actin filaments samples were washed with PBS 1x for 5 min, fixed with 4% (w/v) paraformaldehyde for 15 min and washed with PBS 1x for 5 min. Permeabilization was performed with PBS 1x with 0.1% (v/v) Triton X-100 for 5 min. FITC-conjugated Phalloidin (Invitrogen) 38 nM in PBS 1x was added for 20 min at room temperature in the dark [26].

Cells were washed with PBS 1x for 5 min and incubated with nuclear stain DAPI (Invitrogen) 300 nM in PBS 1x for 5 min. The nuclear morphological changes were also evaluated. Images were acquired by an Inverted Ti-E fluorescence microscope (Nikon).

For SEM analysis, after 1 day one sample per group was washed with 0.1 M sodium cacodylate buffer pH 7.4 and fixed in 2.5% glutaraldehyde in 0.1 M sodium cacodylate buffer pH 7.4 for 2 h at 4°C, washed in 0.1 M sodium cacodylate buffer pH 7.4 and dehydrated in a graded series of ethanol for 10 min each. Dehydrated samples were sputter-coated with gold and observed using Quanta Scanning Electron Microscope (ESEM Quanta 200, Fei).

Quantitative real-time polymerase chain reaction (q-PCR)

At day 14, cells grown on the MS-BIO-HA and the control samples, used as calibrator, were homogenized and total RNA extraction was performed by use of the Tri Reagent, followed by the Direct-zol™ RNA MiniPrep kit (Euroclone) kit according to manufacturer's instructions. RNA integrity was analysed by native agarose gel electrophoresis and quantification performed by the Qubit® 2.0 Fluorometer together with the Qubit® RNA BR assay kit, following manufacturer's instructions. Total RNA (500 ng) was reverse transcribed to cDNA using the High-Capacity cDNA Reverse Transcription Kit, according to manufacturer's instructions. Quantification of gene expression, using Taqman assays (Applied Biosystems), for Runt-related transcription factor 2 (Runx2, Mm01340178), Alkaline phosphatase (ALP, Mm00475834), Bone morphogenetic protein 2 (BMP2, Mm01340178), Osteopontin OPN, spp1 Mm00436767), Collagen 15 (Col15a1 Mm00456584) and glyceraldehyde 3-phosphate dehydrogenase, used as housekeeping gene, (GAPDH, Mm99999915) was performed by use of the StepOne™ Real-Time PCR System (Applied Biosystems). N. 4 scaffolds for each sample were analyzed, using three technical replicates for each experiment. Data were collected using the OneStep Software

(v.2.2.2) and relative quantification was performed using the comparative threshold (Ct) method ($\Delta\Delta Ct$), where relative gene expression level equals $2^{-\Delta\Delta C}$ [27].

Statistical Analysis

Results were expressed as Mean \pm SEM plotted on graph. Statistical analysis was made by two-way ANOVA analysis of variance using ΔCt value by the GraphPad Prism software (version 6.0), with statistical significance set at $p \leq 0.05$.

5.3. Study and optimization of the reaction kinetics related to controlled phase transformations in 3-D biomorphic templates

5.3.1. Pyrolysis

Pyrolysis is an irreversible thermochemical decomposition of organic matrix (i.e. resins, cellulose, hemicellulose, lignin, etc.) up to carbon phase at elevated temperatures in the oxygen-free environment (or any halogen).

During pyrolysis, the large molecules are undergone to very high temperatures leading high molecular vibrations. Every molecule in the wood sample is stretched and shaken to such an extent that large molecules starts breaking down into smaller molecules. H_2O , CO and CO_2 gases are released during the pyrolysis process.

A flux of inert gas (N_2) is used to maintain the inert atmosphere and push out residual gases produced by the wood decomposition.

At the end of this process, the wood is completely converted into a structure composed only by carbon (C). The final product of this process is a porous carbon template characterized by a

structure of amorphous graphite. Pyrolysed samples maintain microstructure and morphology of the native specimen despite this step is associated by an high weight loss and a huge volume shrinkage, both transversal and longitudinal directions.

5 different suppliers of canes (signed B, C, F, G and N) were selected for each test to minimize the influence of the natural structure variability on the statistical analysis of the results.

In order to set the critical parameters that influence structural characteristics of the materials (structure maintenance, cracks formation and shrinkage) and loss of ignition (LOI), two different parameters were optimized: 1) maximum temperature and 2) dwell time at the maximum temperature.

To evaluate the influence of the temperature on the pyrolysis, three tests were carried out at different higher temperatures (1000°C, 1100°C and 1200°C) by maintaining the same heating rates and varying the dwell time to obtain the same total time, considering heating and dwelling, (930 minutes) for all the processes, as shown in **Table 5.I.** The results obtained for each thermal cycle are summarized in **Table 5.II.**

Table 5.I.: Thermal cycles performed at different max temperature.

<i>Name</i>	<i>T</i> (°C)	<i>Heating</i> <i>rate</i> (°C/min)	<i>T</i> (°C)	<i>Heating</i> <i>rate</i> (°C/min)	<i>T</i> (°C)	<i>Dwell</i> <i>time</i> (min)	<i>Heating</i> <i>rate</i> (°C/min)	<i>T</i> (°C)	<i>Dwell</i> <i>time</i> (min)	<i>Total</i> <i>time</i> (min)
1000°C	25	10	350	2	500	120	1	1000	200	930
1100°C	25	10	350	2	500	120	1	1100	100	930
1200°C	25	10	350	2	500	120	1	1200	0	930

Table 5.II. Average loss of ignition, volume loss and porosity measured after treatment at different final temperature.

<i>Parameters/temperature</i>	<i>1000°C</i>		<i>1100°C</i>		<i>1200°C</i>	
	<i>average</i>	<i>error</i>	<i>average</i>	<i>error</i>	<i>average</i>	<i>error</i>
Volume loss	57,93%	2,07%	58,82%	1,42%	59,76%	2,00%
Loss of ignition	70,55%	1,13%	70,96%	1,04%	71,52%	0,78%
Pyrolised porosity	84,76%	1,62%	84,89%	1,58%	84,69%	1,46%

Considering expected performance of the final device, particularly important was the distribution of the pores, and if they are open or closed [12]. Three samples heated at different temperatures are observed by SEM (**Figures 5.1.**) to investigate morphology.

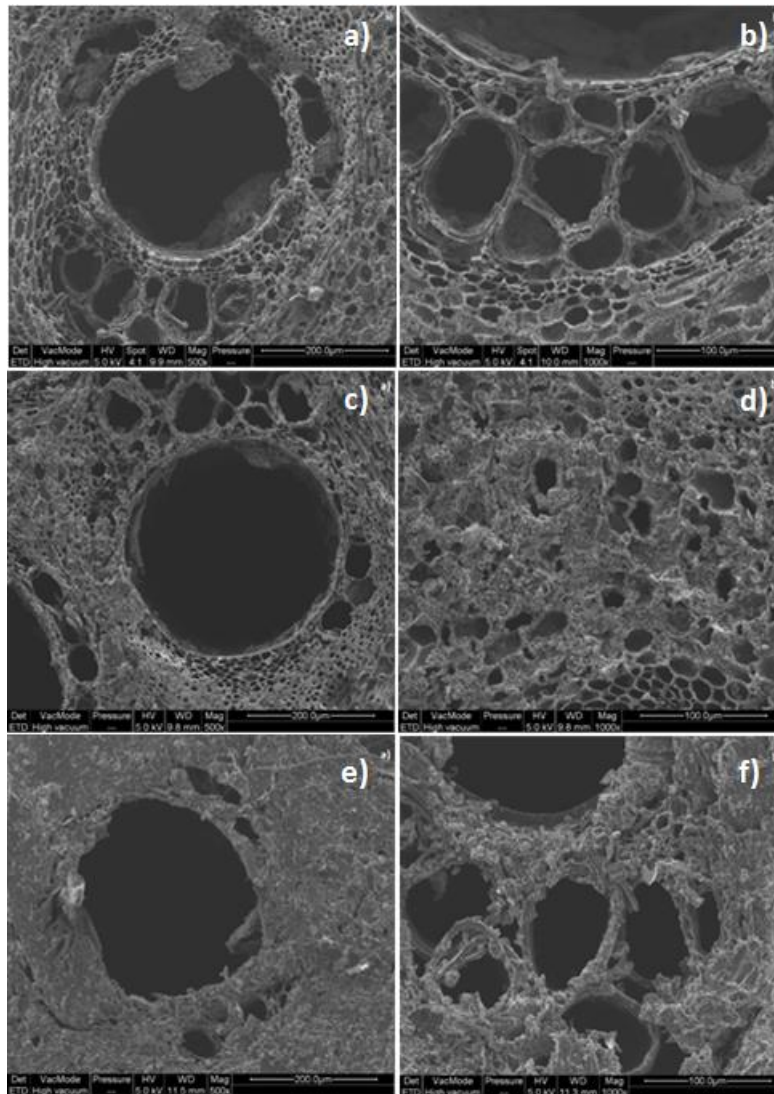


Figure 5.1.a-f. SEM Images of a pyrolysed Rattan at 1000°C (a,b), 950°C (c,d) and 1100°C (e,f) magnification 500x (a,c,e) and 1000x (b,d,f).

The identified pores can be divided into 3 different categories, according to their diameter: micropores ($\varnothing = 1-20 \mu\text{m}$), mesopores ($\varnothing = 20-200 \mu\text{m}$), macropores ($\varnothing = 200-800 \mu\text{m}$). After treatment at 900°C the microimages demonstrated the maintaining of the micro-, meso- and macro-pores. At 1100°C and 1200°C about 20% and 100% in volume of micropores disappeared

respectively, if compared with the sample treated at 1000°C. In addition at 1200°C also about 20% in volume of the mesopores are compromised (totally or partially closed).

Contrarily to the above observation other considered characteristics, total porosity, loss of ignition and volume loss (see **Table 5.II.**), were not affected by max temperature. On the basis of the these results 1000°C was chosen as maximum temperature for the pyrolysis.

At 1000°C the effect of the dwell time was studied.

Three thermal treatments were carried out with different dwelling time (200, 90 and 30 minutes) at 1000°C, as shown in **Table 5.III.** The temperature was raised up to 1000 °C following the heating cycle shown in **Table 5.I.** In order to define the effect of dwell time, differences on weight and volume loss and porosity were calculated (see **Table 5.III.**).

Table 5.III. Residual porosity, loss of ignition and volume loss after treatment for different dwell times at 1000°C.

<i>Dwell time (min)</i>	<i>Total time (min)</i>	<i>Residual porosity (%)</i>		<i>Loss of ignition (%)</i>		<i>Volume loss (%)</i>	
		<i>average</i>	<i>error</i>	<i>average</i>	<i>error</i>	<i>average</i>	<i>error</i>
200	930	84.76	1.62	70.55	1.13	57.93	2.07
90	820	84.98	1.54	70.41	1.23	57.52	1.85
30	760	81.54	1.77	66.38	1.05	53.17	1.99

By comparison of the results the sample treated for 200 and 90 minutes reached the same of residual porosity, loss of ignition and volume loss values while 30 minutes are not sufficient for the total thermal decomposition. The samples treated for 200 minutes and 90 minutes showed the same microstructure (pore dimension ranges and their distribution) after SEM observation. To

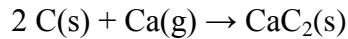
ensure the completion of the reaction avoiding an excessive and longer heating treatment of the material, the dwell time at 1000°C chosen for further experiments was 90 minutes.

In each of the two tests among the 5 supplier of canes were not revealed any significant difference in terms of loss of ignition, volume loss and final porosity.

5.3.2. Carburization

In the carburization process the carbon template from wood is completely transformed into calcium carbide, maintaining the initial structure and pore distribution.

The chemical reaction is given below:



In a previous article, Tampieri et al. [9], the carburization process was performed in inert gas flow and 1600°C in temperature, to allow the complete evaporation of calcium (> 1480°C). In this case, the final 3D specimen showed the disappearance of the pore dimensional range < 1 μm, due to excessive densification degree at high temperature.

In order to identically replicate the starting structure and maintain all its pore dimensional ranges, the reaction was carried out in vacuum condition (up to 100 mbar) to be able to minimize the calcium evaporation temperature, in according to the calcium vapor pressure curve, shown in **Figure 5.2.**

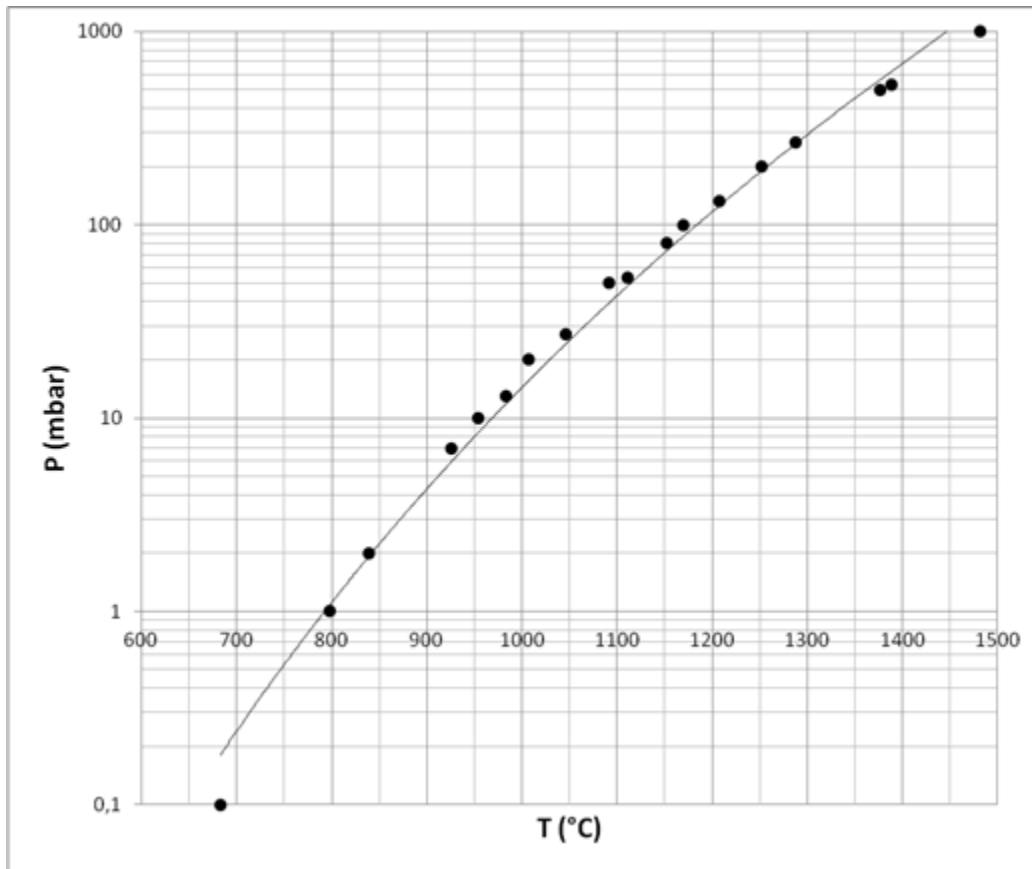


Figure 5.2. Calcium vapor pressure curve

An improved heating cycle was performed: an heating rate of 150°C/h up to 1200°C, 2h in dwell time and a cooling rate of 300°C/h, in argon atmosphere. The maximum temperature reached is far below the temperature of evaporation of calcium at room atmosphere (1484°C). When the temperature reached 900°C, a vacuum of 100mbar was created inside the furnace.

The average carburization yield obtained in the vacuum condition was $96.6 \pm 0.8\%$ (tested on 25 samples). The templates with a yield superior than 93.5% (23/25) did not presented cracks or deformations. Otherwise, the thermal expansion of significant carbon residual is incompatible with the carbide structure and causes its breaking.

The products were characterized by specific surface area (SSA), X-ray diffraction analysis (XRD), porosity, crystals size and shape (SEM).

The XRD spectrum (**Figure 5.3.**) showed phase composition of the carburized sample. It's composed only by pure CaC_2 (the Ca(OH)_2 peaks are due to partial transformation of CaC_2 in presence of humidity), both in the tetragonal and cubic crystalline form. In a previous work [9] the calcium carbide was obtained only in the tetragonal form, to demonstrate of the different temperature reached in the vacuum or flow treatment. The partial cubic form of CaC_2 could improve its conversion in cubic form of CaO , during the crystalline reorganization in the following oxidation step,

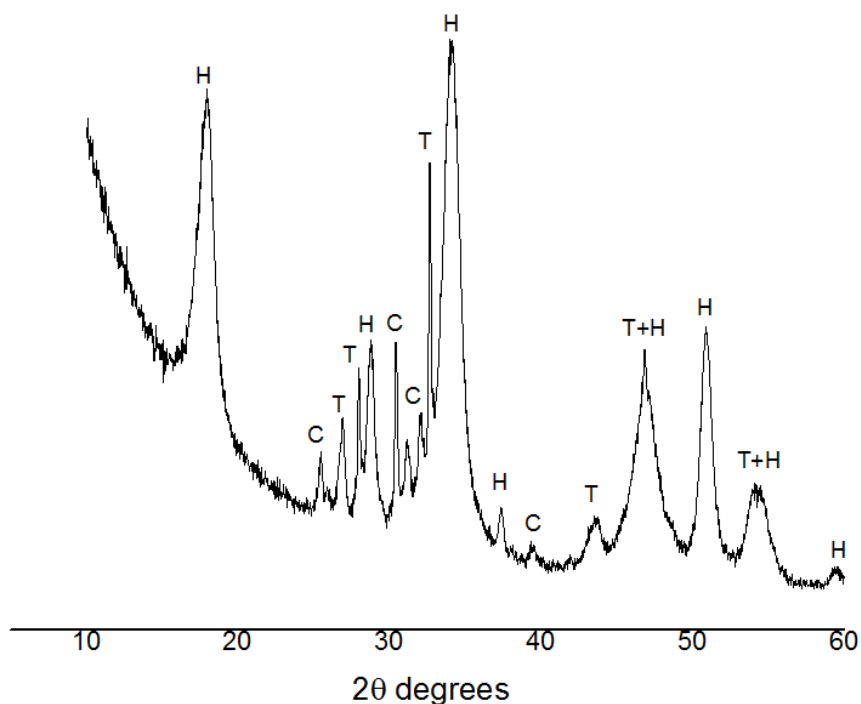


Figure 5.3. XRD spectrum of the calcium carbide with peaks attribution: C cubic calcium carbide, T tetragonal calcium carbide, H calcium hydroxide.

SEM images (**Figures 5.4.**) showed the preservation of micro-, meso- and macro-porosity in transversal (**Figures. 5.4.a-b.**) and longitudinal (**Figure 5.4.c.**). The images in **Figure 5.4.d.** showed the dimensions of the calcium carbide grains in the scaffold after carburization (in the

range of about 5-15 μm); they are an order of magnitude smaller than calcium carbide obtained in atmospheric pressure transformation.

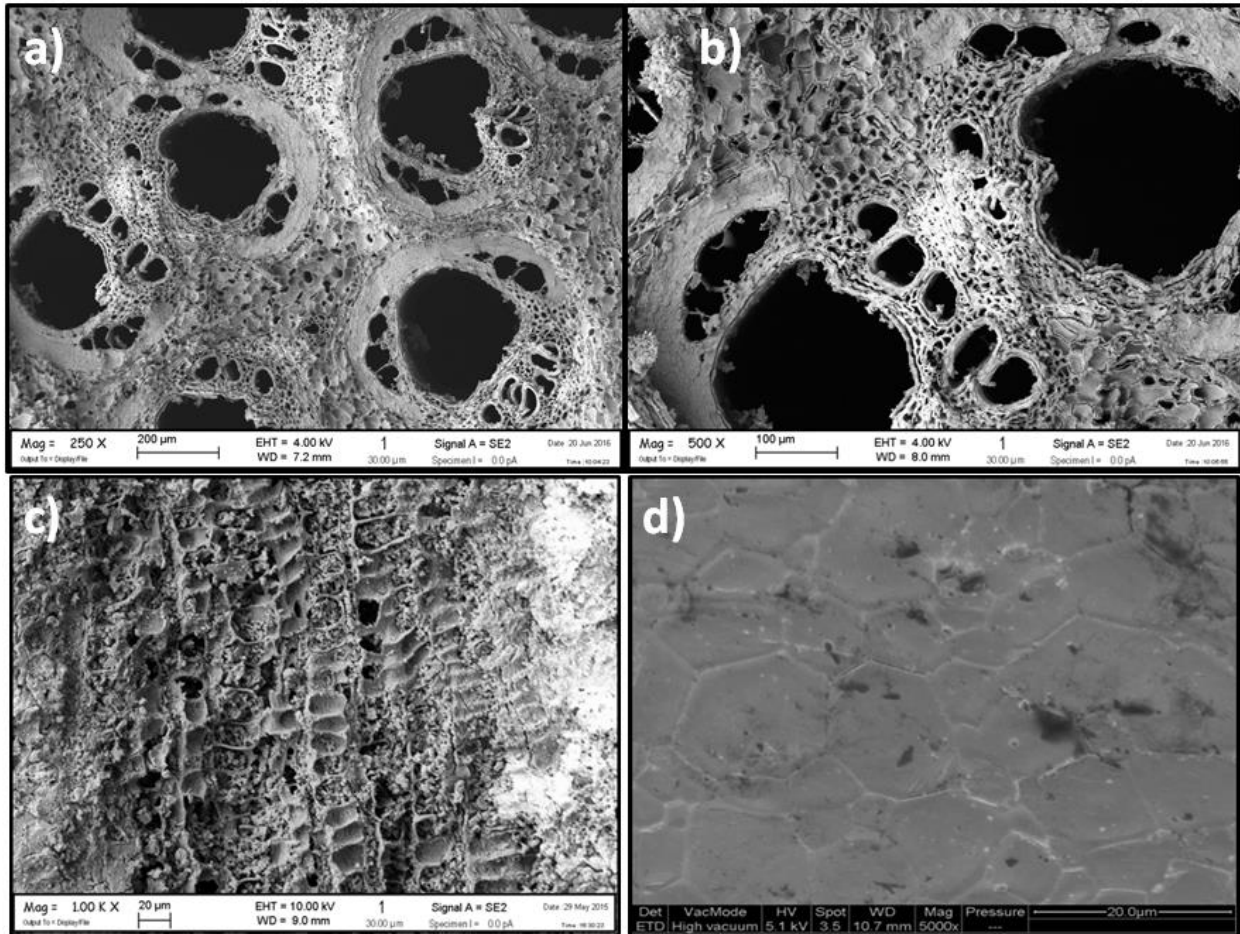


Figure 5.4.a-d. SEM images of the calcium carbide template with different magnification: a 250x, b 500x, c 1000x and d 5000x. **a-b-d** are transversal section while **c** is a longitudinal section. The vacuum conditions employed in the carburization step strongly reduced the defects and cracks that can be observed in the hierarchical pore structure of the calcium carbide.

In addition, the lower temperatures employed in the present disclosure prevent grain coalescence and excessive consolidation of the calcium carbide, which provoke structural distortion and deviations from the original microstructure of the starting wood, thus impairing the outcome of the following process steps. **Figure 5.5.** compares porosity between carbon template (starting)

and calcium carbide template (product) in the range of 0.01-40 μm . The data are presented as relative volume % of the porosity. The data confirm the maintaining of the same porosity range; only an half amount of the nanometric porosity (0.1-0.01) was lost in the calcium carbide template. Smallest pores could be plugged by residual of calcium entrapped in the structure or by the volume reduction (about 12%) associated to the process.

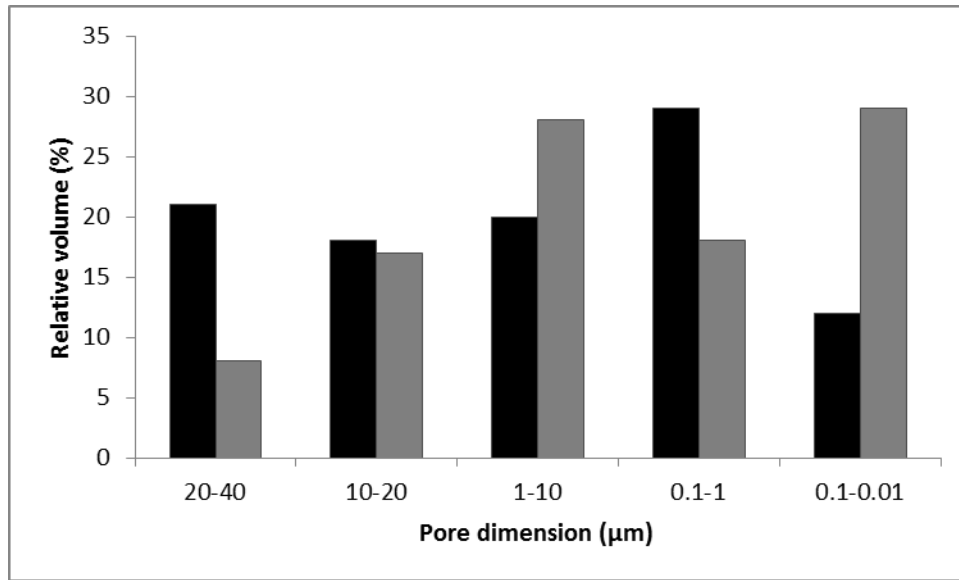
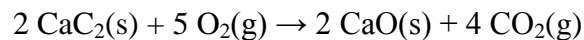


Figure 5.5. Comparison between Pores distribution of calcium carbide template (black) and carbon template (grey). Considered porosity range 0.01-40 μm

5.3.3. Oxidation

The oxidation step consist in the complete transformation of the calcium carbide in calcium oxide through a thermal treatment in air, maintaining the original structure and pore distribution.

The solid-gas reaction of this step is the following equation:



The reaction was performed in an air furnace, by using the oxygen of environment air as reactant. Different heating cycles were tested and a balance checked the weight loss of the sample during

the reaction. A complete reaction resulted after weight loss of about 12.5%. Ideal heating cycles had an heating rate of 5°C/min up to 300°C, 10°C/min up to 800°C/min and 2°C/min up to 1200°C with a dwell time of 30 minutes (total cycle time was 340 minutes). The heating cycle and the weight loss are showed in **Figure 5.6.**

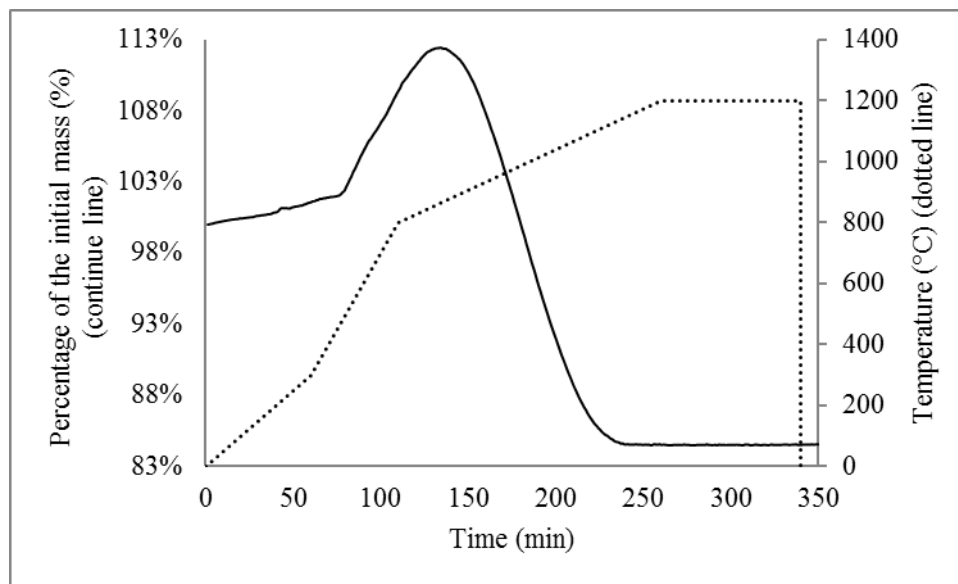
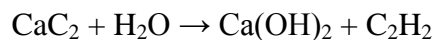
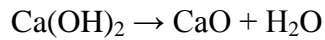
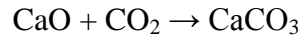
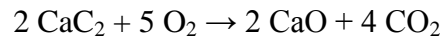


Figure 5.6. Monitoring of the reaction rate by weight percentage variation(continue line, primary axe) and heating rate (dotted line, secondary axe)

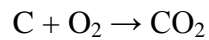
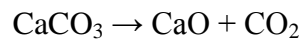
A first slight increment of the weight (within 80 minutes and 500°C) is due to the spontaneous hydration of calcium carbide with moisture, in according to the reaction:



From 80 to 130 minutes (in the range of about 500-800°C) the remarkable weight increase is of the sample due to the oxidation of calcium carbide and subsequent carbonation of the calcium oxide produced. At the same time the reaction with water stops and start the dehydration of calcium hydroxide.



From 130 minutes to 240, surpassing 850°C, the decarbonation reaction become more relevant than the carbonation, irreversible decarbonation occur when the temperature surpass 900°C, and continues the oxidation of the calcium carbide. In addition the possible residual carbon from a non-complete reaction in the previous passage are burned.



The heating cycle selected permit to reduce the increment of weight in the first part of the reaction, reducing the possible formation of cracks due to an initial absorption of carbon dioxide and a subsequent release of gas. The selected maximum temperature (1200°C) permit the completion of the reaction without presence of calcium carbonate, calcium carbide or carbon.

At the end of the cycle the obtained templates are completely white and maintain the original macrostructure, visible at naked eye, of the original wood.

The obtained calcium oxide template has been analyzed through XRD, to evaluate the phase composition, SEM, to evaluate the shape and dimension of the obtained particles, and specific surface area, to evaluate the reactivity of the material.

XRD shows that the obtained template is composed only of calcium oxide. The calcium hydroxide present in **Figure 5.7**. is the consequence of the partial hydration of calcium oxide due to water present in the air atmosphere during the analysis.

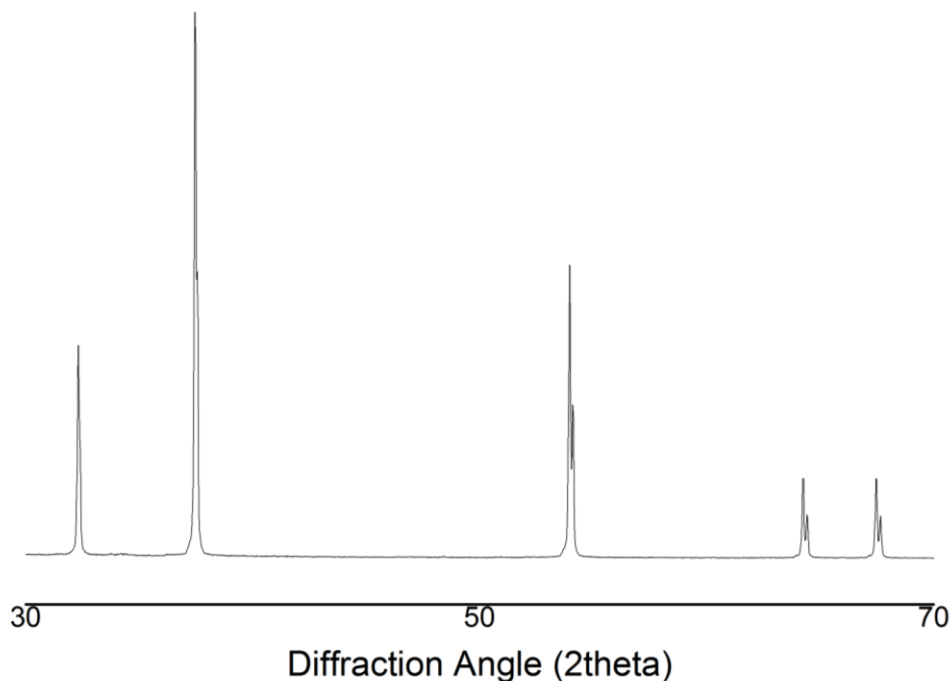


Figure 5.7. XRD spectra of the template after oxidation process. Diffraction 2θ angle 30-70

The specific surface area of the CaO is $9.56\text{m}^2/\text{g}$, higher than previous calcium carbide. From specific surface area is also possible to calculate the dimension of the particles using the formula:

$$6/(l*\text{density})=S$$

where: d is the density of the material, used $3.35\text{g}/\text{cm}^3$, l is the dimension of the particle in μm and S is the specific surface area in m^2/g . Using this formula, the calculated dimension of the particles is 187nm.

The SEM observation (**Figure 5.8.**) showed a not homogeneous matrix, composed by an high microporosity and various grain size dimension. The grains are rounded and have an average dimension of about 700 ± 84 nm. This difference between the value obtained with SSA is probably due to a great distribution of dimension or to an aggregation o particles not visible at SEM. In both cases was confirmed the submicrometric dimension of the particles.

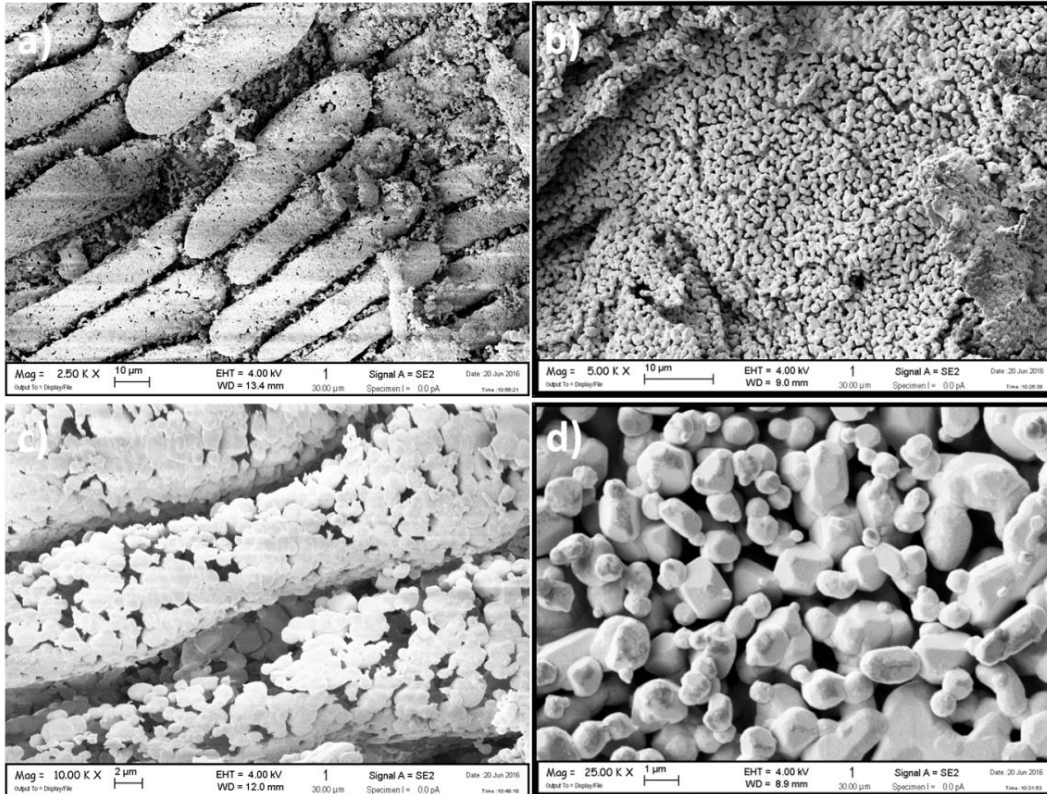


Figure 5.8.a-d. SEM images of the microstructure of the obtained CaO samples with different magnification: a) 2500x, b) 5000x, c) 10000x and d) 25000x.

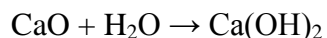
Figure 5.8.a, and **Figure 5.8.c.** show a detail of a longitudinal section of the material where the original structure, also in the microscale, is well preserved.

The aims of the oxidation step were reached because the template results completely transformed without cracks formation or residual phases, like carbon, cytotoxic, or calcium carbide, as visible

in **Figure 5.7.** The increase in the surface area results in an increase of the reactivity for the successive step. Furthermore submicrometric dimension of crystals and their lack of cohesion are positive factors, able to augment the reactivity of the material in the succeeding step.

5.3.4. Hydration

The partial hydration of CaO were carried out [13] to introduce an hydrated layer on the structure and facilitate the following carbonation process through a dissolution-reprecipitation reaction. Water reacts on the surface of CaO in according to the following equation:



permit a different reaction route to calcium carbonate, through hydroxide. Furthermore the dissolution-reprecipitation route for the reaction has the effect of reducing the crystal size of the obtained calcium carbonate. There are three important parameters in the reaction that must be controlled: 1) the time of hydration, 2) the dispersion of water and 3) total yield of reaction. The dispersion of water is important during the reaction is important to obtain a well dispersed calcium hydroxide matrix, improving the complete carbonation reaction in the following step. The reaction rate and the total hydration have to be controlled because a faster reaction or a too high hydration could result in cracks formation. The solution to optimize water dispersion, homogenize the reaction and improve penetration through the porosity is the use of a water/acetone mixture, where acetone was chosen because is more penetrating than other solvents, like ethanol, as dispersant for water. A volume of 50 ml of acetone is sufficient to immerse completely the sample and guarantee the dispersion of water. Another application of acetone is the control of the reaction rate. Dispersed water react slower than centered water,

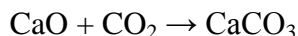
avoiding cracks formation. The quantity of water in the mixture determined the total yield of this step.

Another important aspect that need a fine control is the removal of residual acetone. When partially wet samples were used for carbonation results in cracked samples for the rapidity of evaporation of acetone during the heating cycle. To avoid the formation of cracks is necessary a complete evaporation of acetone before the successive step. To complete this procedure without heat treatment, the samples were placed in a vacuum chamber and left here for 48 hours, to complete the evaporation of acetone.

Different quantity of water inserted for hydration were tested, 1-2-5-7.5-10-15-20% molar compared to calcium oxide. 5% was resulted the higher hydration grade without superficial cracks formation and this value was selected as ideal for the hydration step.

5.3.5. Carbonation

The carbonation step transform the calcium oxide template in a product composed entirely of calcium carbonate in according to the following overall reaction:



The complete conversion of CaO into CaCO₃ is necessary to avoid the collapse of the structure during the last phosphation process in hydrothermal conditions. In fact when large amount (>5%) of CaO remain inside the template, its conversion into calcium hydroxide (Ca(OH)₂) causes the breaking of the structure because calcium hydroxide solubility in water is higher ($K_{sp}=5.5 \cdot 10^{-6}$). Respect to calcium carbonate ($K_{sp}=3.7 \cdot 10^{-9}$) and the reaction will occur slowly.

To obtain the conversion of the template into calcium carbonate it is necessary to treat it at high temperature under pressure of CO₂. An high pressure specific reactor was realized for this treatment.

When CO₂ is over its critical temperature (31.10°C) comprimed over critical pressure (72.9 atm) it becomes a supercritical fluid (see **Figure 5.9.**). A supercritical fluid is an gas-liquid phase, maintaining part of the properties of the gas phase, like penetration of solids or expansion in all the available volume, and part of the properties of the liquid phase, like density or dissolution ability

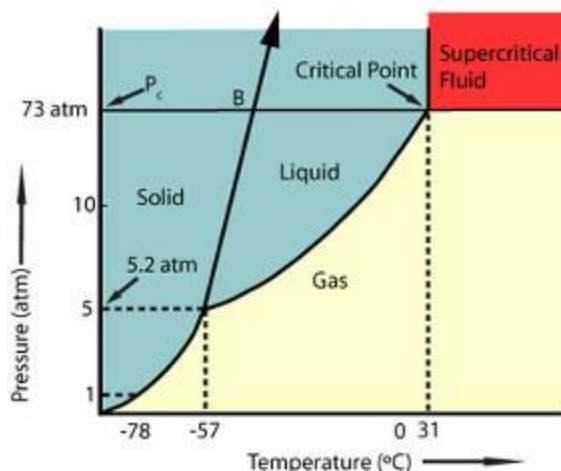
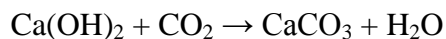


Figure 5.9. Physical state for carbon dioxide in function of pressure and temperature.

The properties of the supercritical fluid are exploited for the carbonation reaction in fact the previous step of hydration permit a different mechanism respect to a direct gas-solid carbonation. When the temperature is above 480°C the carbon dioxide start to react with calcium hydroxide, and release water (see equation below).



The released water was then dissolved by the supercritical fluid, it can penetrate the sample and act as a catalyzer of the reaction. The process in supercritical condition can be summarized by the following step. An aqueous layer was produced on the sample and CaO is not directly converted into CaCO₃ but transformed in Ca(OH)₂. Then the Ca(OH)₂ is dissolved by the aqueous layer into Ca²⁺ ions that precipitate in CaCO₃ form. This reaction mechanism influences the process up to about 600°C. At higher temperature the dehydration of calcium hydroxide becomes irreversible and CaO could not be transformed into Ca(OH)₂ anymore. At temperature superior than 620°C the direct reaction between CaO and CO₂ is predominant. The heating of the samples at temperature above 600°C is useful to increase the dissolution-reprecipitation of the crystals and the reaching of the complete conversion.

Another important effect of water during the carbonation process is the capacity of forming crystals and pores characterized by small dimensions. In fact water converts part of the CO₂ into carbonic acid (H₂CO₃) able to dissolve calcium carbonate in the aqueous layer, in a process of dissolution-reprecipitation. The re-precipitation is a crucial step to obtain calcium carbonate crystals smaller than the initial ones and less adherent each other if compared with the product obtained by gas-solid reaction, increasing the microporosity of the material and the reactivity for the final step. Furthermore the bigger dimension of the crystals obtained without hydration compromise the structural integrity of the template during the successive final step of phosphation, while smaller crystals could reinforce the structure, increasing the specific surface and consequently the number of interactions between grains with the possibility of rearrangements of the structure without crack formation.

In the optimized thermal cycle the carbon dioxide pressure was maintained at 100atm, over the critical pressure and the temperature was slowly increased. The heating cycle was set at 10°C/min up to 400°C, 2°C/min up to 500°C, dwell time of 30 minutes, 2°C/min up to 600°C, dwell time of 1 hour and 0.5°C/min up to 800°C, dwell time of 2 hours.

The final templates had an average yield (calculated by weight increase) of 97.3% ± 1.2%, an average density of 1.01 g/cm³ and a calculate total porosity greater than 60%.

XRD pattern (**Figure 5.10**). confirm that calcium carbonate, in the polymorph crystal form of calcite, was the predominant species (CaO trace can be also observed). Other forms of calcium carbonate, vaterite and aragonite, are not present because are not stable at high temperature (above 470°C) [14].

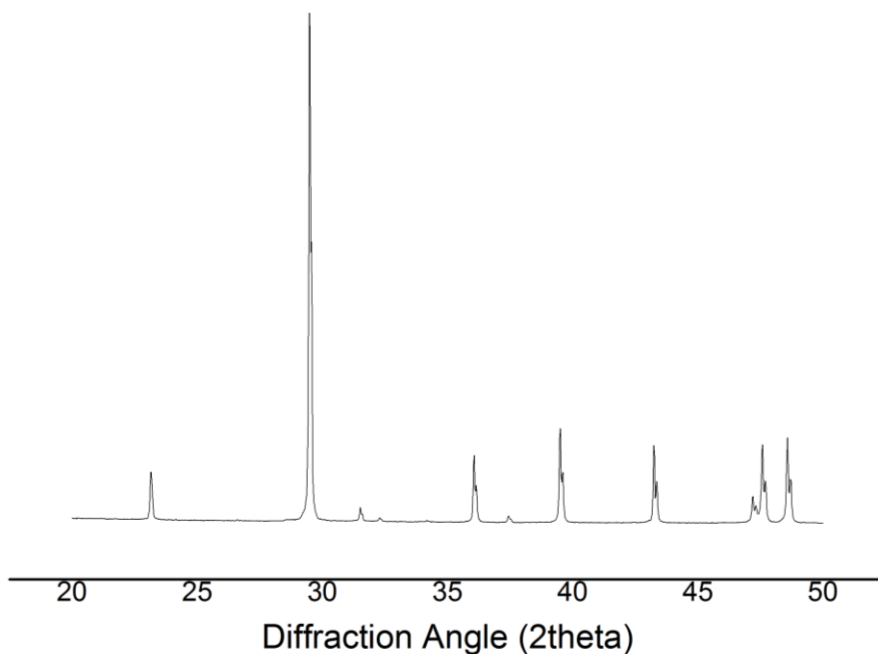


Figure 5.10. XRD spectra of the calcium carbonate template from 20 to 50 of diffraction angle

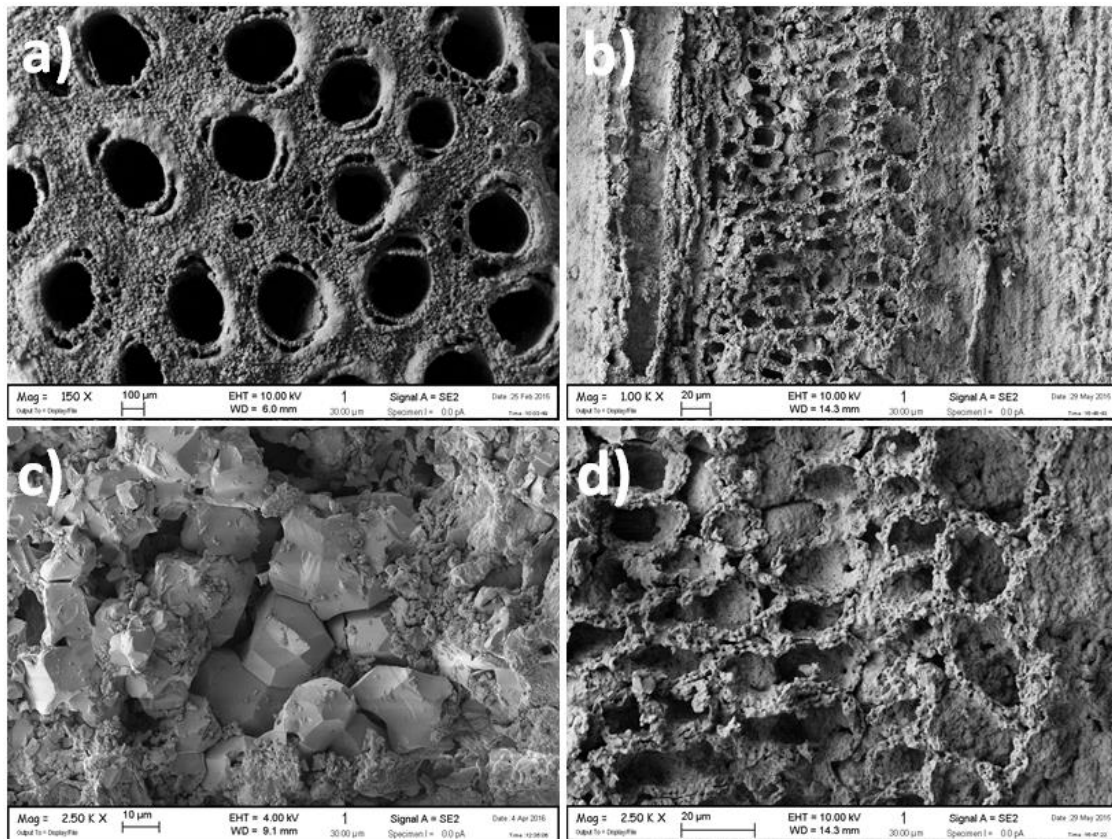


Figure 5.11.a-d. SEM analysis of CaCO₃ template obtained after partial hydration (**a-b-d**) or without hydration (**c**) at various magnification, **a** 150x, **b** 1000x, **c** 2500x, **d** 2500x.

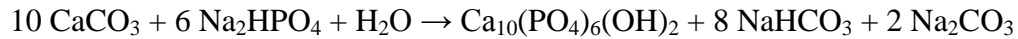
SEM analysis (**Figure 5.11.**) was performed to verify the maintenance of the original structure and comparing the microstructure of CaCO₃ obtained by dissolution-precipitation and solid-gas process. The SEM analysis (**Figure 5.11.a-b.**) confirm that macrostructure is maintained both in the transversal (**a**) and longitudinal (**b**) planes. The images **c** and **d** instead confirm that the crystals obtained with previous hydration are of smaller dimension.

Also the analysis of the specific surface area is interesting for the comparison between CaCO₃ obtained by dissolution-precipitation and solid-gas process. The specific surface area of the sample obtained by hydration approach was 9.60m²/g while the specific surface area of the

samples obtained without previous hydration was 6.28 m²/g. The dimension of the crystallites, obtained using a density for the calcite of 2.711g/cm³, are of 230nm and 352 nm respectively.

5.3.6. Phosphatization

The obtained templates made of calcium carbonate have to be transformed into calcium phosphates. The conversion of calcium carbonate into hydroxyapatite occurs through a reaction of dissolution-precipitation, drive by the different Kps of calcium carbonate ($3.7 \cdot 10^{-9}$) and hydroxyapatite (10^{-58}). The process follow the subsequent reaction:



Obviously the reaction could occur through different ionic species because it occurs in water and sodium salts are easily soluble. The pH has been set to 7.5 considering the solubility phase diagram Ca(OH)₂-H₃PO₄-H₂O at 25 °C [15] and solubility curves of calcium orthophosphoric compounds at 37°C, depending on pH in aqueous solution [16]. (see **Figure 5.12**)

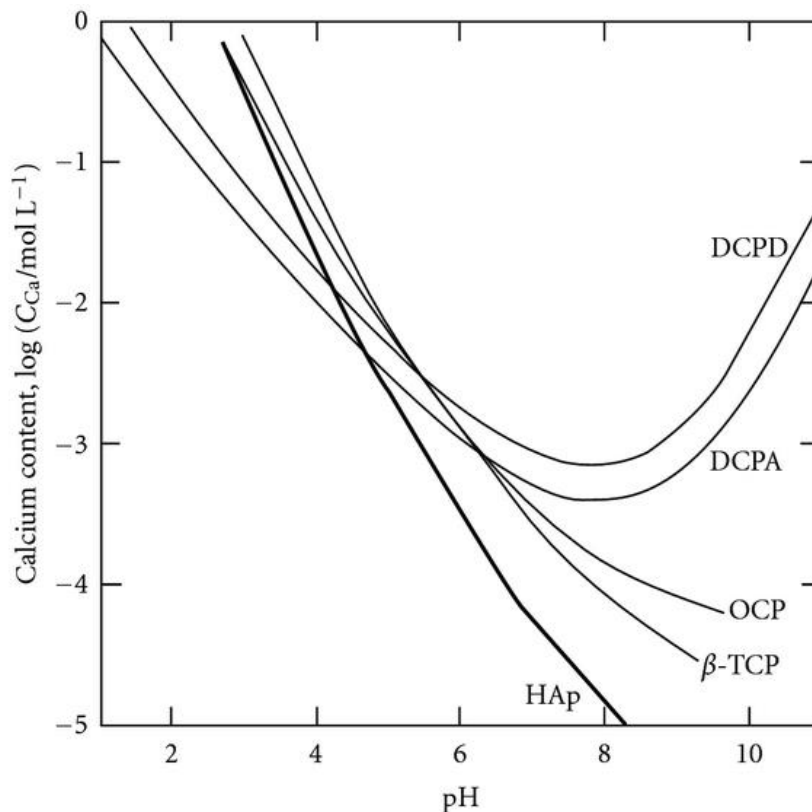


Figure 5.12. Solubility curves of calcium orthophosphoric compounds at 37°C, depending on pH in aqueous solution. HAp: hydroxyapatite, TCP: tricalcium phosphate, OCP: octacalcium phosphate, DCP: dicalcium phosphate (A: anhydrous, D: dihydrated)

The template was immersed in the phosphate solution and then heated to a temperature of 200°C under a water vapor pressure for 72h. Considering the presence of carbonate ions in the reaction vessel the precipitated hydroxyapatite undergoes to a spontaneous carbonation. When the reaction is concluded the reactor was opened, the samples washed with abundant distilled water and eventually treated for ionic substitution. The carbonate substituted hydroxyapatite samples were immersed in an aqueous solution containing 0.5M $\text{Sr}(\text{NO}_3)_2$ and 0.5M $\text{Mg}(\text{NO}_3)_2$ ions for 24h. Ionic substitution is useful to introduce relevant ions for cells activation, like Mg and Sr. The substitution occurs partially with ions exchange between ions rich solution and the materials, for the doping of the HA crystals, and partially through dissolution-reprecipitation of the material. In

this case the calcium phosphate deposited is β -TCP, more stable in presence of Mg and at lower pH (6). A large number of studies present a biphasic calcium phosphate HA/TCP with a ratio of 70/30 the golden standard for regeneration [17].

5.4. Characterization of the final apatitic scaffold

5.4.1. XRD analysis

X-ray diffraction patterns in **Figure 5.13.** show that the obtained biomorphic materials were made of pure HA phase, in absence of any introduced doping agent, and a mixture of nanocrystalline HA and β -TCP (evaluated as 76:24 wt%) in the ion-doped material, in agreement with the JCPDS cards: 09-0432 and 09-0169, respectively [18] [19]. No other crystalline phases were detected by XRD analysis.

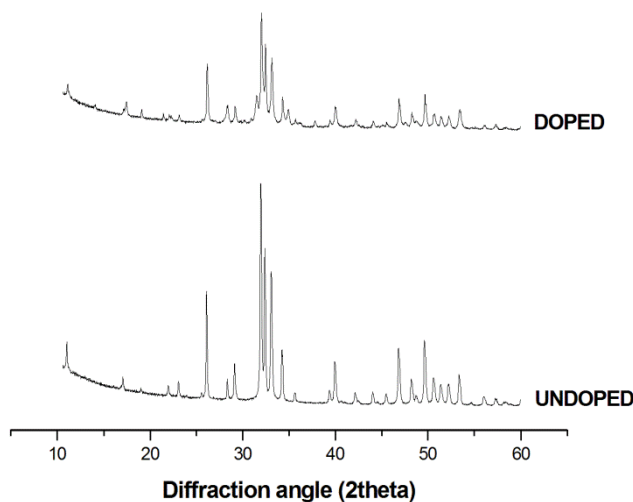


Figure 5.13. XRD pattern of the as-obtained biomorphic scaffolds. a): undoped HA; b): doped HA.

The full profile analysis of the XRD spectra revealed a slight deformation of the HA crystal, as induced by the ion doping (**Table 5.IV.**). Particularly, a slight increase of both a and c cell

parameters was detected, in comparison with the undoped HA, thus yielding HA cell volume expansion without, however, inducing a significant anisotropic deformation of the HA lattice. The XRD patterns of both the obtained materials revealed broad diffraction peaks ascribed to small crystalline domains size, which were evaluated as 91 ± 1 and 66 ± 1 nm for undoped and doped hydroxyapatite phase, respectively. On the other hand, the analysis of peak broadening in β -TCP phase reported on a domain size of 45 ± 1 nm.

Table 5.IV. Crystal data on the as-obtained biomorphic materials.

	a (Å)	c (Å)	<i>Cell volume</i> (Å ³)	c/a	D_{av}
Not doped	9.44735(2)	6.89215(8)	532.7(3)	0.729	91 ± 1
Doped	9.45556(6)	6.90038(7)	534.3(0)	0.730	66 ± 1

5.4.2. Chemical composition

In association with XRD analysis, effective ion doping in biomorphic HA was assessed by elemental analysis that reported on the presence of ≈ 4 and ≈ 1 mol% of magnesium and strontium, respectively, in respect to calcium (**Table 5.V.**). The replacement of calcium with these foreign ions was confirmed by the reduced Ca/P ratio, in comparison with the typical value of stoichiometric HA (i.e. Ca/P = 1.67). The low Ca/P detected also in the non-doped HA could be ascribed to the occurrence of calcium vacancies, following the incorporation of carbonate ions in the HA structure. This hypothesis is supported by evaluation of the FTIR absorption spectra reported in **Figure 5.14.**, where the typical bands belonging to the apatite phase are shown, together with absorption bands at 1430cm^{-1} typical of B-site carbonation (i.e. in the PO₄ crystal site) [20]. In this respect, FTIR spectra highlight that carbonation occurred by replacement of PO₄

functional groups, i.e. in B position, as reported by the presence of absorption bands at 870, 1430 and 1450 cm^{-1} in both the final biomorphic materials.

Table 5.V. Chemical analysis of the produced materials

	<i>Ca/P</i>	<i>Mg/Ca</i> (mol%)	<i>Sr/Ca</i> (mol%)	<i>cations/PO₄</i>	<i>CO₃</i> (wt%)
Doped	1.55	3.89	0.97	1.62	2.56
Not doped	1.62	---	---	1.62	2.12

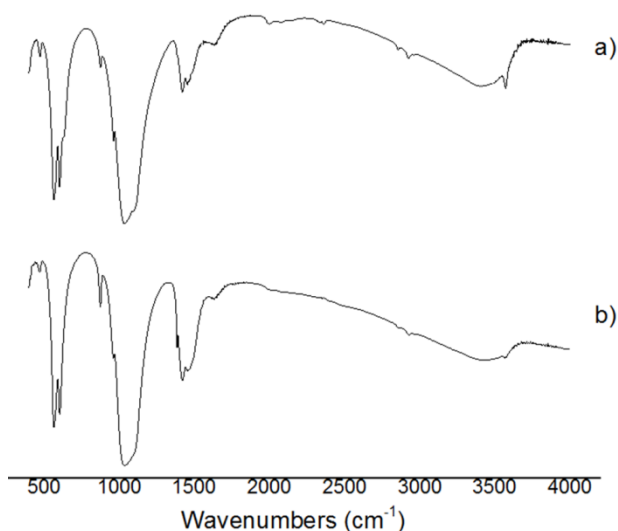


Figure 5.14. FTIR spectra of biomorphic scaffolds. a): undoped; b): doped.

5.4.3. Microstructure

Figure 5.15.a-f. shows SEM micrographs of rattan woods after pyrolysis and after complete transformation into hydroxyapatite. The pyrolysis process, carried out by very slow temperature gradients allowed to maintain a wide open porous morphology with nanostructured details reproducing the original cell wall architecture of the native plant (**Figures 5.15.a, b.**).

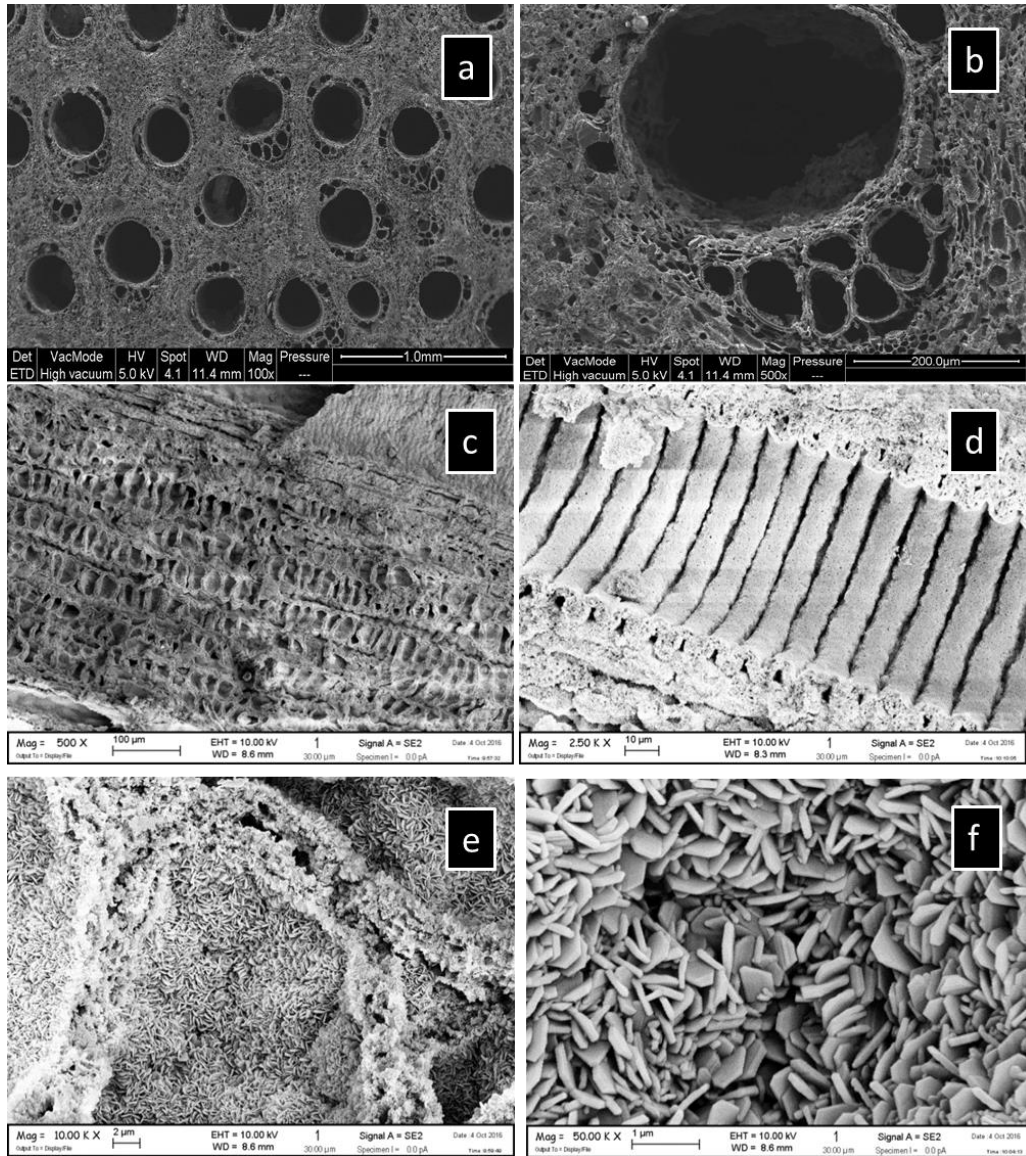


Figure 5.15.a-f. SEM analysis of biomorphic materials. a): structure of pyrolysed wood with b): details at the micron size; c-f): structural details of final MS-BIO-HA scaffolds at the multi-scale. The confirm that the whole transformation process, including intermediate steps forming biomorphic CaO and CaCO₃ ceramics, was carried out with careful control of the process parameters, is the maintenance of the original hierarchical structure at the multi-scale, exhibiting open, pervious channels interconnected with smaller pores and channels. At the lower scale, biomorphic HA appear formed by prismatic nanocrystals with hexagonal-like shape typical of

HA phase, typical for hydrothermal conversion of calcite into HA [21]. The dimension of the obtained nanocrystal, measured by SEM analysis, is about 200nm, very low if compared with a HA sintered at 1250°C, about 1700nm [22]. Furthermore the obtained grains are less compact than sintered ones.

5.4.4. Specific surface area (SSA)

The specific surface area of the obtained sample is very high, 9,96 m²/g. From specific surface area is also possible to calculate the dimension of the particles using the formula:

$$6/(l * density) = SSA$$

where: *d* is the density of the material, used 3.16g/cm³, *l* is the dimension of the particle in μm and SSA is the specific surface area in mm²/g. Using this formula, the calculated dimension of the particles is 190nm, coherent with the one obtained by SEM analysis.

5.4.5. Porosity

The total porosity of the obtained sample is high, calculated between 57,2±1.4% using density of hydroxyapatite equal to 3.16g/cm³. The distribution of the porosity is divided in three big ranges of dimension, as it is possible to see in **Figure 5.16.**

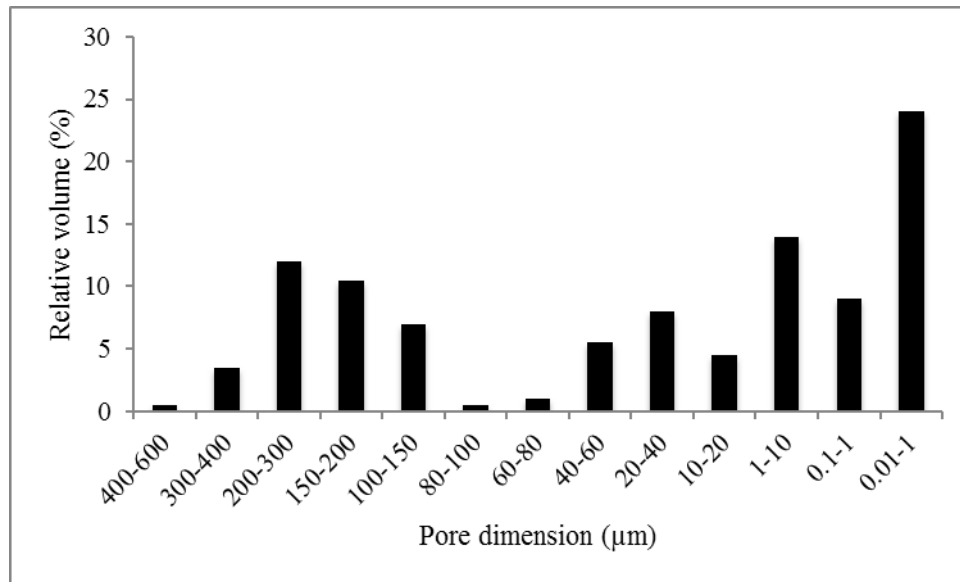


Figure 5.16. Analysis of pore distribution as volume of pore in a completely transformed template

A first group, between 100 and 600 µm, consider the macroporosity of the sample and totals 33.5% of the pore volume. This porosity is useful, during the use as implant, for cells colonization of the inner part of the material and for angiogenesis. A second group, between 100 and 10µm, called mesoporosity and consider the small canals that run along the bigger ones. It is not very important for bioresorbability because is too small for cell passage, cell dimension is superior to 100µm, but is useful for introduction of big volumes of liquids inside the scaffold. It totals only 19.5% of the total pore volume. A third group, the microporosity, between 0.01 and 10µm, is extended and well branched. Differently from the porosity of larger size, microporosity extends not only longitudinally but also transversely. It span through all the volume of the material and favors liquids distribution in the whole scaffold. It totals 47% of total pore volume.

5.4.6. Mechanical properties

The uniaxial compression tests provide a simple and effective way to characterize a material's response to loading. By subjecting a sample to a controlled compressive displacement along a single axis, the change in dimensions and resulting load can be recorded to calculate a stress/strain profile. From the obtained curve, elastic and plastic material properties can then be determined.

The compressive strength of scaffolds is an important bio-engineering consideration. When using porous structures for tissue engineering scaffolds, the structure must retain sufficient mechanical properties to fulfil the requirements of structural integrity once implanted in host tissue.

In uniaxial compression the forces are directed along one direction only, so that they act towards decreasing the object's length along that direction.

The sample need a length/diameter ratio in the range of 1.0-1.5, to avoid the direction of the forces along different directions.

The load versus displacement curve have been drawn from the start of the test to the fracture of the test specimen and the maximum load from each load versus displacement curve have been recorded.

The compressive strength of the specimen (σ) is calculated by dividing the maximum load attained during the test (L) by the cross-sectional area of the specimen (A), according to following formula:

$$\sigma_i = L_i / A_i$$

where: σ_i is the compressive strength of the i-specimen (MPa), L_i is the maximum load in each test (N), A_i is the compressive area of i-specimen (mm^2)

The maximum load (L) in each specimen is evaluated through the Load/Deformation diagram.

Le curve si possono vedere in **Figure 5.17**.

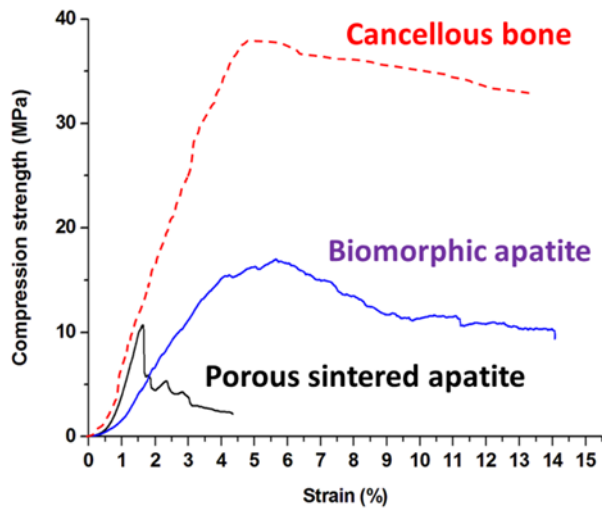


Figure 5.17. Load/Deformation diagram for three different material. Red: cancellous bone, blue biomorphic apatite, black: porous sintered apatite.

The scaffolds composed of biomorphic apatites have a maximum load (17.3MPa) superior than the one of scaffold made of sintered HA with comparable porosity (10.2MPa) though inferior respect to cancellous bone (37.6MPa). Of particular interest for a comparison between the obtained biomorphic scaffold and cancellous bone is the behavior once the maximum load is reached. The scaffold made of porous sintered apatite behaves as a typical brittle material, where the compression strength value decay rapidly once reached the maximum load point. Instead the biomorphic scaffold has a behavior similar to cancellous bone. For their particular hierarchically organized structure, they were able to support partially the cracks that were produced when the maximum load was reached, resulting in a gradual decrease in the value of compression strength. Indeed, once cracked, the material do not lose its shape but try to arrange to absorb the crack and redistribute the loads. This is possible thanks to the hierarchically internal structure and to the small dimension of the crystal that composed the scaffold.

5.4.7. Ion release

Dissolution is a physical chemistry process, which is controlled by some factors, such as solubility of the implant matrix, surface area to volume ratio, local acidity, fluid convection and temperature. In general, dissolution rates of calcium phosphates are inversely proportional to the Ca/P ratio, phase purity and crystalline size, as well as it is directly related to the porosity and surface area, CaP degrade in calcium and phosphorus.

The solubility analyses used to investigate the dissolution rate were conducted in TRIS buffer solution at pH 7.3

The cumulative release of Calcium and Phosphate follows a logarithmic trend, with a similar release rate. As can be seen in **Figure.5.18.a-b.**, there was a rapid increase of both calcium and phosphate ions in effluent from the sample in first several hours. This could be caused by the dissolution of the hydrated and partially amorphous layer that cover the crystals obtained in such conditions [23].

In addition, the dissolution curves corresponding to calcium and phosphate reach a relatively stable level for all three scaffolds. In fact, they exhibit a significantly calcium and phosphate dissolution which saturates after less than 72 h, accordingly with the solubility product of stoichiometric hydroxyapatite ($K_{ps} \gg 10^{-56}$) or mixture of β -TCP / HA.

The mean concentrations in steady state were about 1% for calcium ion and about 0.25% for phosphate ions. The solubility behavior of the HA scaffolds is such that it is predictable that ion release can occur over a significant period of time, so in the viewpoint of in vivo application, as these materials, at physiological conditions, are able to continuously supply elements could be essential for osteoblast activity and new bone tissue formation and development.

The results show that the calcium total release is higher than phosphorus, in according to their weight % amount in the hydroxyapatite.

The release of substituting elements, Mg and Sr, occurs with the same kinetics of the other ions, a logarithmic trend. The great difference is in the quantity of ions released as percentage of the initial content, that is possible to see in **Figure 5.18.b.** Magnesium (45.2%) and strontium (18.7%) are released more likely than calcium (4.8%) and phosphorus (4.6%). This is probably due to a partial dissolution reprecipitation process that occur in the solution. The substituted HA is more soluble than stoichiometric HA so, when substituted HA was dissolved, it can reprecipitate as stoichiometric HA.

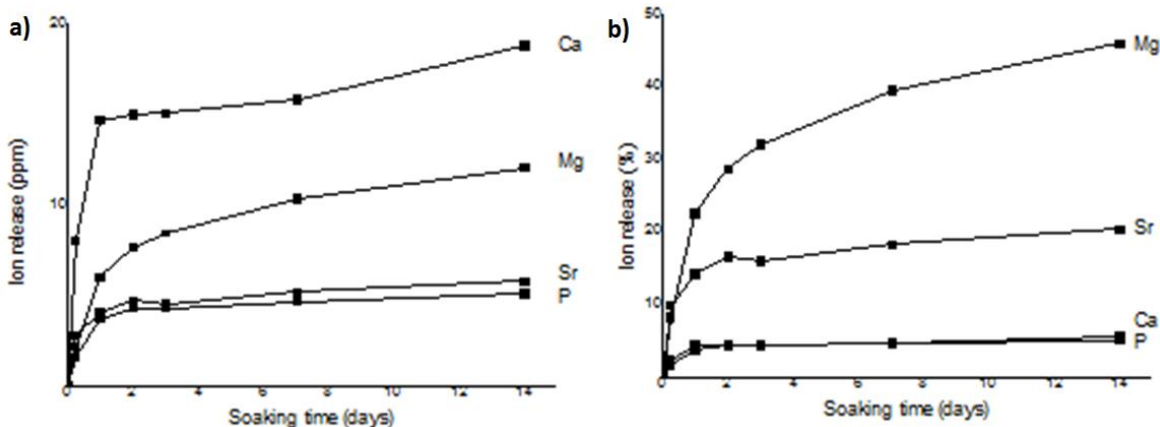


Figure 5.18.a-b. Ion release in function of the soaking time. The results are given in ppm (a) and percentage of the initial ion content (b)

In addition was measured the variation of the pH during the release. If there is a considerable variation in pH during the first phase of the release, it could be toxic for cells when the material is implanted. It was found that pH doesn't vary by more than 0,3 from the initial value during the first phase of the release test (starting average pH = 7.35 ± 0.01 ; final average pH after 72h = 7.35 ± 0.03).

5.5. In vitro characterization

The cell culture was analyzed for cell viability with the Live/Dead assay based on the simultaneous determination of live and dead cells with two probes, Calcein and EthD-1, that measure recognized parameters of cell viability: intracellular esterase activity and plasma membrane integrity respectively. A very high ratio of viable cells were seen with no significant differences among biomorphic MS-BIO-HA and the control S-HA group (**Figure 5.19.a-b**).

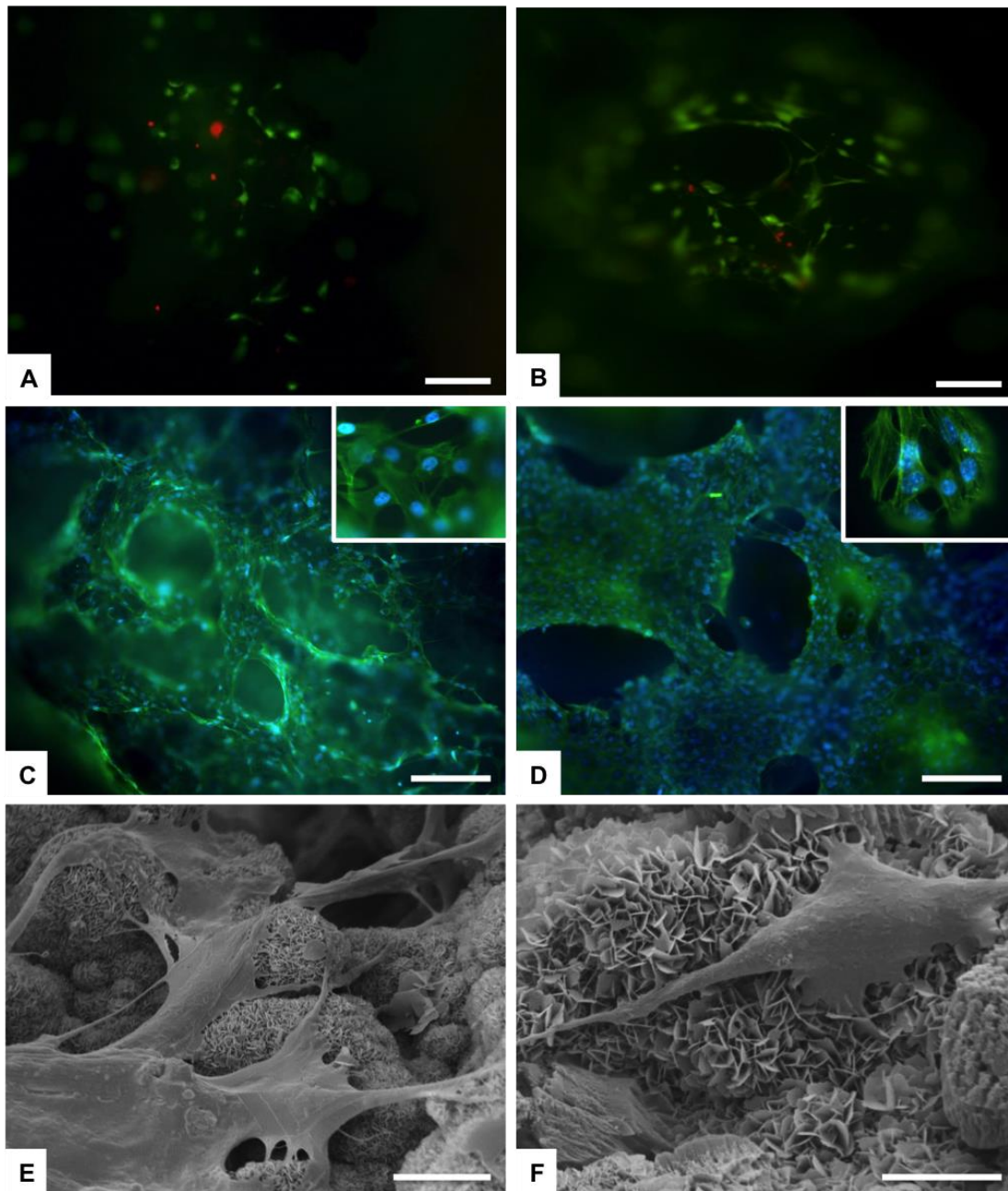


Figure 5.19.a-f. Cell viability analyzed by the Live/Dead assay. Calcein AM stains for live cells in green, EthD-1 stains for dead cells in red. (a) and (b) showed mMSCs seeded on MS-BIO-HA and S-HA samples respectively after 1 day. Analysis of cell morphology by phalloidin staining at day 3. Phalloidin in green stains for actin filaments and DAPI in blue stains for cell nuclei. (c)

MS-BIO-HA (d) S-HA. Analysis of cell morphology assessed by SEM. (e) and (f) show mMSCs seeded on MS-BIO-HA sample at day 1. Scale bars: A-D 200 μm ; E and F 10 μm .

In addition, cell morphology was analyzed by phalloidin staining and scanning electron microscopy. In particular, organization of the cytoskeletal structure of actin filaments is an essential element in maintaining and modulating cellular morphology and cell structural integrity. The morphological analysis showed mMSCs well adhered to the MS-BIO-HA samples without any difference compared to S-HA control group. (**Figure 5.19.c-d.**) After 3 days of cell culture, cells grew into the porous scaffold structure and infiltrated the scaffolds as shown in **Figure 5.19.c-d.** Moreover the nuclear morphological qualitative analysis confirmed that MS-BIO-HA sample was not cytotoxic. In fact, the cell nuclei showed their native morphology and none abnormal alterations were detected (e.g. nuclear fragmentation, chromatin condensation) (**Figure 5.19.c-d.** insets). In addition a detailed cell morphology analysis by SEM, showed, after 24 hours, cells firmly attached to the samples surface, with their typical spindle/fibroblast-like morphology (**Figure 5.19.e-f.**).

The expression of the genes involved in the osteogenic differentiation was analyzed by q-PCR after 14 days of dynamic cell culture condition (**Figure 5.20.**). The results highlighted a significant effect of MS-BIO-HA on the up-regulation of the genes involved in both early (BMP2, Runx2 and ALP) and late (OPN and Col15a1) stages of osteogenic commitment [28], if compared to S-HA sample.

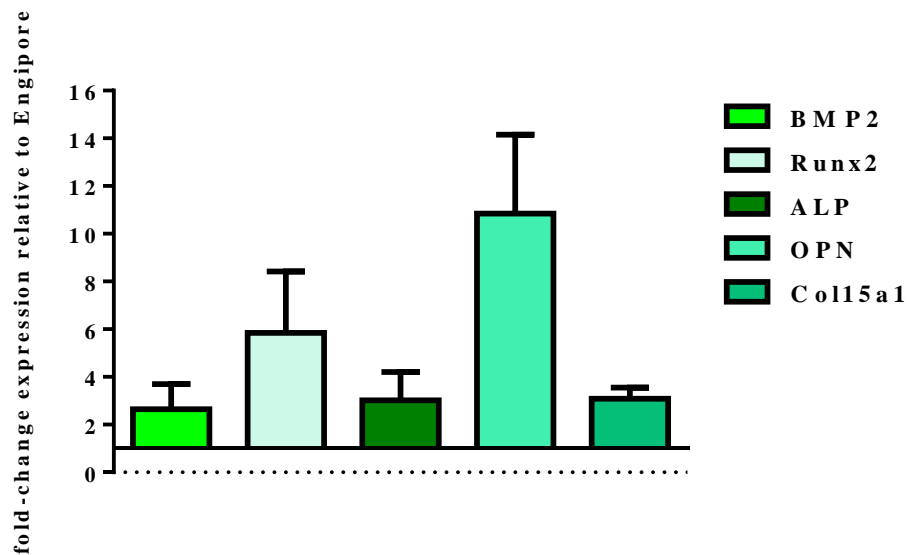


Figure 5.20. Relative quantification ($2^{-\Delta\Delta Ct}$) of gene expression after 14 days of dynamic cell culture. Fold-change expression of the target genes induced by MS-BIO-HA sample, respect to S-HA sample, used as a calibrator, are showed in the graph. Two-way ANOVA analysis indicated statically difference between the samples with $p \leq 0.0001$.

It was already proved the hydroxyapatite inductive effect on MSCs differentiation both as a 3D scaffold-based system [24] and as nanoparticles composition. The obtained results showed that the unique nanostructure and chemical composition of MS-BIO-HA sample amplified the intrinsic inductive power of the biomimetic hydroxyapatite in term of regulation of the principal genes involved in the osteogenic differentiation [29].

The high bioactivity and enhanced resorbability of apatite nanophases with bio-competent ionic substitutions such as carbonate, magnesium and strontium can allow enhanced formation of new bone with organized structure thus strongly accelerating the healing process. In fact, the co-existence of such features could trigger instructive mechanisms for mesenchymal stem cells that, in conditions of dynamic culturing in perfusion bioreactor, dramatically overexpressed a number of genes relevant for the bone regenerative cascade, after 14 days of culturing.

5.6. Conclusions

The results presented indicate that was found a route to the creation of biomorphic scaffold of dimension relevant for in vivo test on big animals (sheep) with optimization and control of the kinetics of every step. The obtained material has been completely characterized from a chemical, physical, mechanical, structural and biological point of view.

The biomorphic transformation of natural ligneous templates with functionally relevant morphology and pore structure, is a fascinating nature-inspired and unique approach, potentially able to surpass all the classical and existing techniques of 3D fabrication of bioceramics for long bone regeneration, including foaming processes, sacrificial templates and also, 3-D rapid prototyping, which lack of a sufficient level of control of the final composition, structure and nanosize features enabling a factual and functionally relevant mimicry with the target tissue.

A relevant finding is that outstanding biologic performance were recorded, following preliminary in vitro evaluation, thus suggesting that the features of biomimesis are uniquely able to trigger, direct and sustain the bone regenerative cascade, possibly without the aid of any other biologic factors or drugs to be added to the scaffold.

Future prospective for this work can concern the production of pieces of the dimension useful for human clinical tests, 6cm of length and 3cm of diameter, the introduction of other ions to give new properties to the apatitic phase, such as Ga or Zn for antibacterial properties, or the loading of drugs, such as anticancer or antibacterial drugs.

5.7. References

- [1] Holmes RE, Bucholz RW, Mooney V. Porous hydroxyapatite as a bone graft substitute in diaphyseal defects: a histometric study. *Journal of orthopaedic research : official publication of the Orthopaedic Research Society* 1987;5:114-21.
- [2] Hoppe A, Guldal NS, Boccaccini AR. A review of the biological response to ionic dissolution products from bioactive glasses and glass-ceramics. *Biomaterials* 2011;32:2757-74.
- [3] Ray RD. Vascularization of bone grafts and implants. *Clinical orthopaedics and related research* 1972;87:43-8.
- [4] Liedert A, Kaspar D, Blakytyn R, Claes L, Ignatius A. Signal transduction pathways involved in mechanotransduction in bone cells. *Biochemical and biophysical research communications* 2006;349:1-5.
- [5] Clohisy JC, Calvert G, Tull F, McDonald D, Maloney WJ. Reasons for revision hip surgery: a retrospective review. *Clinical orthopaedics and related research* 2004:188-92.
- [6] Bose S, Roy M, Bandyopadhyay A. Recent advances in bone tissue engineering scaffolds. *Trends in biotechnology* 2012;30:546-54.
- [7] Muralithran G, Ramesh S. The effects of sintering temperature on the properties of hydroxyapatite. *Ceramics International* 2000;26:221-30.
- [8] Kannan S, Goetz-Neunhoeffler F, Neubauer J, Ferreira JMF. Ionic Substitutions in Biphasic Hydroxyapatite and β -Tricalcium Phosphate Mixtures: Structural Analysis by Rietveld Refinement. *Journal of the American Ceramic Society* 2008;91:1-12.

- [9] Tampieri A, Sprio S, Ruffini A, Celotti G, Lesci IG, Roveri N. From wood to bone: multi-step process to convert wood hierarchical structures into biomimetic hydroxyapatite scaffolds for bone tissue engineering. *Journal of Materials Chemistry* 2009;19:4973-80.
- [10] Sprio S, Ruffini A, Valentini F, D'Alessandro T, Sandri M, Panseri S, et al. Biomimesis and biomorphic transformations: New concepts applied to bone regeneration. *Journal of Biotechnology* 2011;156:347-55.
- [11] Landi E, Sprio S, Sandri M, Celotti G, Tampieri A. Development of Sr and CO₃ co-substituted hydroxyapatites for biomedical applications. *Acta biomaterialia* 2008;4:656-63.
- [12] Woodard JR, Hilldore AJ, Lan SK, Park C, Morgan AW, Eurell JAC, et al. The mechanical properties and osteoconductivity of hydroxyapatite bone scaffolds with multi-scale porosity. *Biomaterials* 2007;28:45-54.
- [13] Zhang L, Zhang B, Yang Z, Guo M. The Role of Water on the Performance of Calcium Oxide-Based Sorbents for Carbon Dioxide Capture: A Review. *Energy Technology* 2015;3:10-9.
- [14] Yoshioka S, Kitano Y. Transformation of aragonite to calcite through heating. *Geochemical Journal* 1985;19:245-9.
- [15] Byrappa K, Yoshimura M. *Handbook of hydrothermal technology*: William Andrew; 2012.
- [16] Kuroda K, Okido M. Hydroxyapatite coating of titanium implants using hydroprocessing and evaluation of their osteoconductivity. *Bioinorganic chemistry and applications* 2012;2012.
- [17] Wang J, Chen W, Li Y, Fan S, Weng J, Zhang X. Biological evaluation of biphasic calcium phosphate ceramic vertebral laminae. *Biomaterials* 1998;19:1387-92.
- [18] Rodríguez-Lorenzo LM, Hart JN, Gross KA. Structural and chemical analysis of well-crystallized hydroxyfluorapatites. *The Journal of Physical Chemistry B* 2003;107:8316-20.

- [19] Yashima M, Sakai A, Kamiyama T, Hoshikawa A. Crystal structure analysis of β -tricalcium phosphate $\text{Ca}_3(\text{PO}_4)_2$ by neutron powder diffraction. *Journal of Solid State Chemistry* 2003;175:272-7.
- [20] Landi E, Celotti G, Logroscino G, Tampieri A. Carbonated hydroxyapatite as bone substitute. *Journal of the European Ceramic Society* 2003;23:2931-7.
- [21] Liu J, Ye X, Wang H, Zhu M, Wang B, Yan H. The influence of pH and temperature on the morphology of hydroxyapatite synthesized by hydrothermal method. *Ceramics International* 2003;29:629-33.
- [22] Monmaturapoj N, Yatongchai C. Effect of sintering on microstructure and properties of hydroxyapatite produced by different synthesizing methods. *Journal of Metals, Materials and Minerals* 2010;20:53-61.
- [23] Zahn D, Hochrein O. Computational study of interfaces between hydroxyapatite and water. *Physical Chemistry Chemical Physics* 2003;5:4004-7.
- [24] Papadimitropoulos A, Piccinini E, Brachet S, Braccini A, Wendt D, Barbero A, et al. Expansion of human mesenchymal stromal cells from fresh bone marrow in a 3D scaffold-based system under direct perfusion. *PloS one* 2014;9:e102359.
- [25] Papadopoulos NG, Dedoussis GV, Spanakos G, Gritzapis AD, Baxevanis CN, Papamichail M. An improved fluorescence assay for the determination of lymphocyte-mediated cytotoxicity using flow cytometry. *Journal of immunological methods* 1994;177:101-11.
- [26] Faulstich H, Zobeley S, Rinnerthaler G, Small JV. Fluorescent phallotoxins as probes for filamentous actin. *Journal of muscle research and cell motility* 1988;9:370-83.
- [27] Livak KJ, Schmittgen TD. Analysis of relative gene expression data using real-time quantitative PCR and the $2^{-\Delta\Delta C(T)}$ Method. *Methods* 2001;25:402-8.

[28] Orlando B, Giacomelli L, Ricci M, Barone A, Covani U. Leader genes in osteogenesis: a theoretical study. *Archives of oral biology* 2013;58:42-9.

[29] Montesi M, Panseri S, Iafisco M, Adamiano A, Tampieri A. Effect of hydroxyapatite nanocrystals functionalized with lactoferrin in osteogenic differentiation of mesenchymal stem cells. *Journal of biomedical materials research Part A* 2015;103:224-34.

6. Final conclusions and future perspectives

In the present work, three different novel approach at biomimetic substituted hydroxyapatitic nanophases addressed to regenerative bone surgery have been developed and optimized.

In summary:

- 1) New hydroxyapatitic multisubstituted nanosized phases were prepared by neutralization reaction. Different extent of ionic substitution of Zn^{2+} or Ga^{3+} , Mg^{2+} and CO_3^{2-} were inserted during the synthesis of the new phases to increase biomimicry and give antibacterial activity. These ionic substitution have a double effect on the apatitic phase. A first effect is the enhanced osteoinductive properties of HA on human mesenchymal stem cells. Another effect is the antibacterial properties of this new materials, tested against 4 different strains of pathogenic bacteria and yeast. The antibacterial efficiency is maintained also after 15 days of conditioning. Of particular interest are the multisubstituted phase that shows synergistic effect of the three different ions both on the osteoinductive and antibacterial side. These materials can be addressed to the use as coating for prosthetic implants or as material to create bone scaffolds itself giving an integrated solution to problems linked with bacterial infection and lack of osteointegration.
- 2) The use of strontium doped hydroxyapatite has already been demonstrated effective as anti-osteoporotic agent. An useful and simple technique (PED) able to deposit a thin, well adherent coating of Sr-doped calcium phosphate on the surface of a thermoplastic material like PEEK was developed. A well crystalized nanophase coating of hydroxyapatite with a Sr/Ca ratio close to the initial phase was obtained after a mild heating treatment. This coating improve roughness and

wettability of PEEK and can consequently increase its in vivo bioactivity and its biological fixation without compromising its mechanical properties.

- 3) A 6-steps process with total control of the kinetic of reaction of each step was optimized to produce biomimetic scaffolds. The obtained scaffolds maintain the initial hierarchical structure and the pore range distribution of the rattan canes used as templates but are composed calcium phosphates. The scaffolds were obtained in two different composition, a Mg-Sr-CO₃- multi- substituted nanosized biphasic calcium phosphate (hydroxyapatite : β -TCP 70:30) and a monophasic nanosized carbonate-hydroxyapatite. These two scaffolds were able to support mechanical load and trigger directly the cells regenerative cascade. To improve further properties of the scaffolds it is possible insert other ions in the apatitic lattice or load biologicals, such as grow factors or anticancer, antibacterial or antiosteoporotic drugs. After sheep tests scaffolds would be produced in pieces of dimensions useful for clinical tests that can represent the first option for the regeneration of load bearing portion of long bones.

7. Acknowledgments

This thesis would not have been possible without and Anna Tampieri, Simone Sprio and Andrea Ruffini who introduced me to the bioceramics research field and supervised all my work.

I want to thank all my colleagues of the Bioceramics and Bio-hybrid Composites Group from the Institute of Science and Technology for Ceramics (Italy), for their support and collaboration, in particular Silvia Panseri, Monica Montesi, for the valuable contribution and discussion about the biological interaction of biomaterials and for the biological in vitro tests. I would also thank Daniele Dalle Fabbriche, Claudio Capiani, Cesare Melandri, Guia Guarini, Andreana Piancastelli and Paola Pinasco for the significant support in the laboratory during the characterization of my materials.

I wish to thank Prof. Giuseppe Falini, my academic supervisor, and the staff of his lab, for the smart suggestions and valuable support during my PhD.

My thanks also go to a lot of scientists from companies and other academic institutions who collaborated to the studies presented in this thesis. In particular I would like to thank Lorenzo Pradella and Angela Palumbo, from Greenbone Ortho s.r.l. (Faenza, Italy), as well as Michele Bianchi (Istituto Ortopedico Rizzoli, IOR, Laboratorio NaBi) for the work on coating deposition.

I also would like to thanks Fondazione del Monte di Bologna e Ravenna for providing the financial support for the work on Sr-HA coatings.